Where dust comes from: Global assessment of dust source attributions with AeroCom models

Dongchul Kim[1,2], Mian Chin[2], Greg Schuster[3], Hongbin Yu[2], Toshihiko Takemura[4], Paolo Tuccella[5], Paul Ginoux[6], Xiaohong Liu[7], Yang Shi[7,8], Hitoshi Matsui[9], Kostas Tsigaridis[11,10], Susanne E. Bauer[10,11], Jasper F. Kok[12], and Michael Schulz[13]

[1]University of Maryland, Baltimore County, Baltimore, MD, United States
[2]NASA Goddard Space Flight Center, Greenbelt, MD, United States
[3]NASA Langley Research Center, Hampton, VA, United States
[4]Research Institute for Applied Mechanics, Kyushu University, Fukuoka, Japan
[5]University of L'Aquila, L'Aquila, Italy
[6]NOAA/OAR, Geophysical Fluid Dynamics Laboratory, Princeton, New Jersey, United States
[7]Texas A&M University, College Station, TX, United States
[8]Now at Massachusetts Institute of Technology, Cambridge, MA, United States
[9] Graduate School of Environmental Studies, Nagoya University, Nagoya, Japan
[10]NASA Goddard Institute for Space Studies, New York, NY, United States
[11]Center for Climate Systems Research, Columbia University, New York, NY, United States
[12]University of California, Los Angeles, Los Angeles, United States
[13]Norwegian Meteorological Institute, Oslo, Norway

ABSTRACT

The source of dust in the global atmosphere is an important factor to better understand the role of dust aerosols in the climate system. However, it is a difficult task to attribute the airborne dust over the remote land and ocean regions to their origins since dust from various sources are mixed during long-range transport. Recently, a multi-model experiment, namely the AeroCom-III Dust Source Attribution (DUSA), has been conducted to estimate the relative contribution of dust in various locations from different sources with tagged simulations from 7 participating global models. The BASE run and a series of runs with 9 tagged regions were made to estimate the contribution of dust emitted in East- and West-Africa, Middle East, Central- and East-Asia, North America, the Southern Hemisphere, and the prominent dust hot spots of the Bodélé and

Taklimakan Deserts. The models generally agree in large scale mean dust distributions, however models show large diversity in dust source attribution. The inter-model differences are significant with the global model dust diversity in 30 - 50 %, but the differences in regional and seasonal scales are even larger. The multi-model analysis estimates that North Africa contributes 60 % of global atmospheric dust loading, followed by Middle East and Central Asia sources (24 %). Southern hemispheric sources account for 10 % of global dust loading, however it contributes more than 70 % of dust over the Southern Hemisphere. The study provides quantitative estimates of the impact of dust emitted from different source regions on the globe and various receptor regions including remote land, ocean, and the polar regions synthesized from the 7 models.

Corresponding author: Dongchul Kim (dongchul.kim@nasa.gov)

Key points:

- Contributions of various dust sources are quantitatively estimated in a multi-model experiment.
- Contributions of various sources have different horizontal and vertical distributions and seasonality.
- Dust near source regions are dominated by dust emitted in the upwind source regions; however many remote land, ocean, and polar regions are affected by a mixture of dust from various sources around the globe.

1. Introduction

Mineral dust aerosols are small airborne particles, primarily emitted from soils by aeolian processes including saltation and aerodynamic entrainment (Gillette et al. 1998; Marticorena and Bergametti, 1995; Marticorena et al., 1997; Macpherson et al., 2008; Shao et al., 2011). As the most abundant aerosol type by mass in the Earth's atmosphere, mineral dust plays an important role in global climate by interacting with incoming and outgoing radiation, providing liquid and ice cloud nuclei, and affecting atmospheric stability (Haywood et al., 2005; Forster et al., 2007; Evan et al., 2008, DeMott et al., 2010; Creamean et al., 2013; Colarco et al., 2014; Rosenfeld et al., 2014; Shi and Liu, 2019; Jordan et al., 2020; Shi et al., 2022; Kawai et al., 2023). Dust has important implications on global biogeochemical cycles through fertilizing terrestrial and ocean ecosystems and modulating carbon uptake (Albani et al., 2014; Jickells et al., 2005; Maher et al., 2010; Yu et al., 2015; Checa-Garcia et al. 2021; Westberry et al., 2023). Also, dust is a major $PM_{2.5}$ aerosol contributor over or near dust source regions across the global (Hand et al., 2017, Bauer et al., 2019).

Dust source regions on a global scale have been extensively studied from many previous investigations (e.g., Tegen and Fung, 1995; Ginoux et al., 2001, 2012; Zender et al., 2003; Shao et al., 2011; Kok et al., 2021a-b, 2023). The majority of dust mass is emitted from the so-called dust-belt which includes North Africa, the Middle East, and East Asia. Other regions like North America, South America, South Africa, and Australia are also known as important dust source regions contributing dust to the Earth's atmosphere. Once emitted, dust can travel thousands of kilometers across the entire hemisphere, and some of them reach pristine remote areas and the polar regions. These long-range transported dusts have profound impacts on the regional hydrological cycle and climate system when they are deposited on snow and ice surfaces, by decreasing surface albedo and increasing snow and ice melting (Bullard et al. 2016). Dust from different sources is known to have different mineral compositions, and thus different optical properties, with important implication for climate studies (Formenti et al., 2014; Engelbrecht et al., 2016; Di Biagio et al., 2017).

Because of the importance of the long-range transported dust in the Earth's atmospheric system, several studies have investigated the source-receptor relationships between major dust sources and various receptors over land, ocean, and the polar regions by using global model simulations, inverse modeling approaches, and composite methods (Mahowald et al., 2005 and references therein; Shao et al., 2011; Hamilton et al., 2019; Kok et al., 2021a, 2021b, 2023). These studies commonly indicate the significant contribution from various sources to the global dust distribution including remote oceans, such as the Northern Pacific and the Northern Atlantic Oceans. However, they also show a wide range of differences between studies, which can reach up to a factor of more than ten, mainly associated with the complex surface and atmospheric processes, including emission parameterization, dry deposition, wet deposition, and atmospheric dynamics (Huneeus et al., 2011; Kim et al., 2014, 2019). Although dust emission is one of the most important drivers for the global and regional dust cycle, the relative contribution of various dust sources to remote areas via long range transport is not well studied.

It is challenging to attribute dust sources over the remote land and ocean regions, since dust is mixed during long-range transport, where it experiences complex atmospheric processes, including horizontal and vertical-advection, wet deposition, and dry deposition. The spatial and temporal variation of dust emission is also an important factor in estimating dust source attribution. A recent study has estimated the relative contribution of various sources over the remote ocean and polar regions using an inverse modeling technique, showing that dust over most regions are a mixture from many different sources (Kok et al., 2021a,b). However, it is still necessary to conduct more concerted studies to assess the robustness of estimated dust source attributions on global and regional scales.

We report here the results from a recent multi-model experiment named Dust Source Attribution (DUSA), under the umbrella of the internationally coordinated AeroCom Phase III project. Using the multi-model simulations that tag dust emission and transport from 9 dust source regions in the world, the DUSA study aims to (1) examine the model diversity in dust source attribution and (2) estimate the contribution of dust sources to various receptor regions, including remote land/ocean and the polar regions in different altitudes, from the multi-model statistics.

The rest of the paper is organized as follows. In section 2, we describe the domains of dust sources and receptors used in this study, the participating global models, and the experiment setup. The source contributions are compared between models in section 3, the source contributions from the multi-model mean are analyzed in section 4, and the impact of sources on various receptor regions are presented in section 5. Finally, discussions and summary are given in section 6 and 7, respectively.

2. Method

AeroCom is an internationally coordinated effort to advance the understanding of atmospheric aerosols and to document and diagnose differences between models and observations (http://aerocom.met.no). The DUSA experiment, as a part of the AeroCom phase III experiments, has been conducted with a goal to better understand the relative role of various sources in the global dust distribution, including for dust in remote land, ocean, and polar regions as well as in the planetary boundary layer and the free troposphere. Seven models have participated in the

AeroCom-III/DUSA experiment, and they have provided daily and monthly model output from 2009 to 2012. Each model provided a BASE run, which is a standard model simulation, and multiple experimental runs with tagged source regions.

The major sources of mineral dust are well recognized as most of the air-borne dust originate from a few major arid and semiarid regions in North Africa, the Middle East, and Asia, which account for more than 80% of global dust emission, with other smaller dust sources accounting for the remaining portion (Ginoux et al., 2012). The DUSA experiment considers 9 dust source regions that comprise nearly all dust sources except for the Arctic sources, as shown in Figure 1. The source regions include West Africa (WAF), East Africa (EAF), Bodélé Depression (BOD), Middle East (MDE), Central Asia (CAS), East Asia (EAS), Taklimakan desert (TAK), North America (NAM), and the Southern Hemisphere (SOH), which in turn contains dust sources in South America, southern Africa, and Australia. Each model provides a total of 10 simulations, including one BASE simulation with all sources (see Figure S1) and 9 tagged dust source simulations, each with dust emission from a particular source region excluded. The difference between the dust from the BASE run and the tagged run (i.e., BASE minus Tag) are considered as dust from the tagged region. It is worth noting that the sum of dust from all tagged regions is not always the same as total dust from the BASE simulation, which can be explained by a) there are some dust emissions outside of the prescribed tagged regions, and b) model simulations with interactions between aerosol and radiation or cloud can cause changes of the meteorological conditions (such as winds, circulations, precipitation). They induce the differences in dust quantities between BASE and the sum of the 9 tagged runs (denoted as SUM). The global difference of dust emissions between BASE and SUM is between 0 and 2.5 % for the 7 models. To conserve the mass, we use SUM as total dust in most of the DUSA analysis, otherwise specified as BASE.

We define 14 receptor regions across the globe for budget analysis of the source-receptor relationships. They consist of 7 land regions, 5 ocean regions, and 2 polar regions (Figure 2). The land receptor regions include 5 populated regions (i.e., North America (NAM), Europe (EUR), India (IND), East Asia (EAS), and Tropical North Africa (TNAF)) and 2 relatively remote regions (i.e., Amazon (TMZ) and Tibetan Plateau (TBP)). Tibetan Plateau is defined as the area where the elevation is higher than 4 km in the region (70°E~120°E; 29°N~40°N). The ocean regions are grouped to the North Atlantic (NATL), South Atlantic (SATL), North Pacific (NPAC), South Pacific (SPAC), and Indian Ocean (INDO). The Arctic (ARC) and Antarctic (AARC) regions are defined as the area with latitudes higher than 66.3°N and 66.3°S, respectively. The 7 land receptor regions are chosen by the importance in the geochemical cycles and source-receptor relationship. And the other 7 regions are chosen to cover all the oceanic regions and two polar regions.

The 7 participating models are GFDL-AM4, CAM5-ATRAS, CESM2.1.3 (hereafter CESM2), GEOS-GOCART (hereafter GEOS), GEOS-Chem, GISS-ModelE2.1.1-OMA (hereafter GISS-OMA), and MIROC-SPRINTARS (hereafter SPRINTARS). The model setup and configurations are model-dependent, for example, their horizontal resolutions range from 0.5° (longitude) × 0.5° (latitude) in GEOS to 2.5°×2° in GEOS-Chem and GISS-OMA (Table 1). Vertical coordinates range from 30 layers in CAM5-ATRAS to 72 in GEOS. The meteorology fields that drive dust emissions, transport, and deposition in most models are simulated with various levels of observational nudging and reinitialization.

There are also similarities and differences in dust physical properties among models. Although dust density values are similar across the models at 2.5 or 2.65 g cm^{-3}, the range of dust size and the number of size groups are different (Table 1). GFDL-AM4, GEOS, and SPRINTARS have the same size range (0.1-10 μm in radius), but size bins in SPRINTARS are different from GFDL-AM4 and GEOS. CAM5-ATRAS and GEOS-Chem have similar maximum dust size (5 and 6 μm in radius, respectively) but CAM5-ATRAS considers several additional ultra-fine aerosol bins with radius at 0.0005-0.078 μm. Overall, the maximum dust particle size of 16 μm in radius from GISS-OMA is the largest among all models. While most models report dust particle size range in each bin and the size distribution for dust emission and mass concentration are same, CESM2 specifies 3 size modes for dust emissions in the ranges of 0.01-0.1-1.0-10.0 μm of modal diameter. Dust is assumed to be internally mixed with other aerosol species in each mode and the mode diameters are freely evolving with time and locations. All models calculate dust emissions driven mostly by either 10-m wind or friction velocity and dust loss processes of dry deposition (including gravitational sedimentation and surface layer aerodynamic dry deposition) and wet deposition (including in-cloud rainout and below-cloud washout). The dust optical depth (DOD) is calculated from dust column mass by using the mass extinction efficiency (MEE), which is computed from the refractive indices of dust and particle size distributions. However, these physical and optical properties and atmospheric processes are mostly calculated with various degrees of parameterizations that can vary significantly among models.

In most of the analysis presented in this study, we use the percentage of dust mass fraction from a particular source region, F_{src}, to quantify the relative contributions of region-specific dust in horizontal and vertical spaces. By definition, F_{src} is simply the percentage of dust from a tagged source region to total dust in SUM. Following previous AeroCom multi-model studies (e.g., Textor et al., 2006; Schultz et al., 2006; Kim et al., 2019), we use the term "diversity" to express the differences among model simulated quantities, which is defined as the ratio of standard deviation of the model results to the multi-model mean in percentage.

3. Comparisons of dust source contribution between the models

3.1 Global dust budget and evaluation

We first examine the global dust budget related variables from the BASE simulations of the participating models (Table 2). The multi-model mean and standard deviation of global total emission (EMI) are 2196 ± 1091 Tg yr^{-1}, where the difference among the models is almost a factor of four with the largest emission in CAM5-ATRAS (4311 Tg yr^{-1}) and the lowest emission in GEOS-Chem (1130 Tg yr^{-1}), which is consistent with previous estimations (Huneeus et al., 2011; Kok et al., 2021b). Globally, the annual mean of total deposition (DEP) amount is approximately the same as the total emission (within a few percent of difference). The multi-model mean of dust column loading (LOAD) and DOD are 21.4 ± 9.4 (Tg yr^{-1}) and 0.023 ± 0.007, respectively. Model diversity of EMI and DEP is around 50 % while the diversities of LOAD and DOD are slightly lower with the values of 44 % and 31 %, respectively. Three models (i.e., GFDL-AM4, GEOS, and SPRINTARS) have the same particle size range but they still differ by 61 % in emission and 80 % in column loading. The differences among models are a factor of three or four in global dust emission, loading, and DOD. From previous studies, it has been revealed that most parameters associated with dust cycles exhibit large diversities among models, including size distributions, emission parameterizations, surface conditions, dry- and wet removal schemes, advection/convection transport schemes, and MEE (Kim et al., 2014, 2019).

Although most dust quantities listed in Table 2 are difficult to observe such that there is no credible data to evaluate or constrain them, the coarse-mode AOD (AODc) from the ground-based AErosol RObotic NETwork (AERONET) retrievals (SDA algorithm of Version 3, Level 2) (Holben et al., 1998; O'Neill et al. 2003) can be considered as the closest proxy of DOD from observations, even though not all the coarse-mode aerosols such as sea-salt are dust and some dust is in the fine-mode. Here, we compared the monthly averaged model simulated DOD with the monthly averaged AODc from AERONET in Figure 3, following previous studies (e.g., Kim et al., 2021). The model grid points nearest to AERONET locations are chosen in the comparison.

A total of 55 AERONET sites were chosen, based on a previous dust study by Capelle et al. (2018), with AODc data available for the study period of 2009-2012. While the mean DOD in these 55 AERONET sites is 0.142, modeled mean DODs at the same locations have a wide range from 0.063 (SPRINTARS) to 0.219 (CAM5-ATRAS) (Figure 3a). Correlation coefficient between model simulated DOD and the AERONET are in the range of 0.476 for GISS-OMA to 0.862 for GEOS. Normalized standard deviations to observation in models are between 0.64 for SPRINTARS and 1.87 for CAM5-ATRAS. Overall, the Taylor diagram of the comparison shows that models have a certain level of skills in simulating global dust in terms of DOD, however, they exert significant discrepancies (Figure 3b). The multi-model mean DOD is 0.131 for the 55 sites, which is 22 % lower than the mean AODc from AERONET, and its correlation coefficient with AERONET AODc is 0.67. The horizontal distribution of the multi-model mean DOD captures that of the AERONET AODc (Figure 3c). The spatial distribution of models and remote sensing (i.e., MODIS) capture the dominant contribution of the dust belt, however the detailed structure and magnitude vary by models (Figure S2). The multi-model mean also shows a reasonable performance when its deposition is compared with observations with a correlation coefficient of 0.71 (Albani et al., 2014, Figure S3).

3.2 Dust source contribution from the AeroCom models

In this section, we show the fractions of dust emitted from each tagged region to total global dust emission (SUM) from the models (Figure 4 and Table 3). From the multi-model mean, contributions of North African sources to total dust emissions are 24.3 %, 19.0 %, and 8.7 %, for WAF, EAS, and BOD, respectively; together, North Africa (WAF+EAF+BOD) accounts for 52 % of total dust emission, representing the most significant dust source region. Although BOD is considered as a prominent dust source in North Africa, the model estimates that only 8.7±5.3 % dust is emitted from BOD. The 2nd largest dust source region group is western Asia (MDE and CAS) that account for 25 % of total dust emissions with MDE and CAS contribute 14.5 % and 10.5 %, respectively. For the rest of the dust regions in the northern hemisphere, eastern Asia contributes to 9.1 % (5.3 % from EAS and 3.8 % from TAK), and NAM contributes to only 1.2%. Together, the dust source regions in the northern hemisphere emit 87.3% of dust whereas the southern hemisphere SOH contributes to 12.7 %.

The regional emissions and their relative contributions from each individual model are also detailed in Figure 4 and Table 3. Most models agree that WAF (24 ~ 36 %) emits more dust than EAF (15 ~ 23 %), except for CESM2 (8 % for WAF and 26 % for EAF). Most models also agree that North Africa (WAF+EAF+BOD) is the most significant dust source accounting for about one half of total dust emission (46 % ~ 62 %), except for CESM2 (34 %). The region among the largest differences in model estimated emissions is SOH with the maximum-to-minimum emission ratio of a factor of 19 and diversity of 113%. Although the diversity is even larger for NAM, the emission amount is very small compared to other regions. The differences over regions in Asia (MDE, CAS, TAK, and EAS) are also large with the max-to-min ratio of dust emissions ranging from a factor of 6 (MDE) to 13 (TAK) and diversity from 59 % (CAS) to 87 % (MDE). The models agree the best over the Northern Africa regions, although the max-to-min ratio is still a factor of 3-5.

The source contributions to the global dust are also calculated for LOAD and DOD. As shown in Figure 4, the regional percentage contributions to EMI, LOAD, and DOD are quite similar for each model, suggesting that the contributions of dust column load and DOD from different source regions are closely proportional to the regional emissions on global and annual average bases. As displayed in Figure 4, CESM2 shows a remarkably larger fraction of dust from SOH (around 30 % for emission, load, and DOD) than from all other models (from 3 % to 14 %). Conversely, it attributes a much smaller fraction of dust from WAF (≤10 % for emission, load, and DOD) than the rest of the models (from 25 % to 40 %) due to the source function (Zender et al., 2003) used for dust emission (Wu et al., 2020). A recent study has implemented several new parameterizations of aeolian processes (e.g., soil size distribution, drag partitioning, intermittent dust emissions by turbulent wind) to further improve the spatial distribution in CESM2 (Leung et al., 2024).

3.3 Spatial features of regional dust contributions simulated by models: WAF as an example

We choose a case of WAF to demonstrate how models are compared for the dust mass load (Figure 5) and vertical zonal mean of dust mass concentrations (Figure 6) from that region as well as the F_{src} of WAF average for 2009-2012 (Similar plots for all tagged regions are included in Figure S4-S21). While most of the WAF generated dust is transported to the west by the trade winds across the Atlantic Ocean (Figure 5), a branch of eastward transport appears following the prevailing-westerlies. As a result, F_{src} is highest over the source region of West Africa (>80 %) and the North Atlantic Ocean (40 ~ >80 %), and moderate F_{src} values (20 ~ 40 %) appear over the mid- and high latitude of the Northern Hemisphere. The magnitude of F_{src} of WAF is different between models with the highest global value in SPRINTARS (20.3 %) and the lowest in CESM2 (8.8 %), while multi-model mean is about 28 %. The models also show different transport features, for example, CAM5-ATRAS has the highest dust load but dust is more concentrated near the source, whereas the load in GISS-OMA is lower than CAM5-ATRAS but dust is more widely spread to downwind regions.

The zonal mean vertical distributions of dust concentrations and F_{src} of WAF between models are compared in Figure 6. All models show highest value over the latitudes of West Africa (10°N ~ 30°N) in the range of 30 ~70 %. Vertical extent depends on models; some models (GFDL-AM4 and GISS-OMA) show F_{src} of >30 % reaching 200 hPa, while other models display lower extent below 300 hPa. Dust concentration in the middle to upper troposphere is lowest in GEOS-Chem with 0.1 µg m^{-3} contour line confined below 400 hPa, but highest in GISS-OMA with the same contour line extending to 200 hPa. Latitudinal patterns of WAF dust F_{src} are generally similar among models, which show a poleward extension of WAF F_{src} to the Arctic in the free troposphere except SPRINTARS. Dust mass from WAF is however mostly confined in the equator and northern hemisphere (latitudes > 10°S, black contour lines in Figure 6) with little trans-hemispheric transport.

In summary, all models show high F_{src} from WAF over source regions and it gradually decreases downwind in horizontal and vertical directions. Although there are differences in patterns and magnitudes, the general characteristics of F_{src} among models are comparable. Similar characteristics for the model agreement are generally shown for other source regions as well (see Figures S2-S19 in supplementary material). Therefore, in next section (Section 4), we use the multi-model mean, instead of using individual models, to present the dust source attributions from different source regions.

4. Dust source attributions from multi-model mean

In this section, contributions of dust from different source regions (Figure 1) to the receptor regions (Figure 2) are estimated using the multi-model mean of DUSA experiment averaged for 2009-2012. The resolutions of 7 participating models are regridded to a common 1°×1° horizontal resolution and 51 vertical layers at 20 hPa interval between 1000 and 1 hPa for the multi-model mean calculations.

4.1 Horizontal distribution of air-borne dust from different source regions

In this section, we compute the source contribution using LOAD and F_{src} calculated from the multi-model mean. In general, all sources show the largest LOAD and F_{src} over the source region then gradually decrease during transport (Figure 7). Their transport patterns are shown on the map. Dust mass from North African sources (WAF, EAF, BOD) are transported both to the west over the Atlantic Ocean and to the east toward Asia and the Northern Pacific Ocean, although the westward transport is stronger than the eastward transport in latitudes south of 30°N. Global mean LOAD values are 11.8, 9.0, and 4.2 mg m^{-2} for WAF, EAF, and BOD, respectively, and the sum of three regions are 25.0 mg m^{-2}, accounting for 59.4 % of the total load (42.1 mg m^{-2}). The distribution of F_{src} is quite different from that of LOAD due to mixing with dust from other regions. Relative to other tagged regions, WAF is the most important dust source region with the largest F_{src} over extended land and ocean areas in the Northern Hemisphere. It dominates the dust over the western North Africa, Central America, and the entire Northern Atlantic Ocean with values of 50 to >90 %. The F_{src} of WAF is also the highest over the eastern tropical Pacific Ocean (30 ~ 50 %) and even over the Arctic (>20 %). Collectively, the North African sources (WAF, EAF and BOD) account for almost 60% of the global dust loading (28 % for WAF, 21 % for EAF, and 10 % for BOD), although their dominance is mostly in the Northern Hemisphere.

Dust emitted in MDE and CAS also exert large influences beyond the source locations. Model simulations show that dust emitted from MDE is the largest contributor to the dust load over the northern Indian Ocean, whereas dust originating from CAS has significant impact over Eurasia. The F_{src} of CAS dust over the Arctic is the 2nd largest one (10 ~ 20 %) after WAF, and the F_{src} of MDE and CAS over the North Pacific are in the order of >10%, larger than that from the East Asian sources in the tropical and subtropical area. The global mean dust LOAD for MDE and CAS are 6.35 and 3.70 mg m^{-2}, respectively. Together, MDE and CAS contributes to nearly 24 % of global total dust load (15 % for MDE and 8.8 % for CAS).

Compared with the regions discussed so far, dust emitted in East Asia from EAS and TAK have smaller global influences. They transported almost exclusively to the east across the North Pacific to the northern part of North America, and some of them are transported to the Arctic. The global mean LOAD values are 1.26 and 1.15 mg m^{-2} for EAS and TAK, respectively, representing 6 % of global dust load from these two regions (3.0 % for EAS and 2.7 % for TAK). Dust emission from NAM is the lowest among all tagged regions and its influence is mainly over the U.S. and neighboring coastal areas. The global mean LOAD of NAM dust is 0.29 mg m^{-2}, or only 0.7 %.

Lastly, Figure 7 shows that 80% of the air-borne dust over the Southern Hemisphere is from SOH, which combines source regions of Patagonia in South America, along the Namibian coast and in Southern Africa, and the Lake Eyre basin and surrounding areas in Australia. Although it is a predominant source in the Southern hemisphere, SOH only contributes to 10 % of the global dust load (mean LOAD 4.38 mg m^{-2}), which is in a similar magnitude as BOD. The multi-model dust estimations and the contribution of various dust sources to the global dust is summarized in Tables 4 and 5.

4.2. Vertical distribution of air-borne dust from different source regions

The zonal mean vertical profiles of the model-mean dust mass and F_{src} for each dust sources are plotted in Figure 8. All sources commonly show the maximum dust mass and F_{src} values from each source region are near the latitudes of the source, then they are being transported vertically and horizontally by convection and the large-scale circulation. The vertical distributions of dust mass concentration from WAF, EAF, BOD, and MDE show similar features, i.e., the 0.1 μg m^{-3} contour line reaches 300-250 hPa, and latitudinally it extends to the south of the equator to ~10°S. Vertically, F_{src} of WAF dust is quite uniform at 30-50 % from surface to 200 hPa in the Northern Hemisphere, but the cores of F_{src} of EAF, BOD, and MDE are located at different latitudes.

Because of the locations of Asian dust sources of CAS and EAS are a little further north than the dust source regions in North Africa and MDE, emitted dust are easier to be advected northward to the Arctic, such that the F_{src} of CAS and EAS are higher in the north (35-90°N) than other latitudes. On the other hand, because the elevation of TAK source is relatively higher at 1.2-1.5 km above sea level, dust emitted from TAK is more readily to reach higher altitudes than from CAS and EAS, as shown in Figure 8 that its maximum contributions is in the upper troposphere at 400-300 hPa. For the rest of the tagged regions, dust from NAM contributes no more than 10 % of zonal mean dust fraction, and, as expected, SOH dust dominates the entire southern hemisphere throughout the atmospheric column.

Evidently, dust emitted from different source regions are much better mixed at higher altitudes even though the concentrations are orders of magnitudes lower than that in the PBL. Similar source-transport relationship is shown in longitude-pressure plots (Figure S22). In the next section, we will show distributions of dust from different source regions in the 3-dimensional space, i.e., horizontal distributions at several layers in different altitudes, to better comprehend the source attributions.

4.3. Source contributions in different vertical layers

In this section, we examine dust distribution and source contributions in different vertical altitudes with the multi-model mean. We have specifically defined 4 layers roughly representing the mixed layer (0 ~ 2.5 km; Layer 1), lower free troposphere (2.5 ~ 6 km; Layer 2), upper free troposphere (6 ~ 12 km; Layer 3), and stratosphere and above (12 km ~ top of atmosphere; Layer 4) to characterize the dust amount and source contributions in these layers (Figure 9). The multi-model mean shows that on an annual averaged basis, 95% of the 21 Tg dust column mass is located below 6 km, with 72% (15.5 Tg) in Layer 1 and 23% (5.0 Tg) in Layer 2. For the rest, 4 % (0.8 Tg) and 1 % (0.2 Tg) are contained in Layer 3 and Layer 4, respectively (left and middle columns in Figure 9). The dust mass distributions in the tropospheric layers are similar throughout the layers (i.e., Layers 1~4) showing the dust source locations and transport to downwind regions. Although there is only 1 % of the dust in Layer 4, the dust belt still contains more dust than the rest of the world in the upper troposphere.

The fraction of $LOAD_k$ (dust mass integrated in layer k) to the total column LOAD (Figure 9, middle column) shows that 72 % of LOAD is over the source regions in Layer 1, with the highest fractions over the source areas. However, the spatial pattern for Layer 2 is the opposite to Layer 1, showing that the fraction over remote regions is larger than over source regions. It means that transported dust becomes more important for the remote region than near surface in Layer 2, e.g., $LOAD_k$ in Layer 2 (40 ~ 50 %) over the North Pacific Ocean is larger than $LOAD_k$ in Layer 1 (30 ~ 40 %). The contrast of dust fractions between remote and source regions are even larger in Layers 3 and 4, and the dust fractions over the polar regions are 20 ~ 30 % in Layer 3, compared to less than 5 % over the source regions. The results in Figure 9 and 10 shows that the contribution of sources is most dominant near source, however mixing of different sources becomes more important at higher altitudes. In the further analysis of Figure 9, we have found that more dust is placed in Layer 1 in winter than summer (80 % in winter and 60 % in summer) (Figure S23). Especially, the $LOAD_k$ to LOAD ratio in Layer 2 over the Saharan Air Layer (SAL), which is over the Northern Atlantic Ocean, experiences a large seasonal change from 20 % in winter to 50 % in summer.

The vertical change in the dust distribution is analyzed with the ratio of DU_f to DU for Layers 1 ~ 4, where DU_f is the $PM_{2.5}$ size and DU is the whole size range, respectively (right column in Figure 9). In Layer 1, the global DU_f/DU values are 19 %. The lowest values appear over the source regions (<20 %) and it gradually increases during transport (>30 %), due to the faster settling of larger particle size. The strong spatial contrast of DU_f/DU diminishes as the considered layer over the source regions and the global mean values increase with layers to 27 %, 35 %, and 51 % in Layers 2, 3, and 4, respectively. The horizontal and vertical variation can be explained with the longer lifetime of DU_f than total DU.

Next, we investigate how the source contributions vary for the different layer heights (Figure 10). For the analysis, we have combined 8 dust sources to 4 larger groups of NAF

(WAF+EAF+BOD), MDECAS (MDE+CAS), EASTAK (EAS+TAK), and SOH. NAM is omitted in the figure due to its much smaller contributions, as its contribution to global loading is only 0.6 % as shown in Table 5. The source fractions in Layer 1 shows that NAF accounts for 59 % of total dust mass in that layer, followed by MDECAS (23 %) and EASTAK (6 %), which is almost the same as the column-based estimations. For Layer 1, the dust contribution of NAF is most dominant over North Africa and the Northern Atlantic Ocean with values of 80 % or greater. NAF values are also large over the Northern Pacific (20 ~ 30 %) and the Arctic (30 ~ 40 %). MDECAS dust are transported toward the east impacting the Northern Pacific (20 ~ 30 %) and the Arctic (30 ~ 40 %). The regional impact of EASTAK dust is not negligible with the values over the Northern Pacific (30 ~ 50 %) and the Arctic (20 ~ 30 %). The patterns of these larger-source contributions in Layers 2 and 3 are similar to that in Layer 1. The contributions of sources decrease by layer height over the source regions, whereas other source contributions increase over the remote area, suggesting that mixing between sources becomes more important over the remote regions and upper layers. Our estimate of EASTAK contribution to the upper free tropospheric layer (i.e., 6 ~ 12 km) (30 ~ 40 %) over the Northern Hemispheric Pacific Ocean is similar with another estimate (~40 %) using CESM/CARMA model for the upper troposphere (Froyd et al., 2022). The signature of source impact is mostly diminished in Layer 4 due the mixing between sources during the long-range transport, where NAF contribution is decreased to 47 % (by 12 % from Layer 1) and contributions from MDECAS and EASTAK increased to 30 % and 10 % (by 7 % and 4 % from Layer 1, respectively).

4.4. Seasonal variations of dust emission, deposition, and load from different source regions

The monthly mean global budget related variables are calculated for mass and F_{src} (Figure 11). Globally, total dust emission (EMI) is the highest between March and July (200 ~ 250 Tg mon^{-1}), and the lowest in November to January (~150 Tg mon^{-1}). The magnitude and pattern of deposition is similar to that of EMI. In contrast, the column loading (LOAD) has a peak in July (30 Tg) and a low from November to January (~12 Tg). The seasonality of relative contributions by different sources is clearly shown with the fraction plots (i.e., right column in Figure 11). While dust emission from the North Africa sources (WAF+EAF+BOD) constantly contributes between 50 ~ 60 % of total emission throughout the year, a notable opposite seasonal change appears between BOD and MDE or CAS, with the larger emission in the boreal winter season for BOD but summer season for MDE and CAS. On the other hand, contributions of EAS and TAK emissions are larger during the boreal spring than in other seasons, and SOH emission makes more contributions in austral spring and summer seasons. The lifetime of each dust source is ranging 1.2 days for NAM to 4.1 days for WAF, with 3.6 days for SUM. The short lifetime range among sources and the similar seasonality of DEP and LOAD to that of EMI indicate that EMI is the major driver for the seasonality of dust cycle in global scale.

5. Dust source attribution over various receptor regions

A total of 14 continental and oceanic receptor regions are predetermined to examine contributions from various sources to these regions as described in Figure 2 and summarized in Tables 6 and 7.

5.1. Dust source attributions from individual models and multi-model mean

We select 3 land (EAS, NAM, and AMZ), 2 ocean (NATL and NPAC), and 1 polar (ARC) receptor regions to compare source contribution between models (Figure 12 and 13), and the source contribution comparisons of the multi-model mean are listed in Table 6 and 7.

Among the three land receptor regions in Figure 12, EAS and NAM are either a dust source region itself or adjacent to major dust sources. Yet, they are affected not only by their own regional dust sources but also long-range transported dust. Over the receptor region EAS, most models estimate that Asian dust source regions in eastern Asia comprises more than half of the total dust load with the multi-model mean of 65 % from EAS and 12 % from TAK, whereas dust emitted over North Africa (WAF+EAF+BOD) and MDE contribute to 10 % and 12%, respectively. In comparison, most models estimate that only less than half of the dust load over NAM is from its own regional source with the multi-model mean of 24 %, while dust transported from North African sources appears to be the major contributor to supply 49 % (32 % from WAF, 11 % from EAF, and 6 % from BOD) of NAM's dust load. The rest is contributed by dust emitted over other regions with a few percent from each.

Different from EAS and NAM, AMZ does not emit dust. The dust load over AMZ is all from long-range transport. Most models agree that North Africa, especially WAF, supplies more than half the dust over AMZ with the multi-model mean of 73 % collectively from WAF (40 %), EAF

(17 %), and BOD (16 %). The rest is from SOH (13%) and other source regions. The present study estimates that the contribution of Bodélé to AMZ varies depending on models in the range from 3 % in CAM5-ATRAS to 24 % in GEOS with 139 % of diversity.

It is clearly noticeable from Figure 12 that there are significant differences in source attributions to the receptor regions among the 7 models. For example, most models estimate that more than 70 % of LOAD over the EAS receptor is from EAS and TAK sources, but GISS-OMA and SPRINTARS show their contributions less than 40%. Over NAM, GISS-OMA attributes only 6% of LOAD to NAM own source, in sharp contrast with other models' estimation of 24%-52%. Over AMZ, GEOS model shows that 92% of the LOAD is from North Africa and almost nothing from SOH, but CAM5-ATRAS estimates 47% from SOH and less than 50% from North Africa. Such large discrepancy can be partly explained by the differences in dust emissions from various source regions, but different transport efficiency may play more important role causing the remarkable differences among models in dust source attribution over downwind regions.

The source contributions for two oceanic receptor regions of NATL and NPAC and a polar region of ARC are compared in Figure 13. The multi-model consensus is that more than 90 % of the dust load over NATL is from North African with the multi-model mean of 95 % (69 % from WAF and 13 % each from EAF and BOD). However, attribution to individual source regions in North Africa is different among models, as CAM5-ATRAS and GEOS-Chem attributes >80 % of the LOAD to WAF but CESM2 and GISS-OMA designate the WAF contribution of 52 ~ 55 %. The largest difference among models is the contribution of BOD to NATL with a range spreading from 2 % from CAM5-ATRAS to 27 % from GISS-OMA and the model diversity of 107 % (Table 7).

The source attribution over NPAC is more diverse than over NATL among models. Although dust originating from eastern Asia (EAS+TAK) is considered as a major contributor for the NPAC region, the inter-model difference is significant with large spread from 18 ~19 % (GISS-OMA and SPRINTARS) to 72 % (GEOS-Chem). All models clearly show the contributions of dust from North Africa regions to the dust loading over NPAC, but the relative contribution among models is also substantially different, from 13 % (CESM2) to 58 % (SPRINTARS). Interestingly, most models (except GEOS-Chem) find a distinguishable contribution (16 ~ 29 %)

of dust from MDE+CAS to NPAC. Overall, the multi-model mean shows the contributions of dust emitted in eastern Asia (EAS+TAK), western Asia (MDE+CAS), and North Africa accounted for 32 %, 25%, and 39%, respectively, of the dust loading in NPAC with North Africa being the largest contributor.

Over the Arctic region ARC, dust from CAS and MDE arise as an outstanding contributor accounting for 36 % in the multi-model mean, which is consistent with most model estimates that fall in the range of a little over 30 %. The clear "outlier" model is CESM2 that assigns 65% of ARC dust from MDE+CAS with 60 % from CAS alone; in contrast, GEOS-Chem shows only 18% dust originating in MDE+CAS. Dust from North Africa appears still being the most important contributor to the dust over ARC with the multi-model mean of 42 %, and the range from most individual models is between 36 ~ 53 % except CESM2 (16 %). The remaining important dust source region for the ARC dust is eastern Asia (EAS+TAK), which accounts for 20 % of ARC dust load from the multi-model mean that is in the middle of the range of 17 ~ 31 % from individual model estimates. It is worth noting that the local dust from the Arctic (e.g., Bullard et al., 2016) is missing in the present study and it needs to be considered in future studies. Previous studies have estimated that the high latitude dust emission accounts for about 2 ~ 3 % of global dust emissions (Groot Zwaaftink et al., 2016; Shi et al, 2021).

The diversity of source contribution varies significantly depending on source regions and receptors (Table 6 and 7). Over land receptors, whereas the model diversity of SUM (i.e., sum of 9 sources) is ranging from 40 % in EUR to 93 % in AMZ, the diversity of various sources is ranging from 42 % (EAF in EUR) to 173 % (EAS in IND). Over ocean and polar receptors, whereas the diversity of SUM (i.e., sum of 9 sources) is ranging 45 % in NATL to 106 % in SATL, the diversity of sources is ranging from 33 % (EAS in NAPC) to 226 % (NAM in AARC). Overall, we have found a large spread between models in estimating source contributions over the various receptor regions. Depending on the region and season, the difference of relative source contribution can be a factor of more than ten.

5.2. Seasonal variations of dust source attribution over receptor regions

We examine the seasonality of dust source contribution to the dust loading (LOAD) and deposition (DEP) over the receptor regions with the multi-model monthly mean (Figure 14 and

15). There are distinctive differences in seasonal dust source contribution of LOAD in the receptor regions. For the 7 land receptor regions (see Figure 2), the NAM shows two peaks in spring (April) and summer (July-August). While the local NAM dust and the long-range transported dust from the Pacific Ocean are major sources for the NAM receptor in April, WAF is the dominant source for July-August. EUR has a peak in May, where EUR is most affected by WAF followed by EAF. The EAS receptor has two maximums in April-June and October that are mainly due to the dust emitted in EAS, and IND has a peak in May-June mainly caused by dust from CAS. Dust seasonal cycle over TNAF is controlled by dust from EAF and BOD that are stronger in March and November, and it is noted that the impact of WAF is not dominant throughout the year. Over AMZ, North African sources are dominant in spring, while the MDE and SOH source contribution is increased in summer and Fall, respectively. TAK is a dominant source over TBP between April and August when dust loading is elevated, but other dust from other source regions also makes noticeable contributions especially from CAS.

Over the broad ocean basins, both INDO and NATL show a maximum in July, dominated by dust transported from MDE for INDO and WAF for NATL. In comparison, dust over NPAC is a mixture of dust from all source regions in the northern hemisphere with a peak in spring, which is mainly because of more favorable long-range transport of dust from EAS and TAK to NPAC. In the southern hemisphere, SATL and SPAC are dominated by SOH, as expected, while the peak months are February and November over SATL and October over SPAC. The contributions from dust originating in the northern hemisphere to SATL and SPAC are mostly in the upper troposphere, as indicated in Figure 8. For the two polar regions, both show a maximum in their respective spring time, but ARC receives a mixture of dust from all regions in the northern hemisphere whereas AARC is dominated by SOH, mainly because the dust source regions in the southern hemisphere are aggregated together as SOH in this study such that the individual source contributions are not discernable.

The lifetime in ocean receptors (3.2 days in SATL ~ 6.9 days in AARC) are longer than the land receptors (1.1 days in TBP ~ 3.9 days in NTAF), which can be explained with the short lifetime of coarse dust particles in land regions and more lofted aerosol vertical distributions in remote ocean regions. A factor of 10 difference in DEP and LOAD is also found in ARC and AARC, which are far from the dust source and dominated by fine particles. Interestingly, the seasonality of DEP is notably different to LOAD over most land and ocean receptors, except for a few receptors such as TNAF and INDO. Some receptors show one or two months change of peak month in DEP from LOAD (e.g., EUR, EAS, IND, TBP, SATL, and SPAC), while some receptors shift the peak season from one to another (e.g., NAM, AMZ, ARC, and AARC). In the remaining receptors, seasonality of DEP is significantly reduced from LOAD, with more prevalent deposition throughout the year (e.g., NATL and NPAC). Although the most contributing dust sources in LOAD also appear in DEP in general (e.g., WAF in NATL), major contributing sources between LOAD and DEP are different depending on season of the year (e.g., NAM, NPAC, and ARC). Finally, contributions of DEP from nearby source regions are higher than that of LOAD in non-dust belt receptor regions (e.g., NAM, TBP, and AARC).

Figure 16 and 17 summarize the source attributions of LOAD and DEP, respectively, in all receptor regions from the multi-model mean. It shows that the magnitude of the source contribution varies depending on the location. It should be noted that the source attributions between LOAD and DEP over various receptors are different even in annual mean, which can be explained with the differences in vertical distributions and size-dependent lifetime of dust.

Overall, each receptor has a unique seasonal pattern, magnitude of LOAD and DEP, and relative contribution of sources, indicating that source contribution is non-linear and is an important factor for better understanding of the regional and global dust cycle.

6. Discussion

As stated in the Introduction section, the aims for the DUSA model experiment are twofold: (1) examine the model diversity in dust source attribution and (2) estimate the contribution of dust sources to various receptor regions from the multi-model statistics. We discuss these two aspects below.

6.1. Model diversity

Models that participated in the DUSA experiment show common features in several aspects. First, North Africa is the dominant source, accounting for 35 ~ 66 % and 44 ~ 75 % of global dust emission and column loading, respectively. Second, all models commonly show that the fractions of source region contributions to the global annual mean of dust emission, dust column loading, and DOD are similar (Figure 4), suggesting that source strength from each region determine the relative contributions to the global airborne dust amount from that region, despite the source locations. Third, models show similar features of F_{src} spatial distributions, which can be explained by common large-scale circulation patterns and convection characteristics in models, although the transport efficiency varies greatly across the models.

Meanwhile, the DUSA experiment shows remarkable differences among the models that cannot be explained just by model spatial resolution, dust particle size range, or emission magnitude. For example, CAM5-ATRAS and GEOS-Chem have similar horizontal resolution and similar maximum dust size up to 10 µm in diameter (Table 1), and both models show that dust column load is more confined near the source location (Figure 12 and 13). However, emission from CAM5-ATRAS is the highest and GEOS-Chem is the lowest among the 7 models with a factor of ~4 difference in total emission (Table 2) and a factor of ~3 in column loading. Another example shows that GFDL-AM4 and GEOS have same size bins and similar emission and deposition amounts (within ~10%), but the fraction of emissions from source regions are evidently different (Figure 4) and the lifetime of dust from GEOS ~60% longer than GFDL-AM4. Regarding the transport efficiency, GEOS-Chem and GISS-OMA show sharp contrasts (Figure 5 and 6), as GEOS-Chem usually keeps the dust close to locations near the source whereas GISS-OMA sends dust far beyond their source areas, resulted in the disparity of their source attributions in receptor regions (Figure 12 and 13).

The large differences between models can be attributed to several factors in the model physics that cannot be tracked down by the available diagnostics in the DUSA experiment. Other than using the common regional domains for tagging the dust emissions, all models have their own freedoms in simulating dust, from dust emission parameterizations to dry- and wet-removal processes, advection schemes, and dust particle configurations. In addition, differences in the meteorological fields due to the different host models are inevitable, which including horizontal and vertical advection, large- and convective precipitation, radiative flux, and surface conditions. Understanding the impact of different aerosol (including dust) parameterization and host models is important to better understand the Earth climate system and is an active research area (Hodzic et al., 2023), which requires more in-depth diagnostics such as implementing a common transport tracer to quantify the transport efficiency and a common removal tracer to analyze the removal processes in the future multi-model dust experiments.

6.2. Source attributions from multi-model mean

In the previous sections, we have discussed the contribution of various sources using multi-model mean. A few highlights of the analysis are as follows: (1) Dust from BOD accounts for about 10 % of global dust emission and loading, and it shows the largest diversity among models in all receptor regions (Table 6 and 7). Given the considerable attention on the BOD dust (Tegen et al., 1996; Koren et al., 2006; Ben-Ami et al., 2010; Yu et al., 2018), it needs more devoted studies on particularly the transport pathways of dust generated in BOD, which should have distinguishable seasonal variations from dust originating in other regions in North Africa (Figure 11 and 12; Yu et al., 2018). Although BOD is very important source region for global dust cycle, the impact of dust from Bodélé is still unsettled: While a remote sensing study estimates a strong contribution of Bodélé (~ 50 %) to the Northern Atlantic dust (Koren et al., 2006), another remote sensing study suggests only a few percent contribution of Bodélé to North America (Yu et al., 2020). In our estimation, the contribution of dust emitted from Bodélé accounts for about 13 % and 17 % to AMZ and NATL, respectively. (2) CAS dust effects over the ARC from the multi-model mean is 24 %, which is more than the contribution of dust from WAF (23 %) even though the emission amount from CAS is 43 % of that from WAF. This study has revealed the potential importance of CAS dust impact, which has drawn much less attention than other regions in the dust belt. (3) NAF makes more contribution than EAS (EAS+TAK) to dust loading over NPAC, which is also unexpected since EAS is a strong source right upwind of NPAC while most NAF dust is being transported to the west over the Atlantic. However, our study suggests that the influence of the EAS dust is more significant over the extra-tropical NPAC but NAF dust dominates the dust loading in the tropical eastern NPAC via westward transport (Figure 10, Figure S4-S6 vs. Figure S9-S10). (4) ARC and NPAC receives a mixture of dust from all regions with no clear outstanding dominant source in terms of column loading, however the relative importance of each source depends not only on geographic locations (latitude and longitude) but also on altitudes (Figure 10; Figure S13-S21). (5) Diversities of SOH source contribution among models exceed 100% in most receptor regions. Because this study lumps the dust source regions in the southern hemisphere together, it is not allowed to diagnose the model differences regarding individual dust sources there. Better designed model experiments with southern hemispheric dust attribution can be considered in future modeling studies.

6.3. Comparisons of global dust source attributions with previous studies

While we have used the multi-model ensemble to estimate the source attribution in this AeroCom-III/DUSA experiment, a similar study has been conducted with an inverse modeling method for DustCOMM and AeroCom-I (Kok et al., 2021a,b). The three estimations have similarity in the overall picture with some differences, considering differences in participating models, differences in methods, and time periods (Figure 18). DUSA estimates that North Africa sources contribute about 60 % of the global dust loading, which is about 10 % larger than DustCOMM and 5 % less than AeroCom-I. These methods all agree that MDECAS and EASTAK are the second and third sources, respectively, for the global dust loading, however DustCOMM estimations are about 5 ~ 10 % larger than DUSA and 2 ~ 5 % larger than AeroCom-I. The three estimations agree that NAM source is marginal, accounting for 0 ~ 3 % for global loading. DUSA attributes about 10 % of global dust loading to SOH source, which is 3 % and 5 % larger than DustCOMM and AeroCom-I, respectively. Both DUSA and DustCOMM commonly show summer peak of dust emission in NAF and MDECAS, and spring peak of dust emission in EASTAK and NAM. While these differences can come from simulations done for different time periods with different analysis methods, it also suggests that the results can vary by participating models or model versions. Unfortunately, currently there are no adequate, reliable observations to offer definitive evaluations of dust source attributions.

6.4. Recommendations for future studies

Although correctly estimating dust source attribution is an important subject to better understand the role of dust to the global and regional climate, the present study has revealed a large diversity between models. Unfortunately, there are no direct observations available for evaluating the dust source attributions. Furthermore, the large model differences in dust source attribution cannot be resolved by a simple global tuning factor for total dust emission or DOD. This finding has an implication that improving dust source attribution is an important task for future global dust modeling.

Based on the present and our previous works (e.g., Kim et al., 2014, 2019), we make the following suggestions toward having more process-level diagnostics of inter-model differences and more observation-based constraints of dust modeling. On the observation side, it is desirable to establish and maintain ground-based networks or mobile observation programs measuring the seasonal cycle of size-resolved dust mass concentrations, deposition fluxes, and optical properties over major dust source regions as well as receptor regions. Measurements over the source regions can help better estimate freshly emitted dust amount, which are rarely directly observable, to improve the emission parameterizations used by the models, whereas the measurements over the receptor regions can help evaluate the model transport and deposition processes that are connected to the source locations near and far.

On the multi-modeling side, more process-level diagnostics are needed to better determine the major factors causing the model diversities. For example, parameters determine dust emissions should be assessed to include the winds or friction velocities, soil moisture and texture, and erodibility that depends on vegetation cover and ephemeral rivers and lakes as potential dust source; parameters associated with dust removal should be assessed to include size-dependent settling velocity, convective and large-scale precipitation, and scavenging efficiency for rainout and washout processes. Finally, differences in atmospheric circulations between hosting models need to be examined to analyze the differences in dust transport; in that regard, implementation of a suitable common transport tracer may help quantify the inter-model differences in transport patterns of both advection and convection.

There are distinguishable differences in dust mineralogy between sources, for example, the Bodélé depression (very white dust), the Sahara ("average" dust), and Australia (red dust), which motivate the NASA Earth Surface Mineral Dust Source Investigation (EMIT) mission to have high-quality global mineralogy map from the space measurement (Green et al., 2020). Also, understanding the modern-day source apportionment is a prerequisite for understanding how dust has changed in the past since deposition records tend to measure regional dust. More careful consideration of dust source attribution would be required for these studies.

7. Conclusions

In the present study, we have investigated the relative contribution of various dust sources in the Earth's atmospheric system using multi-model analysis from 7 global models that participated in the AeroCom-III DUSA experiment. Each model simulated the BASE run and a series of runs with 9 tagged regions for 2009-2012 to estimate the contribution of dust in the atmosphere that are emitted from broad regions of East- and West-Africa, Middle East, Central- and East-Asia, North America, and the Southern Hemisphere, as well as from prominent dust hot spots of the Bodélé and Taklimakan Deserts. For source-receptor relationships, we defined 14 receptor regions across the globe, consisting of 7 land regions, 5 ocean regions, and 2 polar regions. In addition to the individual models, we have generated the multi-model mean of 3-dimensional distribution of dust concentration and source contribution. Whereas observational data to evaluate dust source contribution in models is absent, the comparison of model DOD with the 55 AERONET retrieved coarse-mode AOD data as a proxy of DOD showed that the correlation coefficients between model-calculated DOD and AERONET coarse-mode AOD are from 0.4 to 0.8 with considerable spread of the agreement for spatial and temporal variability across the AERONET sites.

The multi-model analysis has revealed large model diversity of dust emission, loading, and deposition on both global and regional scales. The result indicated that differences in regional dust emission is the first order factor to explain the diversities of global mean dust load, DOD, and deposition among models. Further analysis reveals that the relative dust source strength from various sources is strongly model-dependent. Qualitatively, all models showed that the dust load over the dust-belt regions are dominated by their local sources such as North Africa, Middle East, and/or Asian sources. However, some models show that contribution of a source is much stronger (e.g., SOH in CESM2) or weaker (e.g., WAF in CESM2 and BOD in GISS-OMA) than other models. Horizontal and vertical distribution of source contribution is also substantially different among models, with some models (e.g., GISS-OMA) more effectively transporting dust than other models (e.g., GEOS-Chem). Quantitatively, the inter-model differences are significant with the model diversity in 30 - 50 % for global, annual averaged quantities of total dust emission, deposition, column load, and lifetime, but the differences in regional and seasonal scales are much larger.

The study has estimated the large diversity values depending on source regions and receptors. Whereas the diversity of total dust load is 40 ~ 93 % over land receptors and 45 ~ 106 % over ocean and polar receptors, the diversity of contributions from different source regions are 42 ~ 173 % over land receptors and 33 ~ 226 % over ocean and polar receptors. The widespread diversity values suggest that there is a large disparity in simulating dust cycles among models.

We have quantitatively estimated source contribution using the multi-model mean of 3-dimensional distribution of monthly dust column loading and source contribution in the global scale and various receptor regions. Overall, the multi-model mean shows that North Africa and MDE contribute about three quarters of global dust loading (~75 %). Dust from the North Africa and MDE sources are mainly transported toward both west and east directions, affecting the Northern Atlantic Ocean and the Northeast Pacific Ocean. CAS contributes 8.8 % of global loading, however it is an important source in the lower troposphere over mid-latitudes and the Arctic. EAS and TAK are significant sources for the Pacific Ocean (32%), although their global contribution is only 5.6 %. NAM dust contribution is confined near the source region, with the global contribution of 0.6 %. The inter-hemispheric transport is not strong column-wise, such that the SOH sources are the most important over the Southern Hemisphere (>70%), with the global contribution of 10.4 %. On the other hand, dust from both hemispheres are better mixed at higher altitudes in the upper-troposphere and lower-stratosphere, although the concentrations are in orders of magnitudes lower than that in the planetary boundary layer.

Multi-model mean analysis showed that the vertical distribution of source contributions is strongly source dependent. North Africa and MDE sources contribute most to the northern hemisphere in most latitudes and altitudes due to the strong convection, source strength, and large-scale circulation. Other sources also make significant contributions to certain regions of the Earth, such as the Arctic (e.g., CAS), high-altitude (e.g., TAK), and southern hemisphere by (e.g., SOH). In the 4-layer analysis of F_{src}, it is found that about 95 % of dust mass is located below 6 km and 72 % below 2.5 km.

The source contribution in column loading is not necessarily the same as deposition, rather the present study showed quite different results between two variables, as dust deposition is more responding to the dust load in the lower atmosphere closer to the surface, therefore the dust from nearby source locations contributes more to the deposition than to the column loading. Overall, dust over receptor regions immediate downwind of nearby source are dominated by dust emitted in the upwind source regions, whereas over remote land, ocean, and polar regions dust are a mixture from various sources around the globe.

Finally, we show that the large model differences in dust source attribution cannot be resolved with a simple global tuning factor, rather it requires more comprehensive studies. Based on the present and past studies, we suggest some actions toward more process-level diagnostics of inter-model differences and more observation-based constraints, including satellite, of dust modeling.

Acknowledgements

We thank NASA CALIPSO, ISFM, and MAP for the funding support, AERONET teams for the data used in this study, and AeroCom for handling model simulations. Computational resources supporting this work were provided by the NASA High-End Computing (HEC) Program through the NASA Center for Climate Simulation (NCCS) at Goddard Space Flight Center. HM was supported by the Ministry of Education, Culture, Sports, Science, and Technology and the Japan Society for the Promotion of Science (MEXT/JSPS) KAKENHI Grant Numbers, JP20H00196, JP22H03722, JP23H00515, JP23H00523, JP23K18519, JP23K24976, and JP24H02225; by the MEXT Arctic Challenge for Sustainability II (ArCS II) Project (JPMXD1420318865); and by the Environment Research and Technology Development Fund 2–2301 (JPMEERF20232001) of the Environmental Restoration and Conservation Agency. Kok has been supported by the NSF (grant nos. ATM 1856389 and 2151093).

Data Availability Statement

AERONET data are available at https://aeronet.gsfc.nasa.gov/ and AeroCom model simulations are available at http://aerocom.met.no/. Deposition data is available at Albani et al. (2014).

References

Albani, S., Mahowald, N. M., Perry, A. T., Scanza, R. A., Zender, C. S., Heavens, N. G., Maggi, V., Kok, J. F., & Otto-Bliesner, B. L. (2014). Improved dust representation in the Community Atmosphere Model. Journal of Advances in Modeling Earth Systems, 6, 541-570. https://doi.org/10.1002/2013MS000279.

Bauer, S. E. & D. Koch (2005). Impact of heterogeneous sulfate formation at mineral dust surfaces on aerosol loads and radiative forcing in the Goddard Institute for Space Studies general circulation model, *J. Geophys. Res*., 110, D17202, doi:10.1029/2005JD005870.

Bauer, S. E., Im, U., Mezuman, K., & Gao, C. Y. (2019). Desert dust, industrialization, and agricultural fires: Health impacts of outdoor air pollution in Africa. Journal of Geophysical Research: Atmospheres, 124, 4104–4120. https://doi.org/10.1029/2018JD029336.

Ben-Ami, Y., Koren, I., Rudich, Y., Artaxo, P., Martin, S. T., &Andreae, M. O. (2010). Transport of North African dust from the Bodélé depression to the Amazon Basin: a case study, Atmos. Chem. Phys., 10, 7533–7544, https://doi.org/10.5194/acp-10-7533-2010.

Bey, I., Jacob, D. J., Yantosca, R. M., Logan, J. A., Field, B. D., Fiore, A. M., Li, Q., Liu, H. Y., Mickley, L. J., &Schultz, M. G. (2001). Global modeling of tropospheric chemistry with assimilated meteorology: Model description and evaluation, J. Geophys. Res., 106(D19), 23073– 23095, doi:10.1029/2001JD000807.

Bullard, J. E., et al. (2016). High-latitude dust in the Earth system, Rev. Geophys., 54, 447–485, doi:10.1002/2016RG000518.

Capelle, V., Chédin, A., Pondrom, M., Crevoisier, C., Armante, R., Crepeau, L., & Scott, N. A. (2018). Infrared dust aerosol optical depth retrieved daily from IASI and comparison with AERONET over the period 2007–2016. Rem. Sens. Env., 206, 15-32.

Checa-Garcia, R., Balkanski, Y., Albani, S., Bergman, T., Carslaw, K., Cozic, A., Dearden, C., Marticorena, B., Michou, M., Van Noije, T., Nabat, P., O'Connor, F. M., Olivié, D., Prospero, J. M., Le Sager, P., Schulz, M., & Scott, C. (2021). Evaluation of natural aerosols in CRESCENDO Earth system models (ESMs): Mineral dust. Atmospheric Chemistry and Physics, 21(13), 10295-10335. https://doi.org/10.5194/acp-21-10295-2021.

Chin, M., et al. (2002). Tropospheric aerosol optical thickness from the GOCART model and comparisons with satellite and Sun photometer measurements, *J. Atmos. Sci*., 59, 461–483.

Chin, M., Diehl, T., Dubovik, O., Eck, T. F., Holben, B. N., Sinyuk, A., & Streets, D. G. (2009). Light absorption by pollution, dust and biomass burning aerosols: A global model study and evaluation with AERONET data, *Ann. Geophys.*, *27*, 3439-3464.

Colarco, P. R., Nowottnick, E. P., Randles, C. A., Yi, B., Yang, P., Kim, K.-M., Smith, J. A., & Bardeen, C. G. (2014). Impact of radiatively interactive dust aerosols in the NASA GEOS-5 climate model: Sensitivity to dust particle shape and refractive index, J. Geophys. Res. Atmos., 119, 753–786, doi:10.1002/2013JD020046.

Creamean, J. M., Suski, K. J., Rosenfeld, D., Cazorla, A., De- Mott, P. J., Sullivan, R. C., White, A. B., Ralph, F. M., Minnis, P., Comstock, J. M., Tomlinson, J. M., & Prather, K. A. (2013). Dust and Biological Aerosols from the Sahara and Asia Influence Precipitation in the Western U.S., Science, 339, 1572–1578, https://doi.org/10.1126/science.1227279.

DeMott, P. J., Prenni, A. J., Liu, X., Kreidenweis, S. M., Petters, M. D., Twohy, C. H., Richardson, M. S., Eidhammer, T., & Rogers, D. C. (2010). Predicting global atmospheric ice nuclei distributions and their impacts on climate, Proc. Natl. Acad. Sci. U.S.A., 107, 11,217–11,222.

Di Biagio, C., Formenti, P., Balkanski, Y., Caponi, L., Cazaunau, M., Pangui, E., Journet, E., Nowak, S., Caquineau, S., Andreae, M. O., Kandler, K., Saeed, T., Piketh, S., Seibert, D., Williams, E., & Doussin, J.-F. (2017). Global scale variability of the mineral dust long-wave refractive index: a new dataset of in situ measurements for climate modeling and remote sensing, Atmos. Chem. Phys., 17, 1901–1929, https://doi.org/10.5194/acp-17-1901-2017.

Engelbrecht, J. P., Moosmüller, H., Pincock, S., Jayanty, R. K. M., Lersch, T., & Casuccio, G. (2016). Technical note: Mineralogical, chemical, morphological, and optical interrelationships of mineral dust re-suspensions, Atmos. Chem. Phys., 16, 10809–10830, https://doi.org/10.5194/acp-16-10809-2016, 2016.

Evan, A. T., Heidinger, A. K., Bennartz, R., Bennington, V., Mahowald, N. M., Corrada-Bravo, H., Velden, C. S., Myhre, G., & Kossin, J. P. (2008). Ocean temperature forcing by aerosols across the Atlantic tropical cyclone development region. Geochem. Geophy. Geosy., 9, Q05V04. doi:10.1029/2007GC001774.

Formenti, P., Caquineau, S., Desboeufs, K., Klaver, A., Chevaillier, S., Journet, E., & Rajot, J. L. (2014) Mapping the physicochemical properties of mineral dust in western Africa: mineralogical composition, Atmos. Chem. Phys., 14, 10663–10686, doi:10.5194/acp-14-10663-2014, 2014.

Forster, P., Ramaswamy, V., Artaxo, P., Berntsen, T., Betts, R., Fahey, D. W., Haywood, J., Lean, J., Lowe, D. C., Myhre, G., Nganga, J., Prinn, R., Raga, G., Schulz, M., & Van Dorland, R. (2007). Changes in Atmospheric Constituents and in Radiative Forcing, in: Climate Change 2007: The Physical Science Basis, contribution of Working Group I to the Fourth Assessment Report of the Intergovernmental Panel on Climate Change, edited by: Solomon, S. D., Qin, M., Manning, Z., Chen, M., Marquis, K. B., Averyt, M. T., and Miller, H. L., Cambridge University Press, Cambridge, United Kingdom and New York, NY, USA, 129–234.

Froyd, K. D., Yu, P., Schill, G. P., Brock, C. A., Kupc, A., Williamson, C. J., et al. (2022). Dominant role of mineral dust in cirrus cloud formation revealed by global-scale measurements. Nature Geoscience, 15, 177–183. https://doi.org/10.1038/s41561-022-00901-w.

Gillette, D. (1978). A wind tunnel simulation of the erosion of soil: Effect of soil texture, sandblasting, wind speed, and soil consolidation on dust production. Atmos. Environ.,12, 1735–1743.

Gillette, D. A., Marticorena, B., & Bergametti, G. (1998). Change in the aerodynamic roughness height by saltating grains: Experimental assessment, test of theory, and operational parameterization. Journal of Geophysical Research, 103(D6), 6203– 6209.

Ginoux, P., et al. (2001). Sources and distributions of dust aerosols simulated with the GOCART model, *J. Geophys. Res*., *106*(D17), 20,255–20,273.

Ginoux, P., J. M. Prospero, T. E. Gill, N. C. Hsu, & M. Zhao (2012). Global-scale attribution of anthropogenic and natural dust sources and their emission rates based on MODIS Deep Blue aerosol products, Rev. Geophys., 50, RG3005, doi:10.1029/2012RG000388.

Green, R. O., Mahowald, N., Ung, C., Thompson, D. R., Bator, L., Bennet, M., Bernas, M., Blackway, N., Bradley, C., Cha, J., Clark, P., Clark, R., Cloud, D., Diaz, E., Ben Dor, E., Duren, R., Eastwood, M., Ehlmann, B. L., Fuentes, L., Ginoux, P., Gross, J., He, Y., Kalashnikova, O., Kert, W., Keymeulen, D., Klimesh, M., Ku, D., Kwong-Fu, H., Liggett, E., Li, L., Lundeen, S., Makowski, M. D., Mazer, A., Miller, R., Mouroulis, P., Oaida, B., Okin, G. S., Ortega, A., Oyake, A., Nguyen, H., Pace, T., Painter, T. H., Pempejian, J., Pérez García-Pando, C., Pham, T., Phillips, B., Pollock, R., Purcell, R., Realmuto, V., Schoolcraft, J., Sen, A., Shin, S., Shaw, L., Soriano, M., Swayze, G., Thingvold, E., Vaid, A., & Zan, J. (2020). The Earth Surface Mineral Dust Source Investigation: An Earth Science Imaging Spectroscopy Mission, in: 2020 IEEE Aerospace Conference, Big Sky, MT, USA, 1–14 March, 1–15, https://doi.org/10.1109/AERO47225.2020.9172731.

Groot Zwaaftink, C. D., H. Grythe, H. Skov, and A. Stohl (2016), Substantial contribution of northern high-latitude sources to mineral dust in the Arctic, J. Geophys. Res. Atmos., 121, 13,678–13,697, doi:10.1002/ 2016JD025482.

Hamilton, D. S., Moore, J. K., Arneth, A., Bond, T. C., Carslaw, K. S., Hantson, S., et al. (2020). Impact of changes to the atmospheric soluble iron deposition flux on ocean biogeochemical cycles in the Anthropocene. Global Biogeochemical Cycles, 34, e2019GB006448. https://doi.org/10.1029/2019GB006448.

Hand, J. L., T. E. Gill, and B. A. Schichtel (2017), Spatial and seasonal variability in fine mineral dust and coarse aerosol mass at remote sites across the United States, J. Geophys. Res. Atmos., 122, 3080–3097, doi:10.1002/2016JD026290.

Haywood, J. M., Allan, R. P., Culverwell, I., Slingo, A., Milton, S., Edwards, J., & Clerbaux, N., (2005). Can desert dust explain the outgoing longwave radiation anomaly over the Sahara during July 2003?, J. Geophys. Res., 110, D05105. doi:10.1029/2004JD005232.

Hodzic, A., Mahowald, N., Dawson, M., Johnson, J., Bernardet, L., Bosler, P., Fast, J., Fierce, L., Liu, X., Ma, P., Murphy, B., Riemer, N. & Schulz, M. (2023). GeneralIzed Aerosol/chemistry iNTerface (GIANT): a community effort to advance collaborative science across weather and climate models. To be published in Bulletin of the American Meteorological Society . https://doi.org/10.1175/BAMS-D-23-0013.1

Holben, B. N., Eck, T. F., Slutsker, I., Tanre, D., Buis, J. P., Setzer, A., Vermote, E., Reagan, J. A., Kaufman, Y. J., Nakajima, T., Lavenu, F., Jankowiak, F., & Smirnov, A. (1998). AERONET – A federated instrument network and data archive for aerosol characterization, *Remote Sens. Environ*., 66, 1–16.

Huneeus, N., Schulz, M., Balkanski, Y., Griesfeller, J., Prospero, J., Kinne, S., Bauer, S., Boucher, O., Chin, M., Dentener, F., Diehl, T., Easter, R., Fillmore, D., Ghan, S., Ginoux, P., Grini, A., Horowitz, L., Koch, D., Krol, M. C., Landing, W., Liu, X., Mahowald, N., Miller, R., Morcrette, J.-J., Myhre, G., Penner, J., Perlwitz, J., Stier, P., Takemura, T., & Zender, C. S. (2011). Global dust model intercomparison in AeroCom phase I, *Atmos. Chem. Phys*., 11, 7781-7816, doi:10.5194/acp-11-7781-2011.

Jickells, T. D., et al., (2005). Global iron connections between desert dust, ocean biogeochemistry, and climate. Science, 308, 67–71.

Jordan, A. K., Zaitchik, B. F., Gnanadesikan, A., Kim, D., & Badr, H. S. (2020). Strength of linkages between dust and circulation over North Africa: Results from a coupled modeling system with active dust. Journal of Geophysical Research: Atmospheres, 125, e2019JD030961. https://doi.org/10.1029/2019JD030961

Kawai, K., Matsui, H., & Tobo, Y. (2023). Dominant role of Arctic dust with high ice nucleating ability in the Arctic lower troposphere. Geophysical Research Letters, 50, e2022GL102470. https://doi. org/10.1029/2022GL102470

Kim, D., Chin, M., Yu, H., Diehl, T., Tan, Q., Tsigaridis, K., Bauer, S. E., Takemura, T., Pozzoli, L., Bellouin, N., Schulz, Peyridieu, M., S., & Chédin A. (2014). Source, sinks, and transatlantic transport of North African dust aerosol: A multi-model analysis and comparison with remote-sensing data, *J. Geophy. Res. Atmos*., 119, 6259–6277, doi:10.1002/2013JD021099.

Kim, D., Chin, M., Yu, H., Pan, X., Bian, H., Tan, Q., Kahn, R. A., Tsigaridis, K., Bauer, S. E., Takemura, T., Pozzoli, L., Bellouin, N., & Schulz, M. (2019). Asian and trans-Pacific Dust: A multi-model and multi-remote sensing observation analysis, *J. Geophy. Res. Atmos*., 124. https://doi.org/10.1029/2019JD030822

Kim, D., Chin, M., Cruz, C. A., Tong, D., & Yu, H. (2021). Spring dust in western North America and its interannual variability—Understanding the role of local and transported dust. Journal of Geophysical Research: Atmospheres, 126, e2021JD035383. https://doi.org/10.1029/2021JD035383

Kok, J. F., Ridley, D. A., Zhou, Q., Miller, R. L., Zhao, C., Heald, C. L., Ward, D. S., Albani, S., & Haustein, K. (2017) Smaller desert dust cooling effect estimated from analysis of dust size and abundance, Nat. Geosci., 10, 274–278.

Kok, J. F., Adebiyi, A. A., Albani, S., Balkanski, Y., Checa-Garcia, R., Chin, M., Colarco, P. R., Hamilton, D. S., Huang, Y., Ito, A., Klose, M., Leung, D. M., Li, L., Mahowald, N. M., Miller, R. L., Obiso, V., Pérez García-Pando, C., Rocha-Lima, A., J. Wan, S., & Whicker, C. A. (2021a). Improved representation of the global dust cycle using observational constraints on dust properties and abundance, Atmospheric Chemistry and Physics, 21, 8127-67.

Kok, J. F., Adebiyi, A. A., Albani, S., Balkanski, Y., Checa-Garcia, R., Chin, M., Colarco, P. R., Hamilton, D. S., Huang, Y., Ito, A., Klose, M., Li, L., Mahowald, N. M., Miller, R. L., Obiso, V., Pérez García-Pando, C., Rocha-Lima, A., & Wan, J. S. (2021b). Contribution of the world's main dust source regions to the global cycle of desert dust, Atmospheric Chemistry and Physics, 21, 8169-93.

Kok, J. F., Storelvmo, T., Karydis, V. A., Adebiyi, A. A., Mahowald, N. M., Evan, A. T., He, C., & Leung, D. M. (2023). Mineral dust aerosol impacts on global climate and climate change, Nature Reviews Earth & Environment, https://doi.org/10.1038/s43017-022-00379-5.

Koren, I., Kaufman, Y. J., Washington, R., Todd, C. C., Rudich, Y., Martins, J. V., & Rosenfeld, D. (2006). The Bodélé depression: a single spot in the Sahara that provides most of the mineral dust to the Amazon forest, Environ. Res. Lett., 1, 1–5.

Leung, D. M., Kok, J. F., Li, L., Mahowald, N. M., Lawrence, D. M., Tilmes, S., Kluzek, E., Klose, M., & Pérez García-Pando, C. (2024). A new process-based and scale-aware desert dust emission scheme for global climate models – Part II: Evaluation in the Community Earth System Model version 2 (CESM2), Atmos. Chem. Phys., 24, 2287–2318, https://doi.org/10.5194/acp-24-2287-2024.

Liu, X., Easter, R. C., Ghan, S. J., Zaveri, R., Rasch, P., Shi, X., et al. (2012). Toward a minimal representation of aerosols in climate models: Description and evaluation in the Community Atmosphere Model CAM5. Geoscientific Model Development, 5(3), 709–739. https://doi.org/10.5194/gmd-5-709-2012

Liu, X., Ma, P.-L., Wang, H., Tilmes, S., Singh, B., Easter, R. C., Ghan, S. J., & Rasch, P. J. (2016) Description and evaluation of a new four-mode version of the Modal Aerosol Module (MAM4) within version 5.3 of the Community Atmosphere Model, Geosci. Model Dev., 9, 505–522, https://doi.org/10.5194/gmd-9-505-2016.

Macpherson, T., Nickling, W. G., Gillies, J. A., & Etyemezian, V. (2008). Dust emissions from undisturbed and disturbed supply-limited desert surfaces, J. Geophys. Res., 113, F02S04, doi:10.1029/2007JF000800.

Maher, B. A., Prospero, J. M., Mackie, D., Gaiero, D., Hesse, P., & Balkanski, Y. (2010). Global connections between aeolian dust, climate and ocean biogeochemistry at the present day and at the last glacial maximum. 99, 1–2, 61–97. doi:10.1016/j.earscirev.2009.12.001.

Mahowald, N. M., Baker, A. R., Bergametti, G., Brooks, N., Duce, R. A., Jickells, T. D., Kubilay, N., Prospero, J. M., v Tegen, I. (2005). Atmospheric global dust cycle and iron inputs to the ocean, Global Biogeochem. Cycles, 19, GB4025, doi:10.1029/2004GB002402.

Marticorena, B., & G. Bergametti (1995). Modeling the atmospheric dust cycle: 1. Design of a soil-derived dust emission scheme, J. Geophys. Res., 100, 16,415–16,430.

Marticorena, B., Bergametti, G., Aumont, B., Callot, Y., N'Doume, C., & Legrand, M. (1997). Modeling the atmospheric dust cycle: 2 simulation of Saharan dust sources. J. Geophys. Res. 102D, 4387–4404.

Matsui H, Koike M, Kondo Y, Fast JD, & Takigawa M. (2014). Development of an aerosol microphysical module: Aerosol Two-dimensional bin module for foRmation and Aging Simulation (ATRAS) Atmos. Chem. Phys.,14, 10315–10331. doi: 10.5194/acp-14-10315-2014.

Matsui, H. (2017). Development of a global aerosol model using a two dimensional sectional method: 1. Model design, J. Adv. Model. Earth Syst., 9, 1921–1947, doi:10.1002/2017MS000936.

Matsui, H. & Mahowald, N. (2017). Development of a global aerosolmodel using a two-dimensionalsectional method: 2. Evaluation andsensitivity simulations,J. Adv. Model.Earth Syst.,9, 1887–1920, doi:10.1002/2017MS000937.

Miller, R. L., et al. (2006). Mineral dust aerosols in the NASA Goddard Institute for Space Sciences ModelE atmospheric general circulation model, *J. Geophys. Res*., 111, D06208, doi:10.1029/2005JD005796.

O'Neill, N. T., Eck, T. F., Smirnov, A., Holben, B. N., & Thulasiraman, S. (2003). Spectral discrimination of coarse and fine mode optical deph, J. Geophys. Res., 108(D17), 4559, doi:10.1029/2002JD002975.

Rosenfeld, D., et al. (2014). Global observations of aerosol-cloud-precipitation climate interactions, Rev. Geophys., 52, doi:10.1002/2013RG000441.

Schulz, M., Textor, C., Kinne, S., Balkanski, Y., Bauer, S., Berntsen, T., Berglen, T., Boucher, O., Dentener, F., Guibert, S., Isaksen, I. S. A., Iversen, T., Koch, D., Kirkevåg, A., Liu, X., Montanaro, V., Myhre, G., Penner, J. E., Pitari, G., Reddy, S., Seland, Ø., Stier, P., & Takemura, T. (2006). Radiative forcing by aerosols as derived from the AeroCom present-day and pre-industrial simulations, Atmos. Chem. Phys., 6, 5225–5246, https://doi.org/10.5194/acp-6-5225-2006.

Shao, Y., Wyrwoll, K.-H., Chappell, A., Huang, J., Lin, Z., McTainsh, G. H., Mikami, M., Tanaka, T. Y., Wang, X., & Yoon, S. (2011). Dust cycle: An emerging core theme in Earth system science, Aeolian Res., 2(4), 181–204, doi:10.1016/j.aeolia.2011.02.001.

Shi, Y., & Liu, X. (2019). Dust radiative effects on climate by glaciating mixed-phase clouds. Geophysical Research Letters, 46, 6128-6137. https://doi.org/10.1029/2019GL082504

Shi, Y., Liu, X., Wu, M., Zhao, X., Ke, Z., & Brown, H. (2022). Relative importance of high-latitude local and long-range-transported dust for Arctic ice-nucleating particles and impacts on Arctic mixed-phase clouds, Atmos. Chem. Phys., 22, 2909–2935, https://doi.org/10.5194/acp-22-2909-2022.

Takemura, T., Okamoto, H., Maruyama, Y., Numaguti, A., Higurashi A., & Nakajima, T. (2000). Global three-dimensional simulation of aerosol optical thickness distribution of various origins, *J. Geophys. Res*., 105, 17,853 – 17,873.

Takemura, T., Nozawa T., Emori S., Nakajima T. Y., & Nakajima T. (2005). Simulation of climate response to aerosol direct and indirect effects with aerosol transport-radiation model, *J. Geophys. Res*., 110, D02202, doi:10.1029/2004JD005029.

Tegen, I., & Fung, I. (1995). Contribution to the atmospheric mineral aerosol load from land surface modification, J. Geophys. Res., 100, 18,707-18,726.

Tegen, I., Lacis, A., & Fung, I. (1996). The influence on climate forcing of mineral aerosols from disturbed soils, Nature, 380, 419–422.

Textor, C., Schulz, M., Guibert, S., Kinne, S., Balkanski, Y., Bauer, S., Berntsen, T., Berglen, T., Boucher, O., Chin, M., Dentener, F., Diehl, T., Easter, R., Feichter, H., Fillmore, D., Ghan, S., Gi- noux, P., Gong, S., Grini, A., Hendricks, J., Horowitz, L., Huang, P., Isaksen, I., Iversen, T., Kloster, S., Koch, D., Kirkevag, A., Kristjansson, J. E., Krol, M., Lauer, A., Lamarque, J. F., Liu, X., Montanaro, V., Myhre, G., Penner, J., Pitari, G., Reddy,S., Seland, Ø., Stier, P., Takemura, T., and Tie, X. (2006). Analysis and quantification of the diversities of aerosol life cycles within AeroCom, Atmos. Chem. Phys., 6, 1777–1813, http://www.atmos-chem-phys.net/6/1777/2006/.

Westberry, T. K., Behrenfeld, M. J., Shi, Y. R., Yu, H., Remer, L. A., & Bian, H. (2023). "Atmospheric nourishment of global ocean ecosystems." Science 380 (6644): 515-519. https://doi.org/10.1126/science.abq5252

Wu, M., Liu, X., Yu, H., Wang, H., Shi, Y., Yang, K., Darmenov, A., Wu, C., Wang, Z., Luo, T., Feng, Y., & Ke, Z. (2020). Understanding processes that control dust spatial distributions with global climate models and satellite observations, Atmos. Chem. Phys., 20, 13835–13855, https://doi.org/10.5194/acp-20-13835-2020.

Yu, H., Chin, M., Yuan, T., Bian, H., Remer, L. A., Prospero, J. M., Omar, A., Winker, D., Yang, Y., Zhang, Y., Zhang, Z., & Zhao, C. (2015). The fertilizing role of African dust in the Amazon rainforest: A first multiyear assessment based on data from Cloud-Aerosol Lidar and Infrared Pathfinder Satellite Observations, Geophys. Res. Lett., 42, doi:10.1002/2015GL06304.

Yu, Y., Kalashnikova, O. V., Garay, M. J., Lee, H., & Notaro, M. (2018). Identification and characterization of dust source regions across North Africa and the Middle East using MISR satellite observations. Geophysical Research Letters, 45, 6690–6701. https://doi.org/10.1029/2018GL078324

Yu, Y., Kalashnikova, O. V., Garay, M. J., Lee, H., Notaro, M., Campbell, J. R., et al. (2020). Disproving the Bodélé depression as the primary source of dust fertilizing the Amazon Rainforest. Geophysical Research Letters, 47, e2020GL088020. https://doi.org/10.1029/2020GL088020

Zhao, M., Golaz, J.-C., Held, I. M., Guo, H., Balaji, V., Benson, R., et al. (2018). The GFDL global atmosphere and land model AM4.0/LM4.0: 1. Simulation characteristics with prescribed SSTs. Journal of Advances in Modeling Earth Systems, 10, 691–734. https://doi.org/10.1002/2017MS001208

Zender, C. S., D. Newman, and O. Torres (2003), Spatial heterogeneity in aeolian erodibility: Uniform, topographic, geomorphologic, and hydrologic hypotheses, J. Geophys. Res., 108(D17), 4543, doi:10.1029/2002JD003039.

Figure Captions

Figure 1. Map of dust sources for model simulation and analysis. The color shade is the annual mean dust emission of the GEOS model for 2009~2012. Source regions are color coded as shown below the map. Source regions are West Africa (WAF), East Africa (EAF), Bodélé (BOD), Central Asia (CAS), Middle East (MDE), East Asia (EAS), Taklimakan desert (TAK), North America (NAM), and Southern Hemisphere (SOH).

Figure 2. Map of dust receptors. Seven receptors are located over land and the remaining receptors cover ocean or polar regions. The receptor names are North America (NAM), Europe (EUR), India (IND), East Asia (EAS), Tropical North Africa (TNAF), Amazon (TMZ), Tibetan Plateau (TBP), North Atlantic (NATL), South Atlantic (SATL), North Pacific (NPAC), South Pacific (SPAC), Indian Ocean (INDO), Arctic (ARC), and Antarctic (AARC).

Figure 3. Comparisons of dust optical depths at 550 nm between AERONET and model averaged for 2009 and 2012. (a) Mean and standard deviation of AERONET and model, and (b) Taylor diagram of DOD from the AERONET and the models. (c) Map of multi-model mean DOD. AERONET DOD is overplotted in circle.

Figure 4. Percent contributions by mass of dust sources in global dust emission (EMI), column loading (LOAD), and dust optical depth (DOD).

Figure 5. Horizontal distribution of F_{src} (contribution of WAF; brown shade) and dust column loading (LOAD) (black contour lines at 5, 20, 50, 200, 500 mg m^{-2}) for WAF. Numbers in parenthesis are the area-weighted global mean of F_{src} (left) and LOAD (right).

Figure 6. Vertical distribution of F_{src} (contribution of WAF; brown shade) and dust concentration (black contour lines at 0.1, 0.2, 0.5, 1, 2, 5, 10 μg m^{-3}) for WAF.

Figure 7. Horizontal distribution of multi-model mean F_{src} (contribution of sources; brown shade) and column dust loading (black contour lines at 5, 20, 50, 200, 500 mg m^{-2}). Numbers in parenthesis are the area-weighted global mean of F_{src} (left) and LOAD (right).

Figure 8. Vertical distribution of multi-model mean F_{src} (contribution of sources; brown shade) and dust concentration (black contour lines at 0.1, 0.2, 0.5, 1, 2, 5, 10 μg m^{-3} from the 9 source regions).

Figure 9. Horizontal distribution of (left) dust layer loading (mg m^{-2}), (middle) dust layer contribution to column (fraction), and (right) ratio of DU_f (diameter <2.5 μm) to DU (i.e., all size range) for each layer. Numbers in panels are the global total values (left) and mean values (middle and right) of each layer.

Figure 10. Horizontal distribution of F_{src} (contribution of sources) of multi-model mean for each layer. NAF is the sum of WAF, EAF, and BOD; MDECAS is the sum of MDE and CAS; EASTAK is the sum of EAS and TAK. Numbers in panels are the contribution of sources to the global dust loading of each layer.

Figure 11. (Left) Global monthly dust emission, deposition, and column loading. (Right) Percent contributions of dust sources.

Figure 12. Mass percentage contributions from nine source regions to the dust load over three land receptor regions EAS, NAM, and AMZ estimated by 7 individual models and their mean values.

Figure 13. Mass percentage contributions from nine source regions to the dust load over two oceanic receptors (NATL, NPAC) and one polar region (ARC) estimated by 7 individual models and their mean values.

Figure 14. Global monthly dust column loading over the 14 receptor regions averaged for 2009-2012.

Figure 15. Global monthly dust total deposition over the 14 receptor regions averaged for 2009-2012.

Figure 16. Dust source contribution of multi model mean for dust loading over the 14 receptor regions.

Figure 17. Dust source contribution of multi model mean for dust deposition over the 14 receptor regions.

Figure 18. Percent contribution of dust sources to global dust loading from the previous studies and the present study. Estimates of the previous study are taken from Kok et al. (2021). Original source regions are regrouped to 5 larger regions.

Table 1. Description of the participating models.

	GFDL-AM4	CAM5-ATRAS	CESM2	GEOS	GEOS-Chem	GISS-OMA	SPRINTARS
Resolution (°lon×°lat)	288×180 (1.25×1)	144×96 (2.5×1.88)	288×192 (1.25×1.93)	720×361 (0.5×0.5)	144×91 (2.5×2)	144×90 (2.5×2)	640×320 (0.56×0.56)
Vertical Layers	33	30	32	72	47	40	40
Meteorology (Simulation Type)[2]	AM4 (Nudged)	CAM5 (Nudged)	CESM (Nudged)	MERRA2 (Replay)	GEOS (CTM)	ModelE (Nudged)	MIROC (Nudged)
Size distribution (μm in radius)	5 bins 0.1-1.0-1.8-3.0-6.0-10.0	12 bins 0.0005-0.001-0.003-0.079-0.196-0.039-0.078-0.156-0.313-0.625-1.25-2.5-5.0	3 modes[1] 0.005-0.05-0.5-5.0	5 bins 0.1-1.0-1.8-3.0-6.0-10.0	4 bins 0.1-1.0-1.8-3.0-6.0	8 bins 0.05-0.1-0.25-0.l5-1-2-4-8-16	6 bins 0.1-0.22-0.46-1.0-2.15-4.64-10.0
Dust emission scheme	Ginoux et. al. (2001)	Zender et al. (2003)	Zender et al. (2003)	Ginoux et. al. (2001)	Zender et al. (2003)	Miller et al. (2006)	Gillett (1978)
References	Zhao et al. (2018)	Matsui et al. (2014, 2017) Matsui and Mahowald (2017)	Liu et al. (2012, 2016)	Chin et al. (2002, 2009) Ginoux et al. (2001)	Bey et al. (2001)	Miller et al., (2006); Bauer and Koch (2005)	Takemura et al. (2000, 2005)

1. Size of CESM2 is the modal radius of each mode. CESM2 has four aerosol modes, but dust is only carried in three of them.

2. Nudged: meteorological field observations (e.g., q, T, p) are ingested to the model, Replay: the model is re-initialized every day, CTM (chemistry transport model): there is no interaction between meteorology and chemistry.

Table 2. Global mean dust quantities from the DUSA participating models averaged for 2009-2012. The three bottom rows are the mean, standard deviation, and diversity of 7 models. The underlined values are the maximum and minimum model values. Diversity is the ratio of standard deviation to mean and in percent. Lifetime is calculated by LOAD/Deposition×365 and in days.

	Emission (Tg yr^{-1})	Deposition (Tg yr^{-1})	LOAD (Tg)	DOD	Lifetime (days)
GFDL-AM4	1578	1595	14.6	0.022	3.3
CAM5-ATRAS	<u>4311</u>	<u>4531</u>	<u>34.2</u>	0.026	<u>2.8</u>
CESM2	2826	2929	31.6	<u>0.034</u>	<u>3.9</u>
GEOS	1417	1418	20.8	0.025	5.4
GEOS-Chem	<u>1130</u>	<u>1132</u>	<u>11.2</u>	<u>0.012</u>	<u>3.6</u>
GISS-OMA	1830	1830	26.0	0.026	5.2
SPRINTARS	2278	2084	11.6	0.017	2.0
Mean	2196	2217	21.4	0.023	3.5
Standard deviation	1091	1171	9.4	0.007	1.2
Diversity (%)	49.7	52.8	44.1	31.2	34.4

Table 3. Dust emission of SUM and various sources by models (Tg yr^{-1}). Percent contribution is given in parenthesis. Diversity is defined as the ratio of standard deviation to mean multiplied by 100. Source regions are West Africa (WAF), East Africa (EAF), Bodélé (BOD), Central Asia (CAS), Middle East (MDE), East Asia (EAS), Taklimakan desert (TAK), North America (NAM), and Southern Hemisphere (SOH).

Source Name	GFDL-AM4	CAM5-ATRAS	CESM2	GEOS	GEOS-Chem	GISS-OMA	SPRIN-TARS	Mean	STD	Diversity
SUM	1556	4253	2823	1416	1130	1830	2221	2175	1073	49.3
	(100.0)	(100.0)	(100.0)	(100.0)	(100.0)	(100.0)	(100.0)	(100.0)	(0)	(0)
WAF	382.7	1099.0	226.7	419.2	406.2	517.0	648.9	528.5	282.6	53.5
	(24.6)	(25.8)	(8.0)	(29.6)	(36.0)	(28.3)	(29.2)	(24.3)	(8.7)	(33.5)
EAF	239.3	891.9	637.8	262.6	213.2	275.0	376.3	413.7	255.9	61.9
	(15.4)	(21.0)	(22.6)	(18.5)	(18.9)	(15.0)	(16.9)	(19.0)	(2.8)	(15.3)
BOD	107.3	201.7	103.2	171.1	128.7	348.0	263.1	189.1	90.3	47.8
	(6.9)	(4.7)	(3.7)	(12.1)	(11.4)	(19.0)	(11.8)	(8.7)	(5.3)	(53.3)
MDE	218.1	927.2	179.8	273.3	180.8	284.0	148.7	316.0	274.1	86.7
	(14.0)	(21.8)	(6.4)	(19.3)	(16.0)	(15.5)	(6.7)	(14.5)	(5.9)	(41.2)
CAS	169.3	432.9	382.7	136.8	52.5	210.0	213.7	228.2	134.8	59.1
	(10.9)	(10.2)	(13.6)	(9.7)	(4.6)	(11.5)	(9.6)	(10.5)	(2.7)	(27.2)
EAS	101.4	276.7	134.2	45.6	79.8	39.3	125.2	114.6	80.2	70.0
	(6.5)	(6.5)	(4.8)	(3.2)	(7.1)	(2.1)	(5.6)	(5.3)	(1.8)	(36.1)
TAK	92.2	89.9	203.4	38.2	15.3	48.4	90.4	82.6	61.2	74.1
	(5.9)	(2.1)	(7.2)	(2.7)	(1.4)	(2.6)	(4.1)	(3.8)	(2.1)	(57.6)
NAM	32.3	45.7	8.9	6.0	3.0	2.9	81.6	25.8	29.6	115.0
	(2.1)	(1.1)	(0.3)	(0.4)	(0.3)	(0.2)	(3.7)	(1.2)	(1.3)	(114.3)
SOH	213.1	287.7	946.5	63.2	49.9	101.0	273.4	276.4	311.1	112.6
	(13.7)	(6.8)	(33.5)	(4.5)	(4.4)	(5.5)	(12.3)	(12.7)	(10.4)	(90.2)

Table 4. Multi-model mean and standard deviation of dust emission, column loading, deposition, and DOD from SUM and various sources. Units are Tg yr^{-1} for emission, load, and deposition, and dimensionless for DOD. Lifetime is calculated by LOAD/Deposition×365 and in days.

	Emission (Tg yr^{-1})	LOAD (Tg yr^{-1})	Deposition (Tg yr^{-1})	DOD (×10^3)	Lifetime (days)
SUM	2174.8±1118	21.1±9.8	2171.7±1199	22.9±7.6	3.5
WAF	528.5±292.1	5.9±2.9	521.2±283.2	3.2±1.4	4.1
EAF	413.7±261.1	4.5±2.9	402.8±252.3	2.9±2.8	4.1
BOD	189.1±99.3	2.1±1.5	189.6±96.4	1.1±0.6	4.0
MDE	316.0±278.2	3.2±2.2	312.0±277.5	1.7±1.1	3.7
CAS	228.2±154.0	1.8±1.2	228.9±160.9	1.5±1.7	2.9
EAS	114.6±87.3	0.6±0.3	118.7±98.8	0.5±0.4	1.8
TAK	82.6±66.3	0.6±0.5	86.3±71.4	0.5±0.7	2.5
NAM	25.8±30.0	0.1±0.1	30.6±31.8	0.1±0.1	1.2
SOH	276.4±314.2	2.2±3.0	281.6±319.8	2.0±3.6	2.9

Table 5. Global scale contribution of SUM and various sources for emission, column loading, deposition, and DOD in percentage. Numbers in the parenthesis are the model diversity, which is the ratio of standard deviation to mean. Unit is percent for both variables.

	Emission (%)	LOAD (%)	Deposition (%)	DOD (%)
SUM	100 (51.4)	100 (46.3)	100 (55.2)	100 (76.0)
WAF	24.3 (13.4)	28.1 (13.7)	24.0 (13.0)	23.5 (10.5)
EAF	19.0 (12.0)	21.5 (13.9)	18.5 (11.6)	22.0 (20.8)
BOD	8.7 (4.6)	10.0 (7.0)	8.7 (4.4)	8.4 (4.6)
MDE	14.5 (12.8)	15.1 (10.6)	14.4 (12.8)	12.9 (8.0)
CAS	10.5 (7.1)	8.8 (5.8)	10.5 (7.4)	11.0 (13)
EAS	5.3 (4.0)	2.9 (1.6)	5.5 (4.6)	3.4 (2.7)
TAK	3.8 (3.0)	2.7 (2.3)	4.0 (3.3)	3.7 (5.0)
NAM	1.2 (1.4)	0.6 (0.5)	1.4 (1.5)	0.6 (0.6)
SOH	12.7 (14.4)	10.4 (14.0)	13 (14.7)	14.6 (26.7)

Table 6. Contribution of sources to receptors over land from the multi-model mean. Top row is the annual mean loading (LOAD) of SUM and standard deviation over the receptor regions. Numbers in the parenthesis are the model diversity, which is the ratio of standard deviation to mean (%).

Source Region	NAM	EUR	IND	EAS	TNAF	AMZ	TBP
LOAD ($\times10^{-3}$ Tg yr^{-1})	84±71	208±82	419±252	418±171	2272±1146	155±144	72±57
SUM (%)	100 (84.6)	100 (39.6)	100 (60.1)	100 (41.0)	100 (50.5)	100 (92.5)	100 (78.6)
WAF (%)	31.7 (113.0)	53.0 (43.2)	4.5 (69.5)	4.7 (93.7)	13.3 (56.3)	34.8 (88.0)	6.8 (87.1)
EAF (%)	11.2 (110.3)	23.5 (41.6)	6.0 (46.3)	3.4 (56.5)	46.0 (97.9)	15.0 (91.3)	6.0 (50.9)
BOD (%)	6.3 (162.1)	5.2 (93.1)	2.7 (98.8)	1.9 (94.5)	25.9 (74.3)	16.7 (138.9)	3.3 (101.7)
MDE (%)	8.3 (113.3)	4.2 (75.1)	33.6 (74.5)	5.2 (77.3)	12.2 (60.5)	11.5 (204.8)	12.6 (67.3)
CAS (%)	6.4 (128.3)	10.8 (79.9)	50.2 (68.5)	6.6 (68.1)	1.1 (48.5)	3.0 (157.1)	16.2 (66.3)
EAS (%)	5.0 (79.0)	1.1 (79.0)	0.9 (172.9)	65.3 (66.6)	0.4 (117.6)	1.0 (91.7)	14.9 (146.2)
TAK (%)	6.1 (85.5)	1.2 (71.1)	0.9 (117.7)	11.7 (73.4)	0.4 (109.5)	0.9 (90.7)	38.7 (107.5)
NAM (%)	24.3 (46.9)	0.7 (85.4)	0.5 (129.0)	0.6 (108.6)	0.4 (127.9)	0.6 (120.6)	0.7 (125.3)
SOH (%)	0.6 (83.3)	0.5 (105.7)	0.6 (146.5)	0.7 (100.5)	0.4 (95.2)	16.7 (93.5)	0.7 (125.7)

Table 7. Same as Table 6 except for ocean and the polar regions.

Source Region	NPAC	SPAC	NATL	SALT	INDO	ARC	AARC
LOAD ($\times10^{-3}$ Tg yr^{-1})	545±424	331±248	2593±1159	594±627	1730±987	75±57	14±13
SUM (%)	100 (77.9)	100 (74.8)	100 (44.7)	100 (105.7)	100 (57.1)	100 (75.8)	100 (94.9)
WAF (%)	20.9 (118.0)	4.6 (111.6)	69.2 (49.9)	3.7 (83.3)	3.5 (74.2)	22.9 (89.1)	4.8 (164.3)
EAF (%)	11.0 (92.8)	3.3 (75.5)	12.7 (52.4)	12.1 (85.9)	8.5 (68.3)	12.7 (82.9)	5.6 (161.8)
BOD (%)	7.6 (155.7)	2.8 (112.6)	12.7 (106.5)	8.4 (125.0)	2.4 (120.7)	6.0 (113.0)	4.4 (170.7)
MDE (%)	14.2 (99.5)	4.1 (100.3)	2.1 (92.6)	3.2 (82.3)	44.9 (70.3)	11.9 (99.9)	5.0 (174.4)
CAS (%)	11.0 (94.1)	1.8 (73.8)	0.9 (73.9)	0.8 (50.5)	11.8 (54.0)	23.7 (75.4)	4.2 (164.9)
EAS (%)	19.8 (32.7)	0.9 (90.2)	0.5 (67.9)	0.5 (71.9)	0.4 (69.3)	11.0 (62.4)	2.8 (217.0)
TAK (%)	11.8 (74.3)	0.8 (74.8)	0.7 (67.3)	0.6 (72.0)	0.5 (62.6)	9.0 (90.9)	3.5 (181.2)
NAM (%)	1.7 (69.4)	0.9 (95.5)	0.7 (82.8)	0.5 (73.7)	0.4 (81.5)	1.6 (103.8)	2.7 (225.5)
SOH (%)	2.0 (74.0)	80.7 (89.4)	0.6 (88.0)	70.2 (141.9)	27.7 (154.2)	1.0 (137.0)	67.0 (91.6)

Figure.

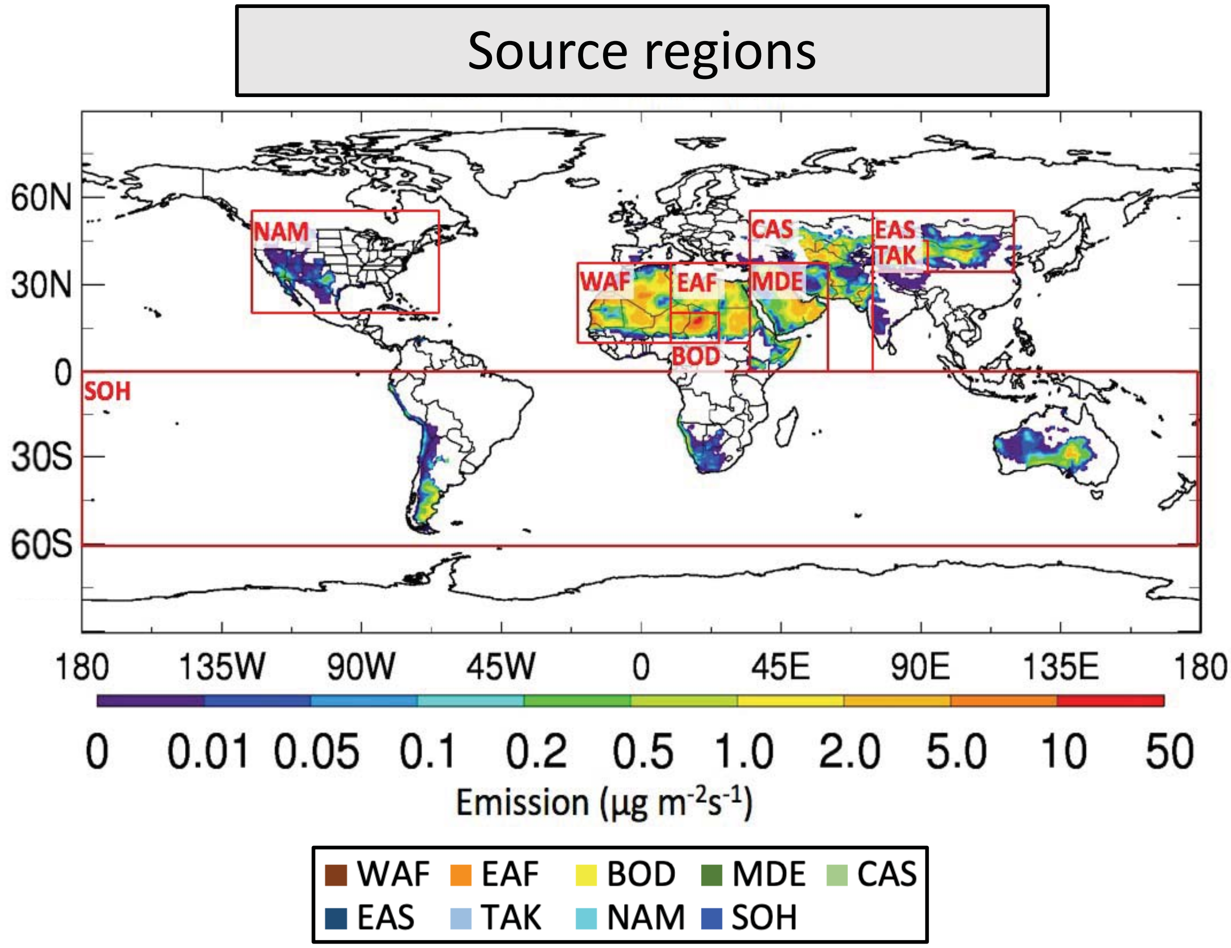

Figure 1. Map of dust sources for model simulation and analysis. The color shade is the annual mean dust emission of the GEOS model for 2009~2012. Source regions are color coded as shown below the map. Source regions are West Africa (WAF), East Africa (EAF), Bodélé (BOD), Central Asia (CAS), Middle East (MDE), East Asia (EAS), Taklimakan desert (TAK), North America (NAM), and Southern Hemisphere (SOH).

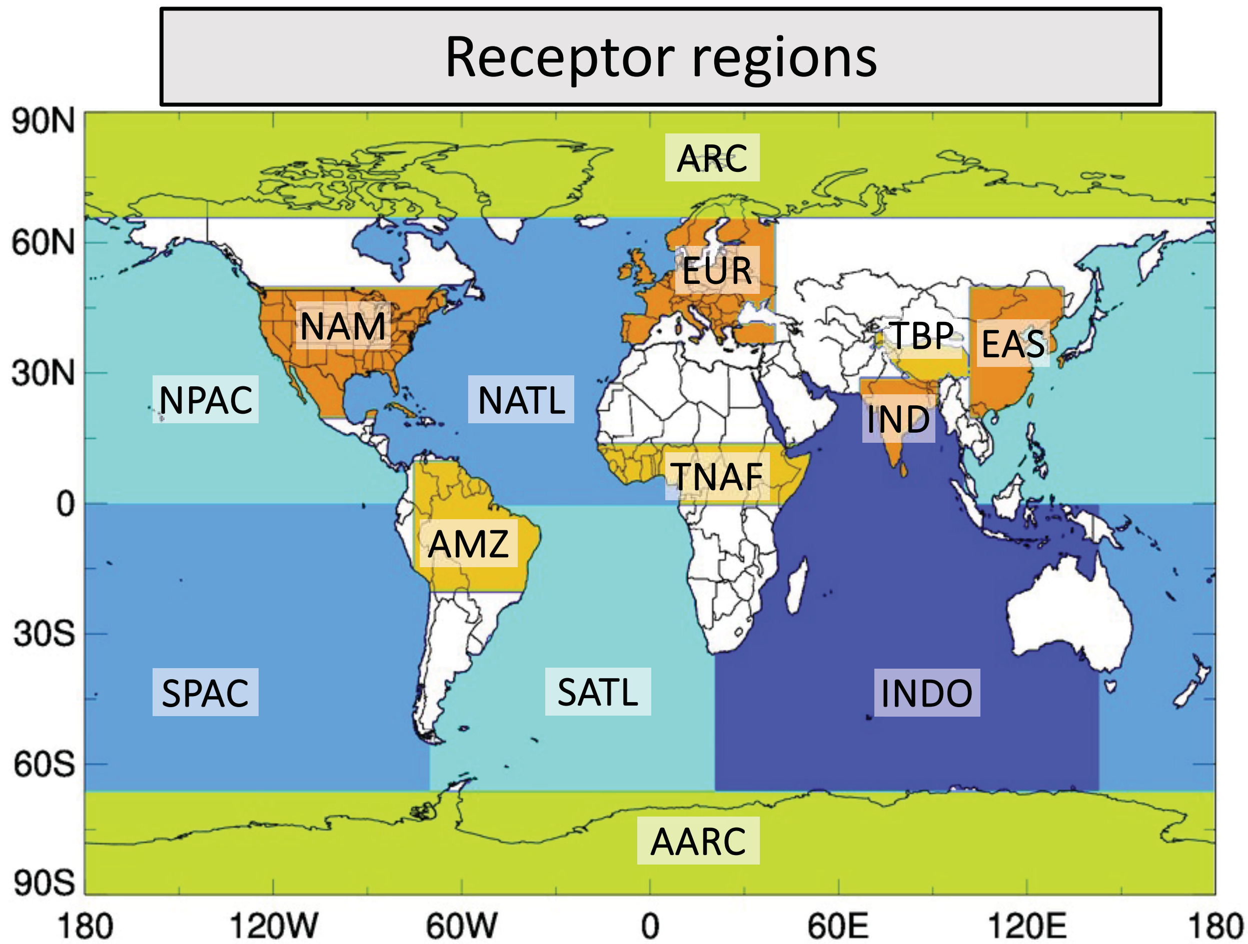

Figure 2. Map of dust receptors. Seven receptors are located over land and the remaining receptors cover ocean or polar regions. The receptor names are North America (NAM), Europe (EUR), India (IND), East Asia (EAS), Tropical North Africa (TNAF), Amazon (TMZ), Tibetan Plateau (TBP), North Atlantic (NATL), South Atlantic (SATL), North Pacific (NPAC), South Pacific (SPAC), Indian Ocean (INDO), Arctic (ARC), and Antarctic (AARC).

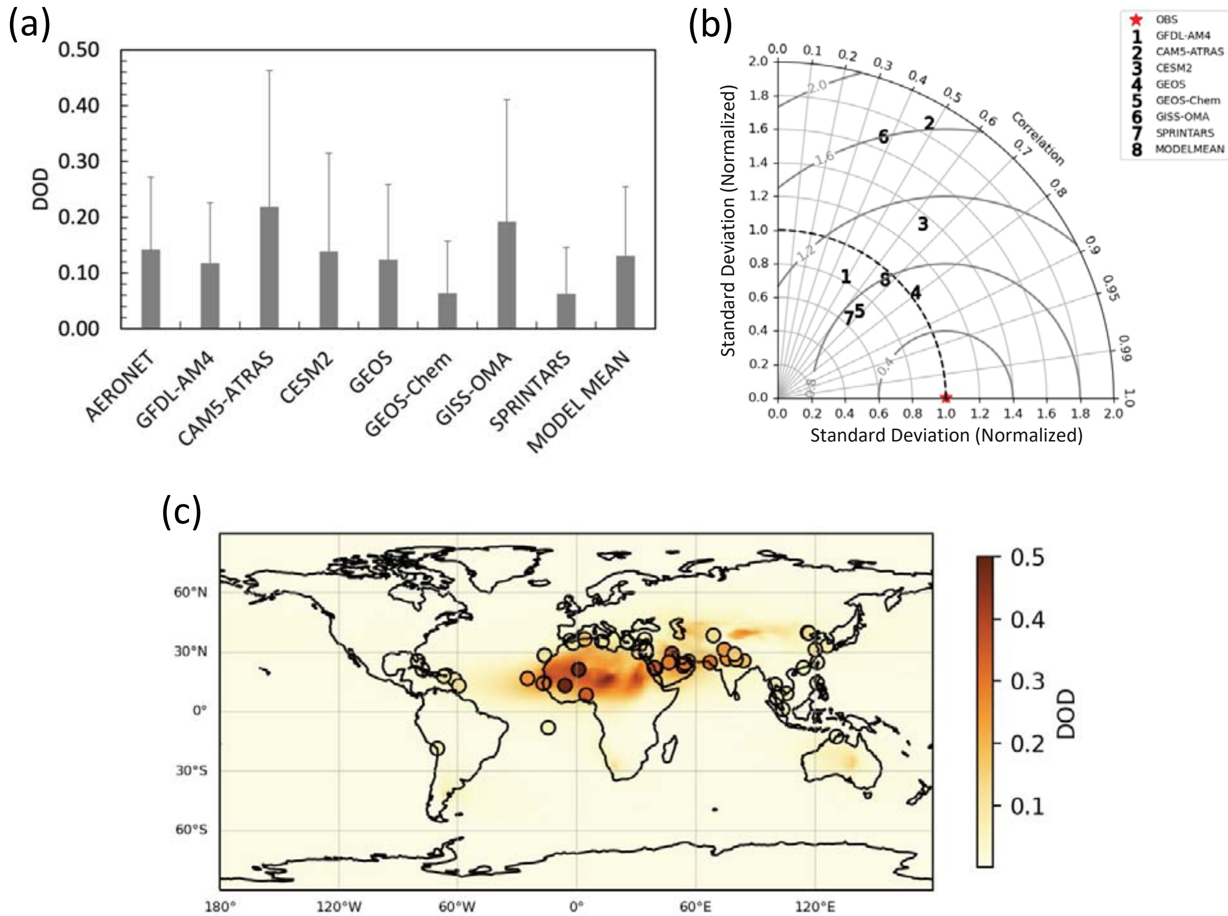

Figure 3. Comparisons of dust optical depths at 550 nm between AERONET and model averaged for 2009 and 2012. (a) Mean and standard deviation of AERONET and model, and (b) Taylor diagram of DOD from the AERONET and the models. (c) Map of multi-model mean DOD. AERONET DOD is overplotted in circle.

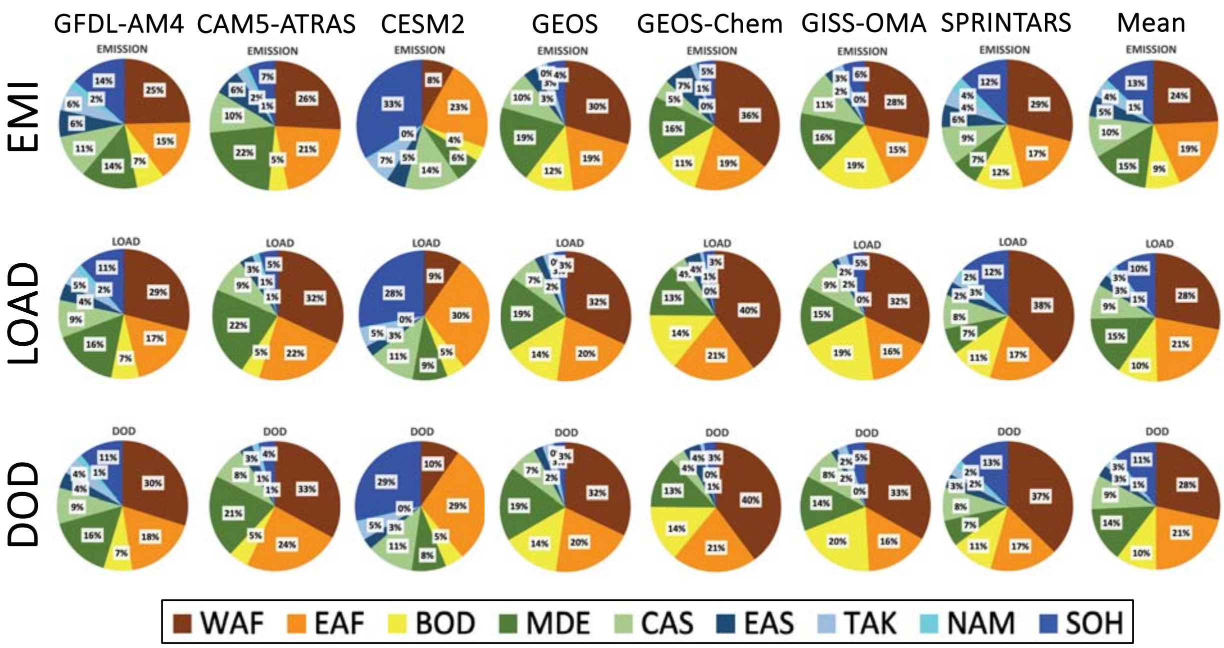

Figure 4. Percent contributions by mass of dust sources in global dust emission (EMI), column loading (LOAD), and dust optical depth (DOD).

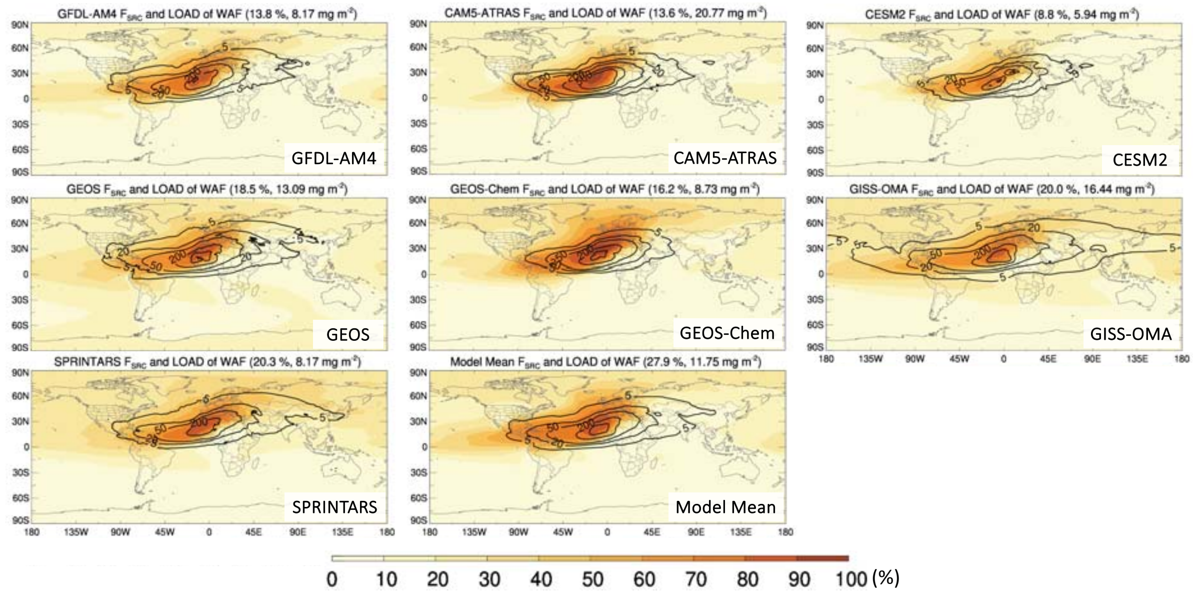

Figure 5. Horizontal distribution of $\bar{A}_{\ddot{A}\bar{A}}$(contribution of WAF; brown shade) and dust column loading (LOAD) (black contour lines at 5, 20, 50, 200, 500 mg m^{-2}) for WAF. Numbers in parenthesis are the area-weighted global mean of $\bar{A}_{\ddot{A}\bar{A}}$(left) and LOAD (right).

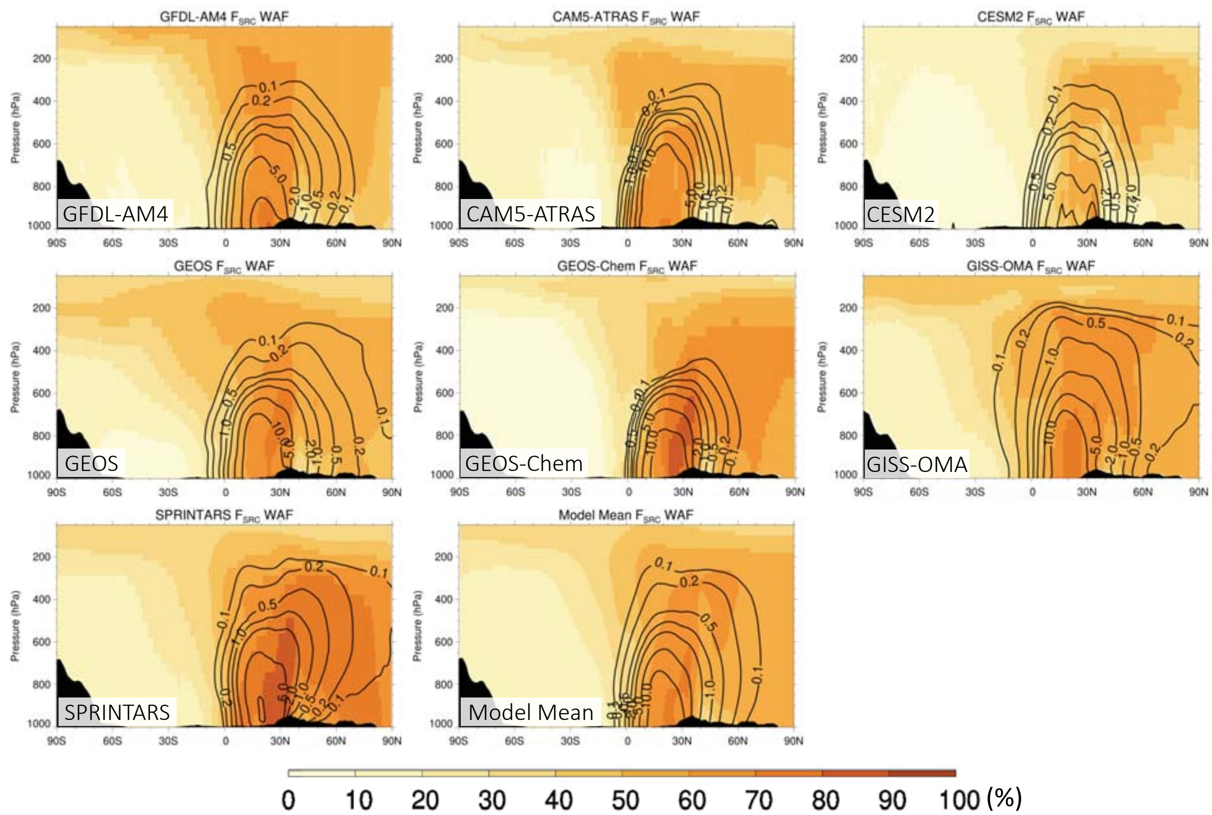

Figure 6. Vertical distribution of Ā ÄĀ(contribution of WAF; brown shade) and dust concentration (black contour lines at 0.1, 0.2, 0.5, 1, 2, 5, 10 μg m^{-3}) for WAF.

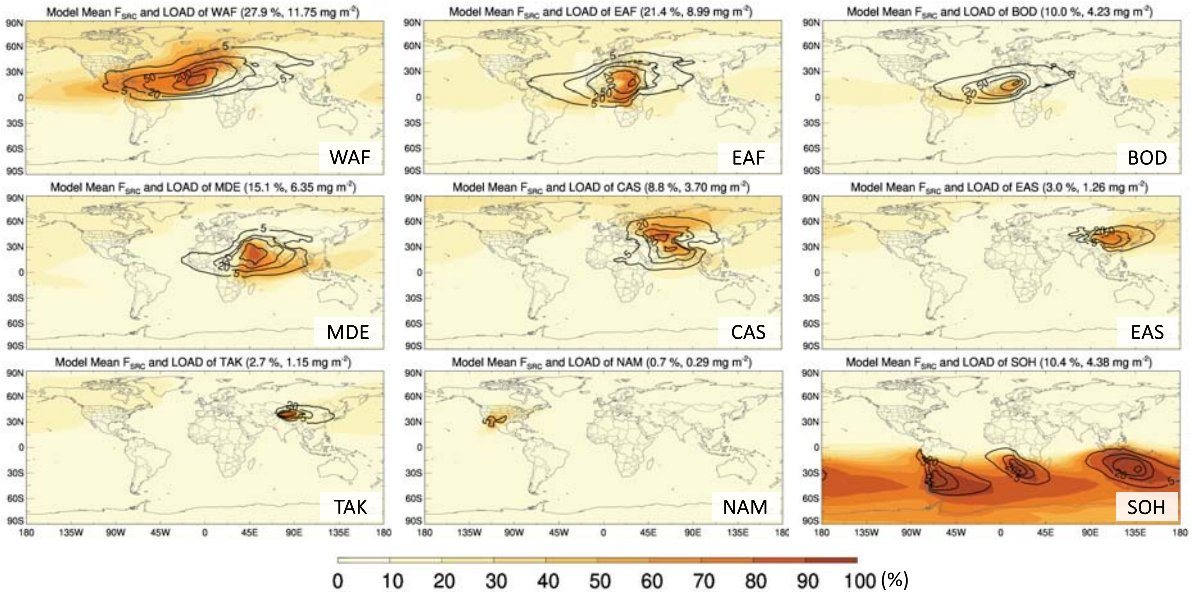

Figure 7. Horizontal distribution of multi-model mean Ā ÄĀ(contribution of sources; brown shade) and column dust loading (black contour lines at 5, 20, 50, 200, 500 mg m^{-2}). Numbers in parenthesis are the area-weighted global mean of Ā ÄĀ(left) and LOAD (right).

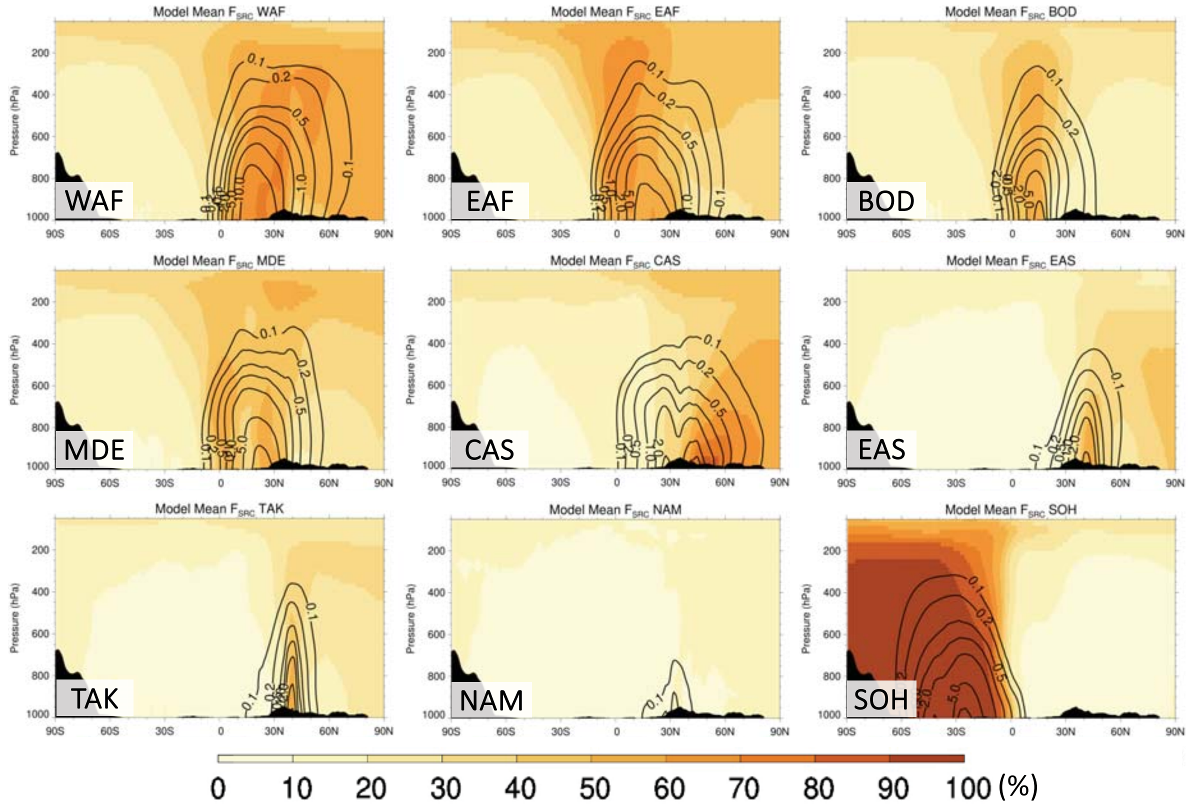

Figure 8. Vertical distribution of multi-model mean $\bar{A}\ \ddot{A}\bar{A}$(contribution of sources; brown shade) and dust concentration (black contour lines at 0.1, 0.2, 0.5, 1, 2, 5, 10 μg m^{-3} from the 9 source regions).

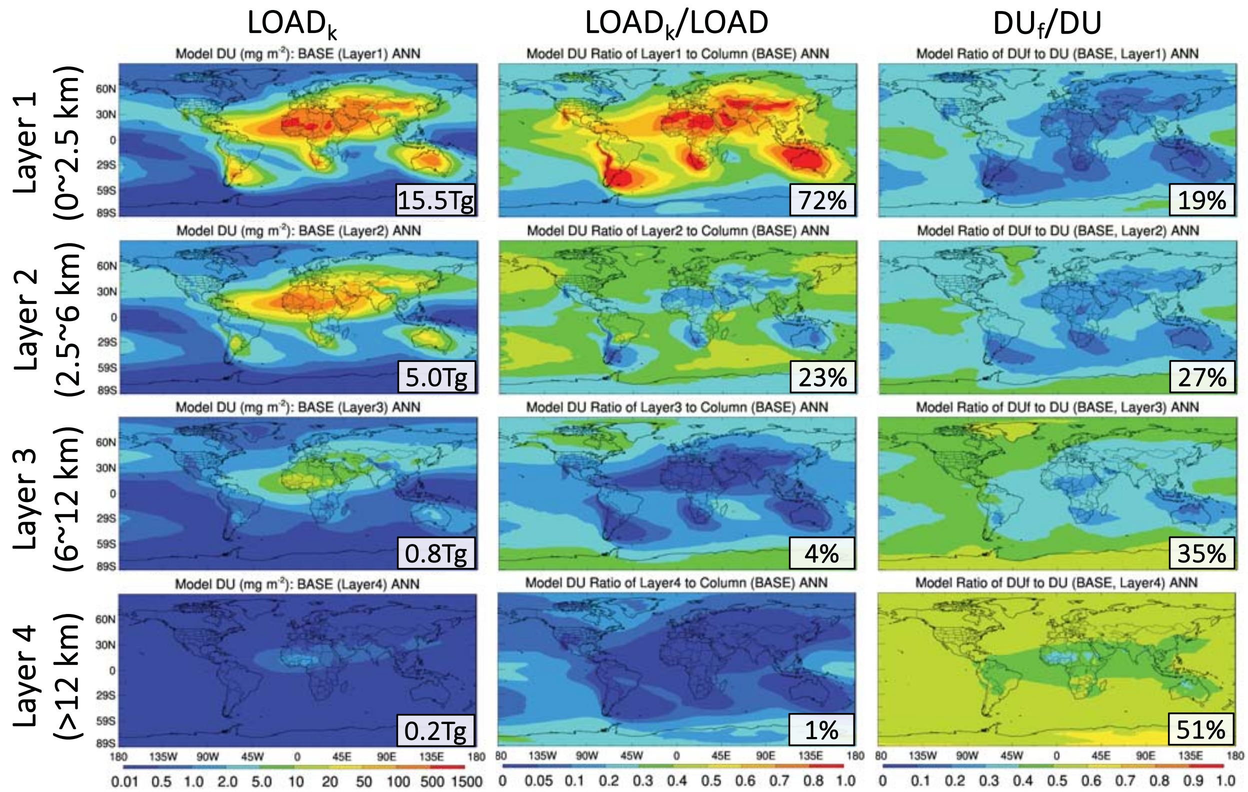

Figure 9. Horizontal distribution of (left) dust layer loading (mg m^{-2}), (middle) dust layer contribution to column (fraction), and (right) ratio of DU_f (diameter <2.5 μm) to DU (i.e., all size range) for each layer. Numbers in panels are the global total values (left) and mean values (middle and right) of each layer.

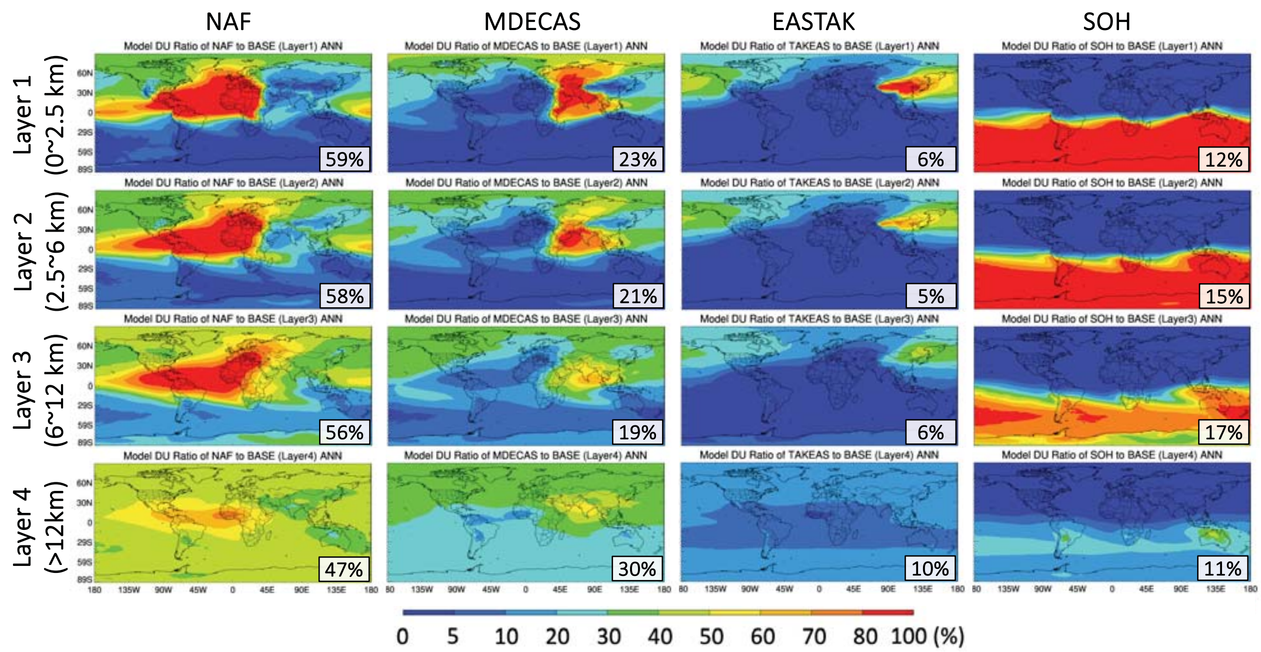

Figure 10. Horizontal distribution of Ā ÄĀ(contribution of sources) of multi-model mean for each layer. NAF is the sum of WAF, EAF, and BOD; MDECAS is the sum of MDE and CAS; EASTAK is the sum of EAS and TAK. Numbers in panels are the contribution of sources to the global dust loading of each layer.

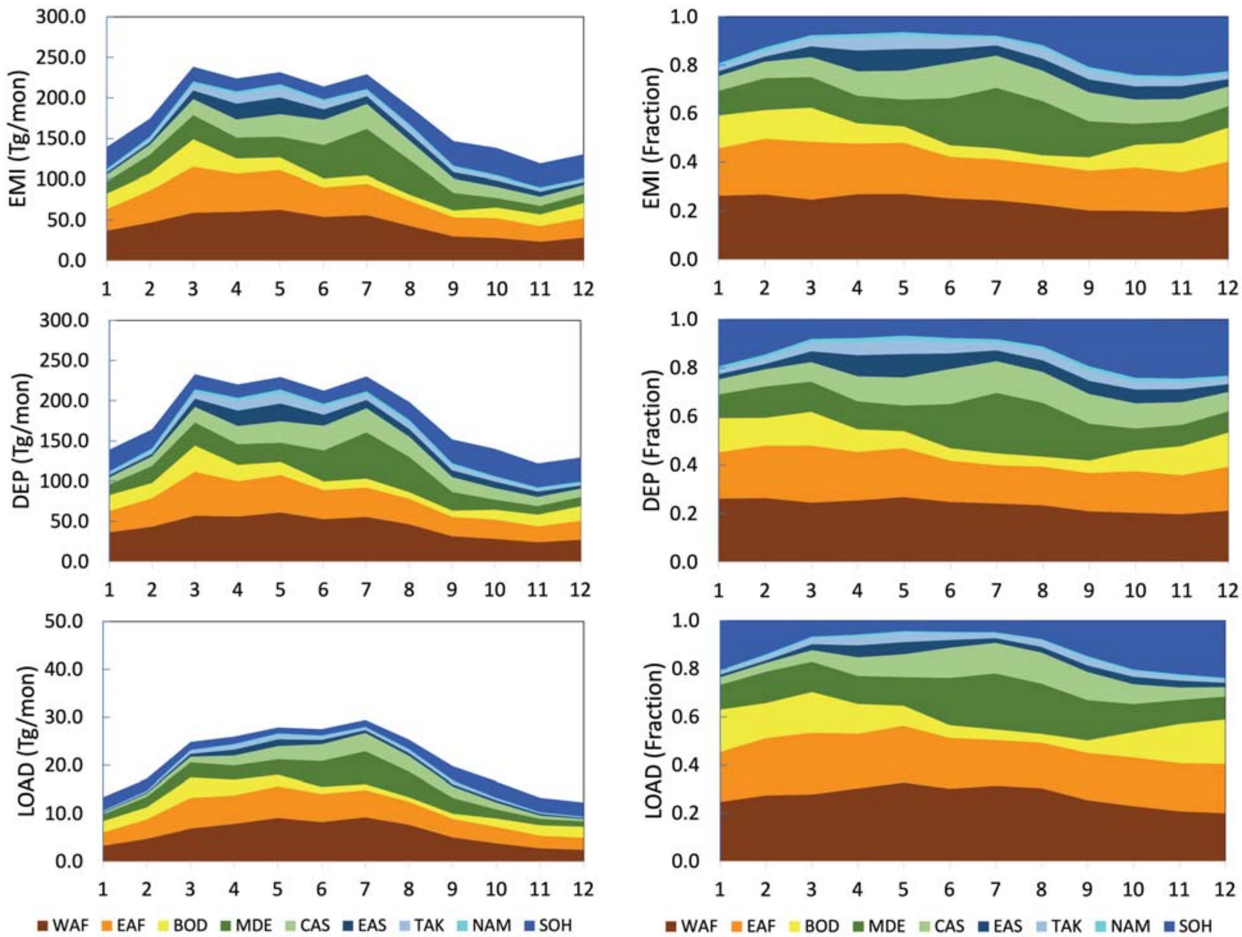

Figure 11. (Left) Global monthly dust emission, deposition, and column loading. (Right) Percent contributions of dust sources.

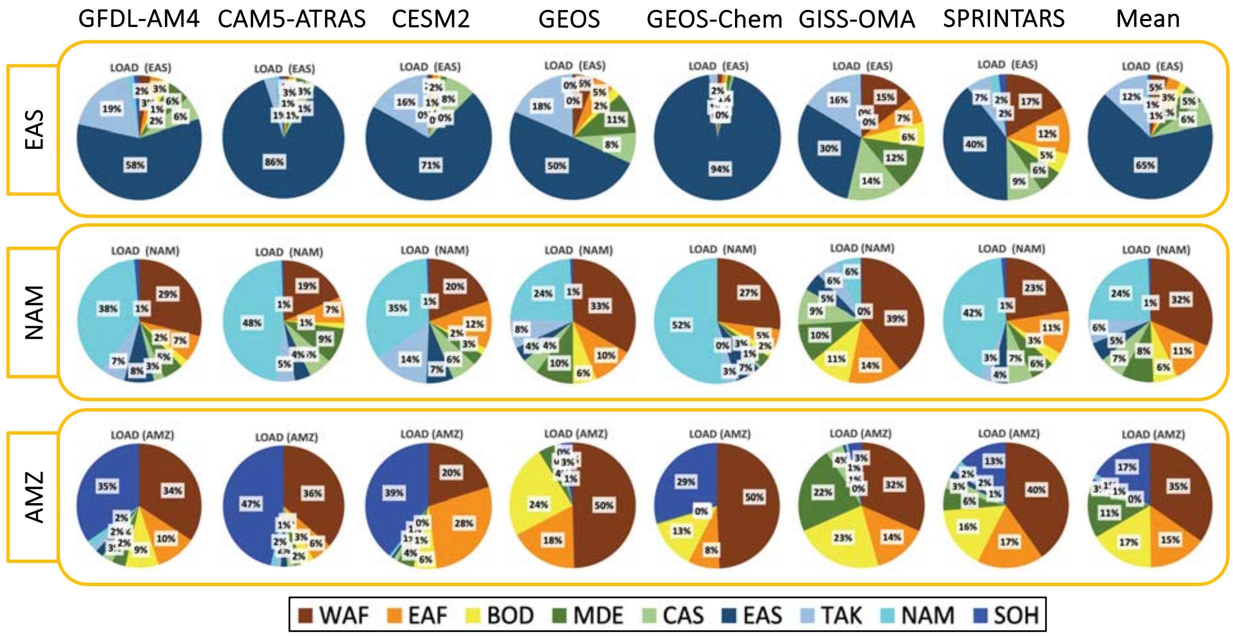

Figure 12. Mass percentage contributions from nine source regions to the dust load over three land receptor regions EAS, NAM, and AMZ estimated by 7 individual models and their mean values.

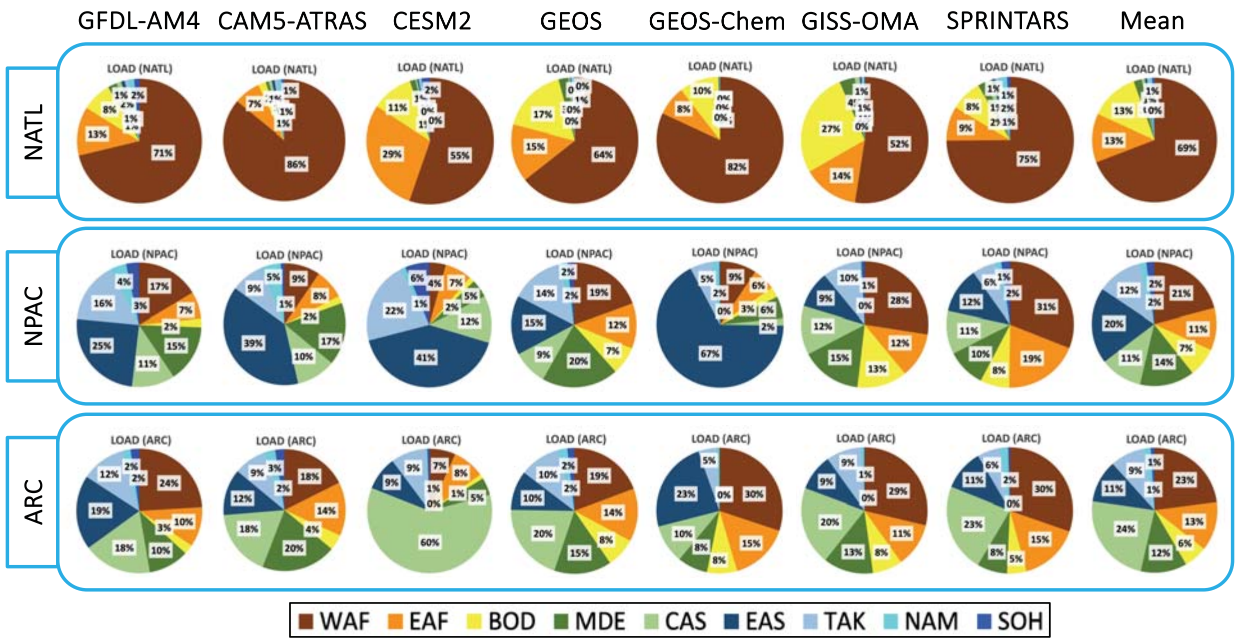

Figure 13. Mass percentage contributions from nine source regions to the dust load over two oceanic receptors (NATL, NPAC) and one polar region (ARC) estimated by 7 individual models and their mean values.

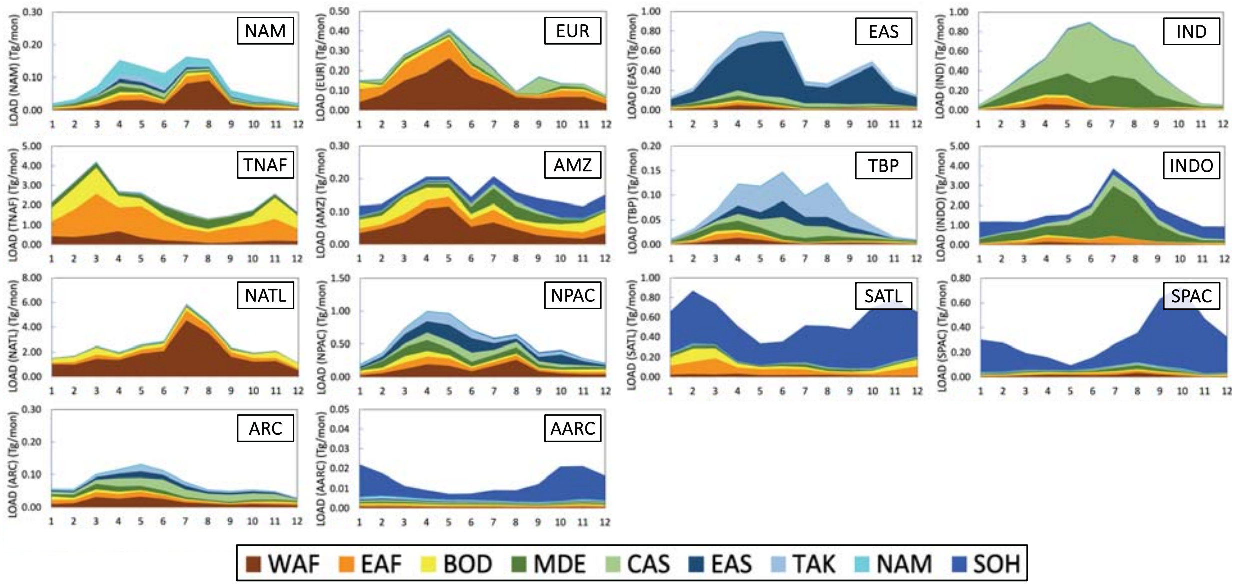

Figure 14. Global monthly dust column loading over the 14 receptor regions averaged for 2009-2012.

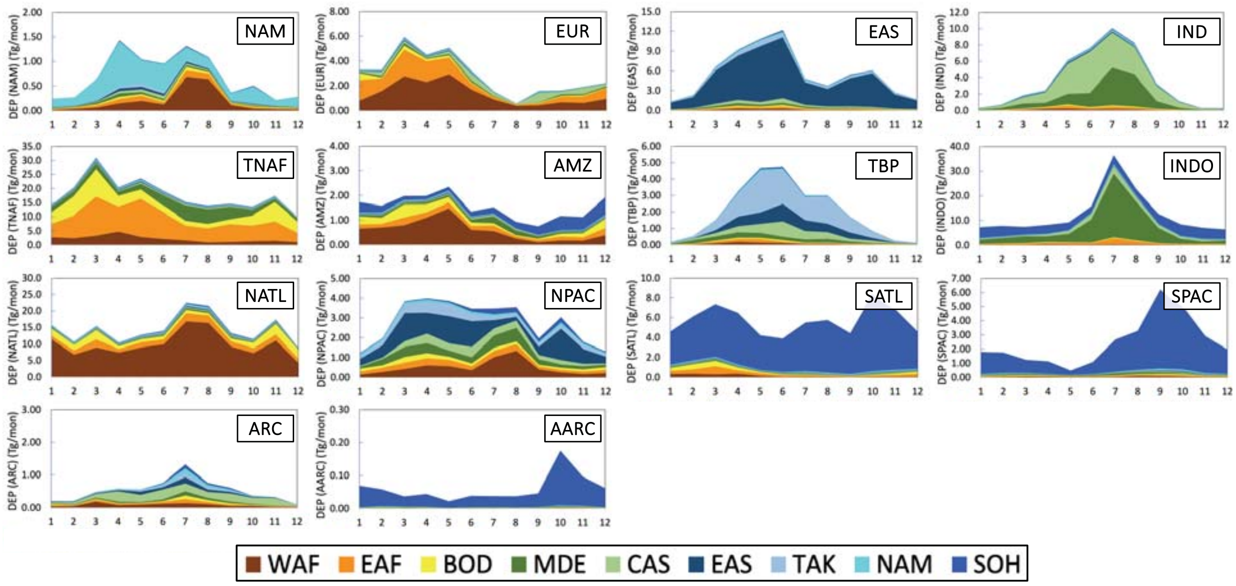

Figure 15. Global monthly dust total deposition over the 14 receptor regions averaged for 2009-2012.

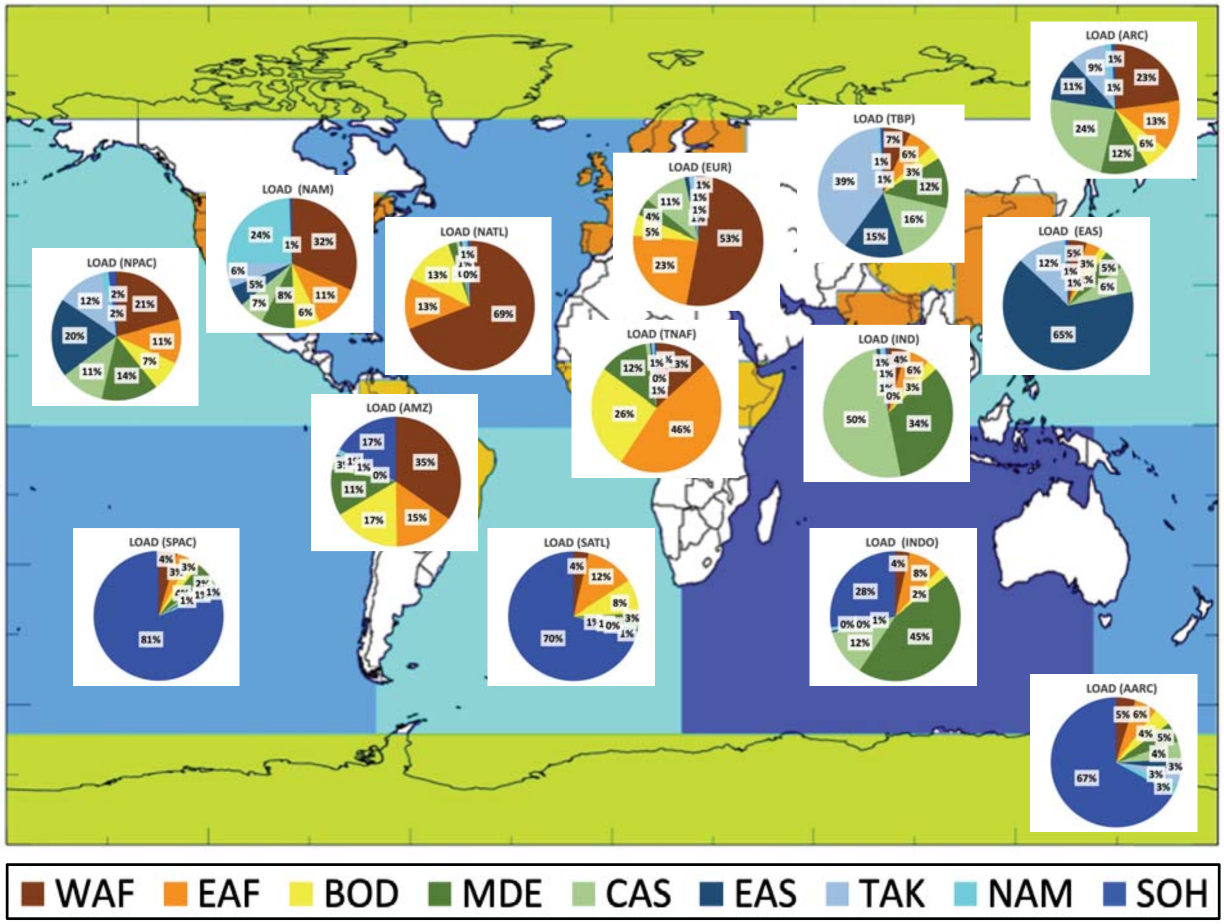

Figure 16. Dust source contribution of multi model mean for dust loading over the 14 receptor regions.

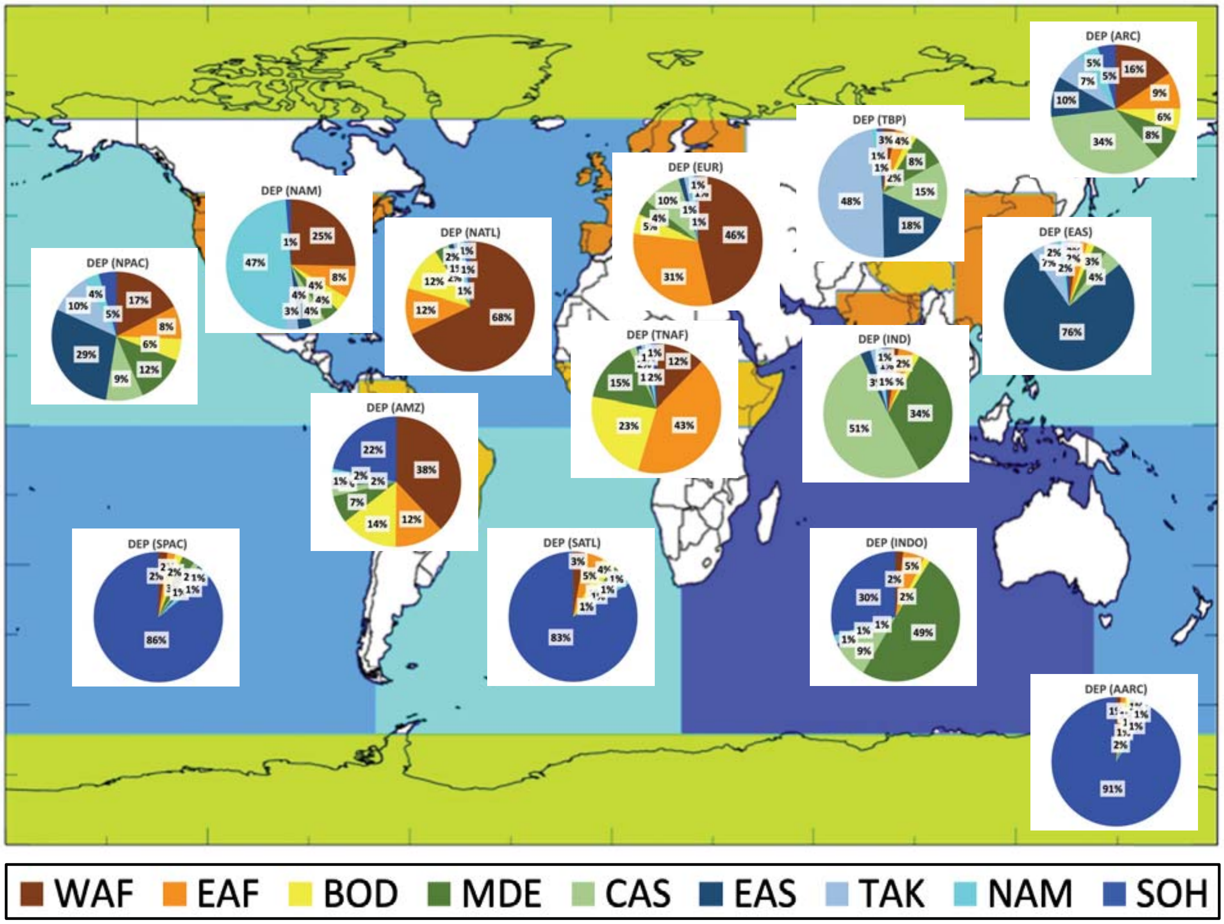

Figure 17. Dust source contribution of multi model mean for dust deposition over the 14 receptor regions.

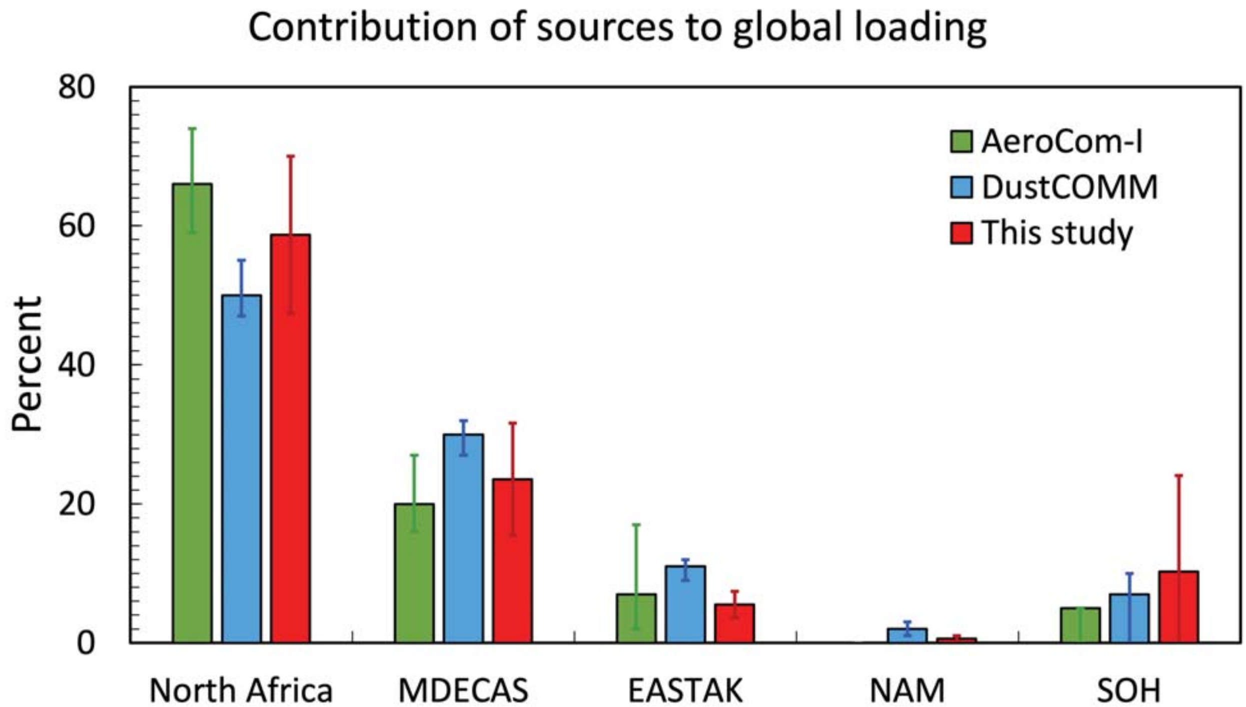

Figure 18. Percent contribution of dust sources to global dust loading from the previous studies and the present study. Estimates of the previous study are taken from Kok et al. (2021). Original source regions are regrouped to 5 larger regions.

Figure 1.

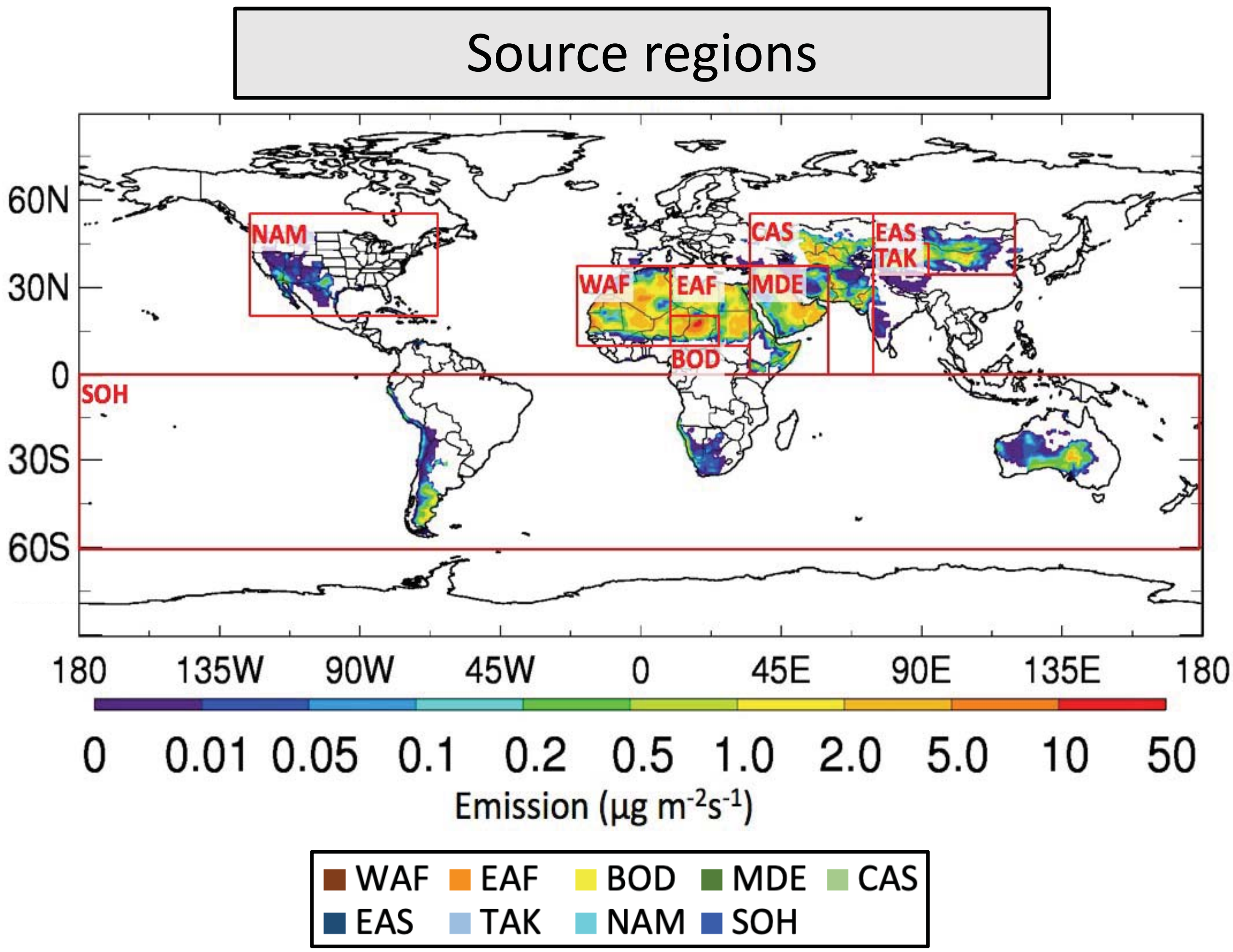
Source regions
NAM
WAF
EAF
BOD
CAS
MDE
EAS
TAK
SOH
60N
30N
0
30S
60S
180
135W
90W
45W
0
45E
90E
135E
180
0
0.01
0.05
0.1
0.2
0.5
1.0
2.0
5.0
10
50
Emission (μg m-2s-1)
WAF EAF BOD MDE CAS
EAS TAK NAM SOH

Figure 2.

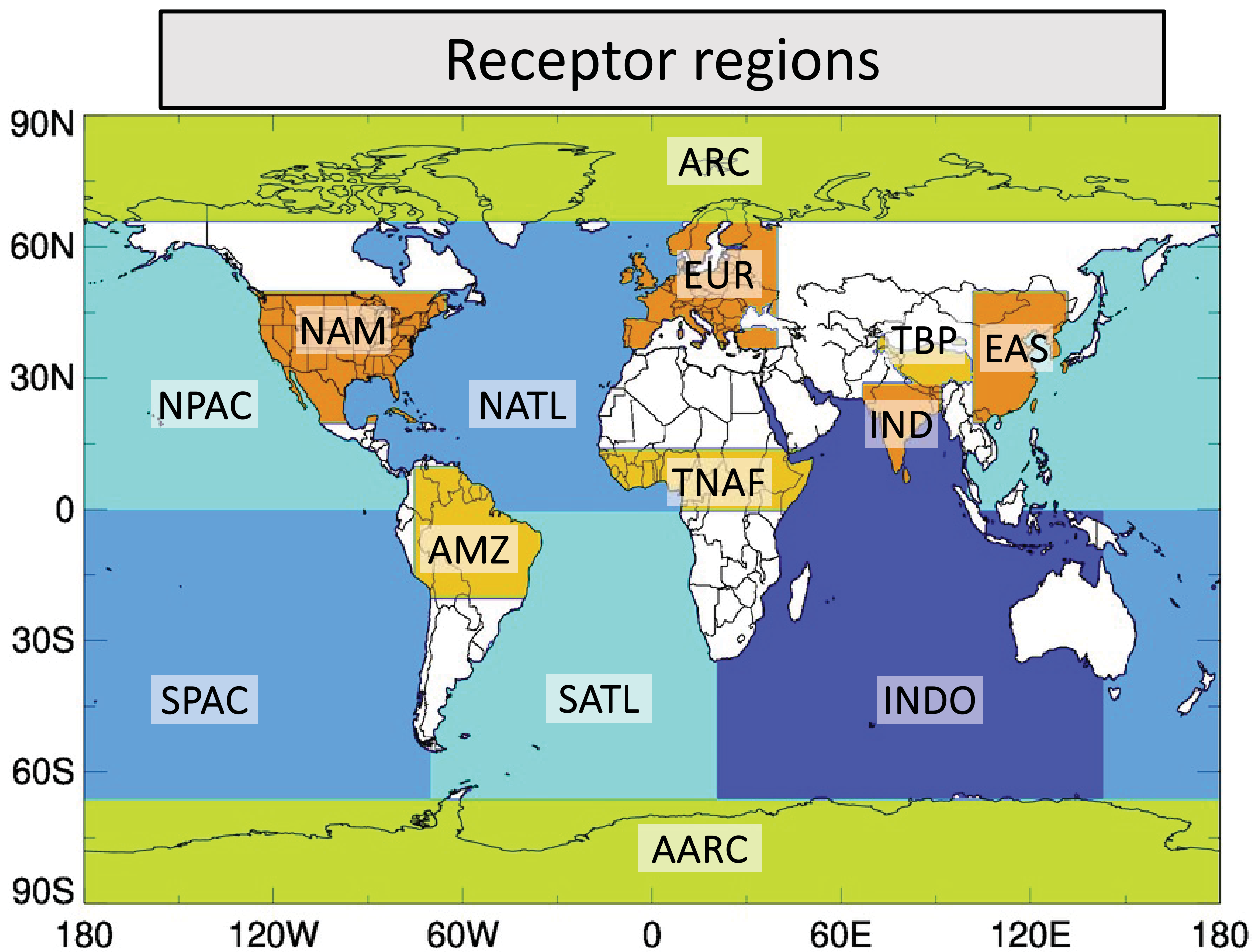
Receptor regions
90N
60N
30N
0
30S
60S
90S
180
120W
60W
0
60E
120E
180
ARC
EUR
NAM
TBP
EAS
NPAC
NATL
IND
TNAF
AMZ
SPAC
SATL
INDO
AARC

Figure 3.

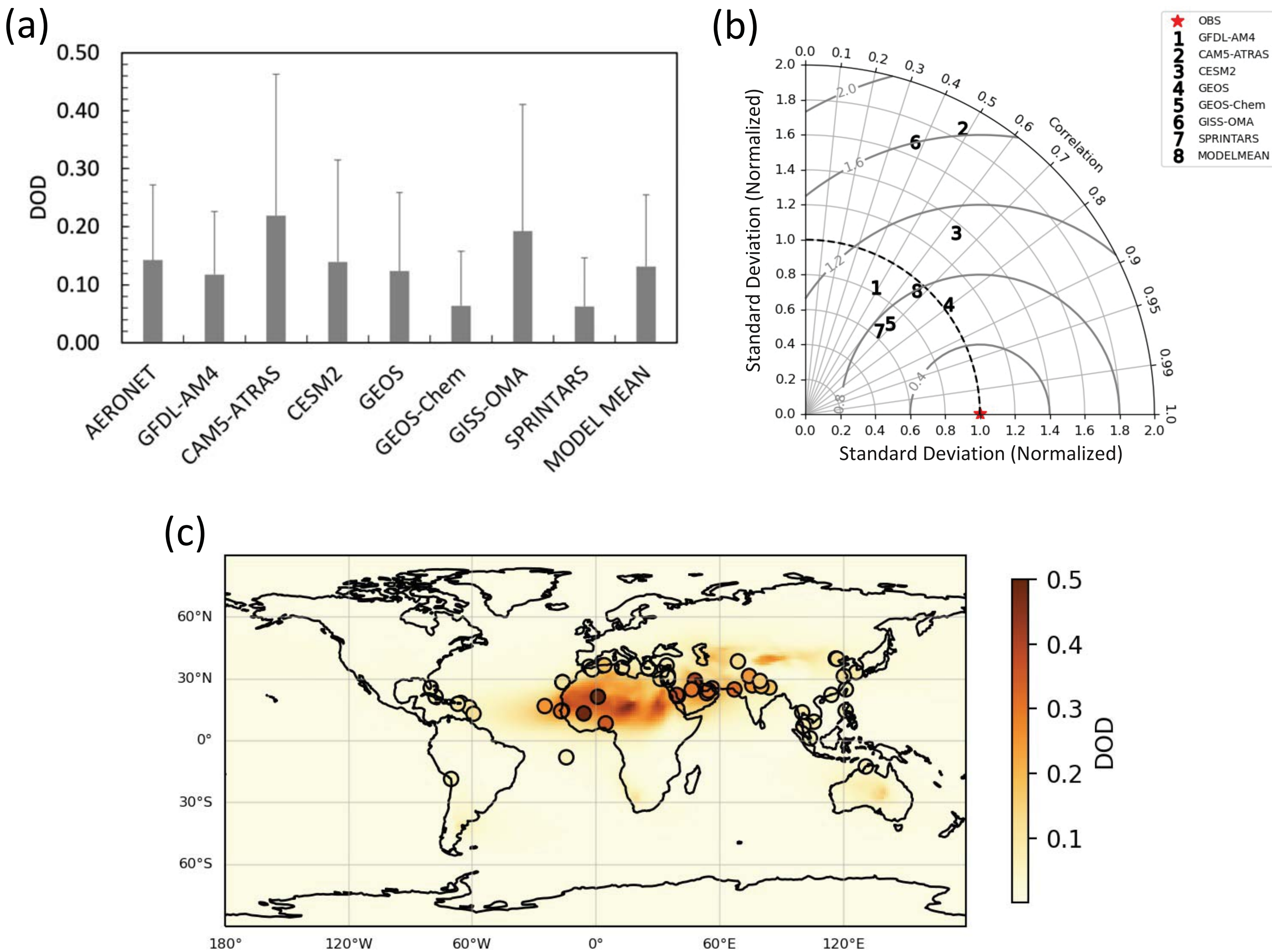

(a)
DOD
0.50
0.40
0.30
0.20
0.10
0.00
AERONET
GFDL-AM4
CAM5-ATRAS
CESM2
GEOS
GEOS-Chem
GISS-OMA
SPRINTARS
MODEL MEAN
(b)
Standard Deviation (Normalized)
Correlation
OBS
1 GFDL-AM4
2 CAM5-ATRAS
3 CESM2
4 GEOS
5 GEOS-Chem
6 GISS-OMA
7 SPRINTARS
8 MODELMEAN
(c)
60°N
30°N
0°
30°S
60°S
180°
120°W
60°W
0°
60°E
120°E
DOD
0.5
0.4
0.3
0.2
0.1

Figure 4.

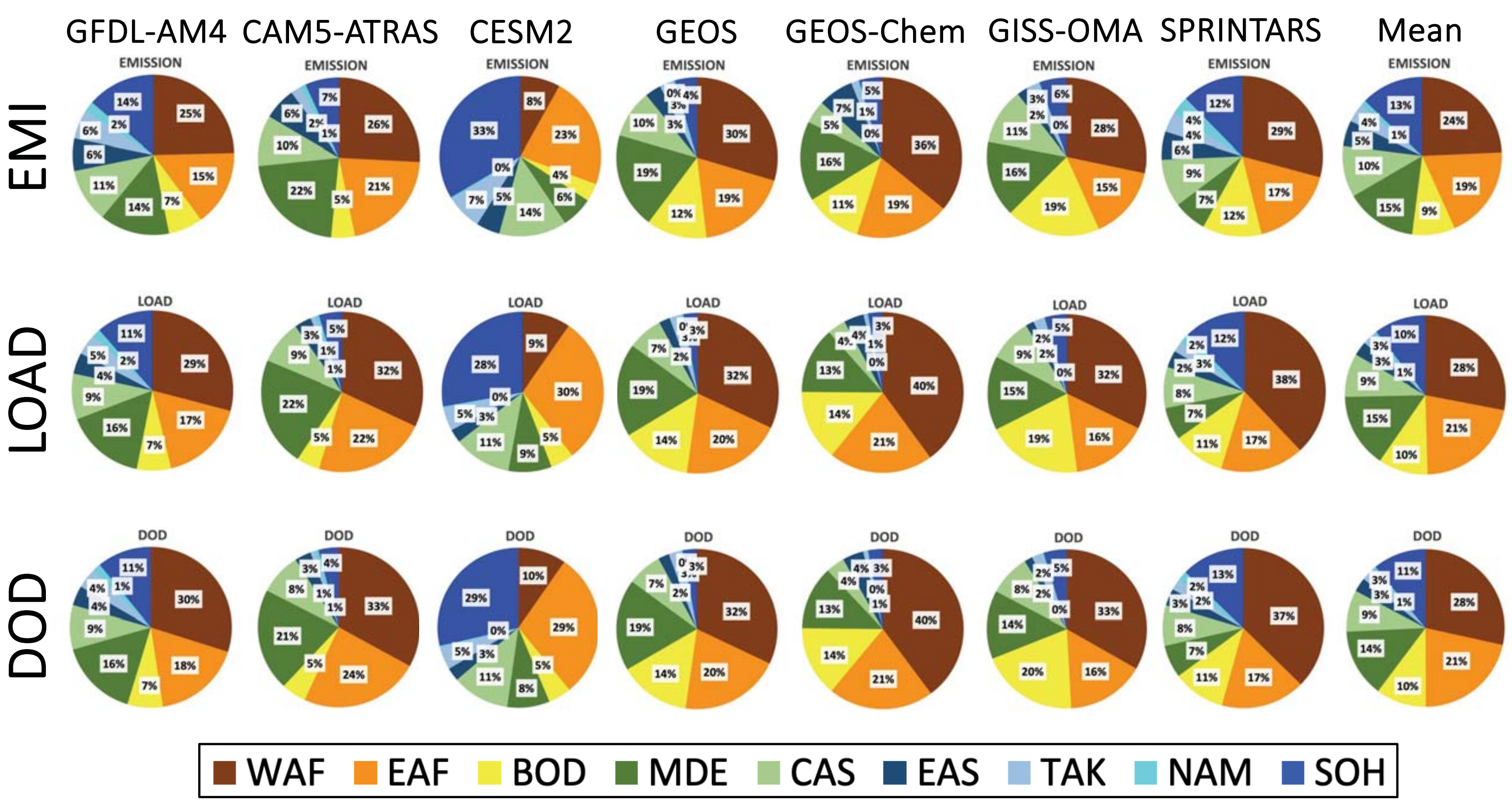
GFDL-AM4
CAM5-ATRAS
CESM2
GEOS
GEOS-Chem
GISS-OMA
SPRINTARS
Mean
EMI
LOAD
DOD
EMISSION
LOAD
DOD
WAF
EAF
BOD
MDE
CAS
EAS
TAK
NAM
SOH

Figure 5.

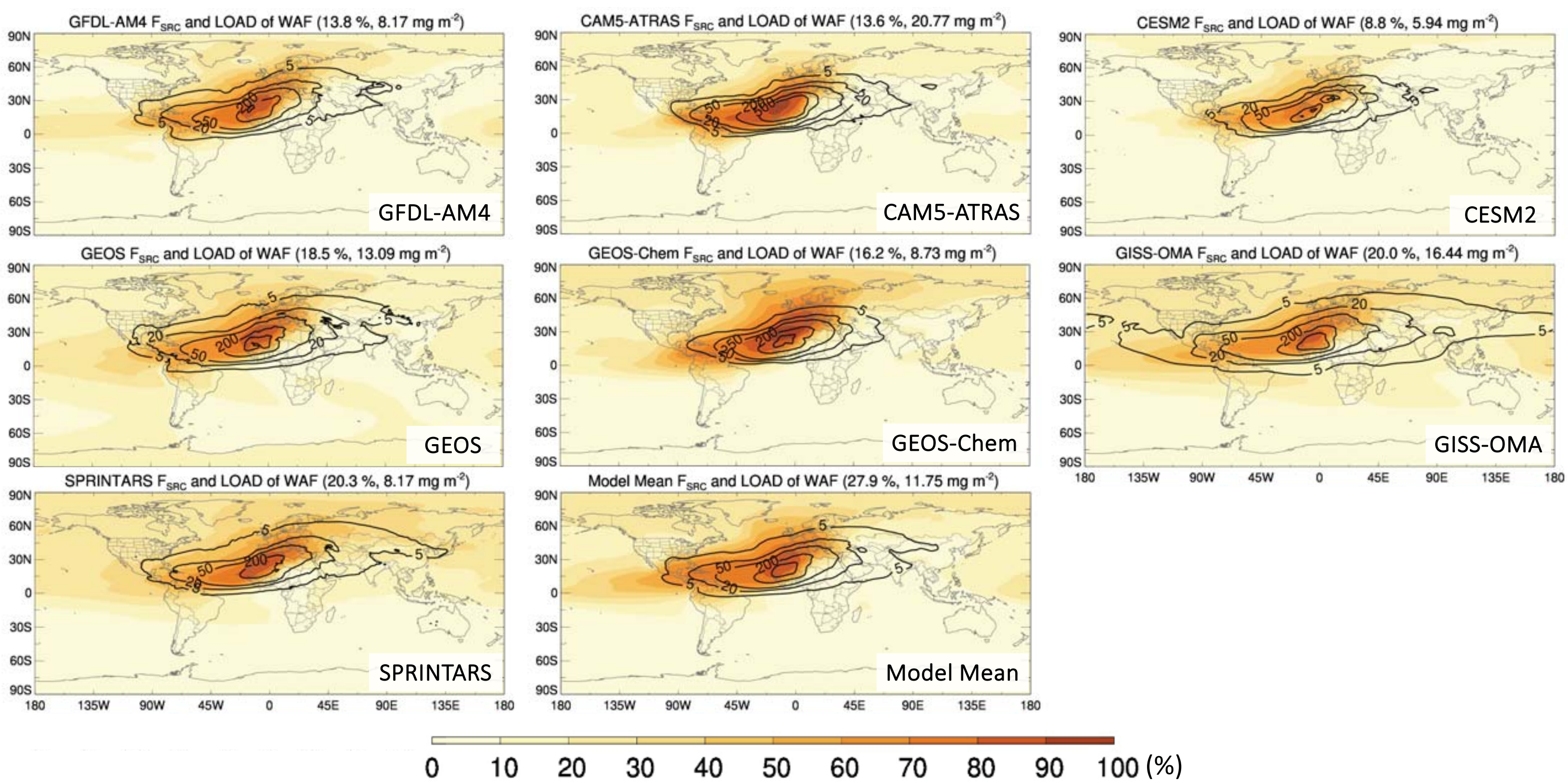

GFDL-AM4 F_{SRC} and LOAD of WAF (13.8 %, 8.17 mg m^{-2})
GFDL-AM4
CAM5-ATRAS F_{SRC} and LOAD of WAF (13.6 %, 20.77 mg m^{-2})
CAM5-ATRAS
CESM2 F_{SRC} and LOAD of WAF (8.8 %, 5.94 mg m^{-2})
CESM2
GEOS F_{SRC} and LOAD of WAF (18.5 %, 13.09 mg m^{-2})
GEOS
GEOS-Chem F_{SRC} and LOAD of WAF (16.2 %, 8.73 mg m^{-2})
GEOS-Chem
GISS-OMA F_{SRC} and LOAD of WAF (20.0 %, 16.44 mg m^{-2})
GISS-OMA
SPRINTARS F_{SRC} and LOAD of WAF (20.3 %, 8.17 mg m^{-2})
SPRINTARS
Model Mean F_{SRC} and LOAD of WAF (27.9 %, 11.75 mg m^{-2})
Model Mean
90N 60N 30N 0 30S 60S 90S
180 135W 90W 45W 0 45E 90E 135E 180
0 10 20 30 40 50 60 70 80 90 100 (%)

Figure 6.

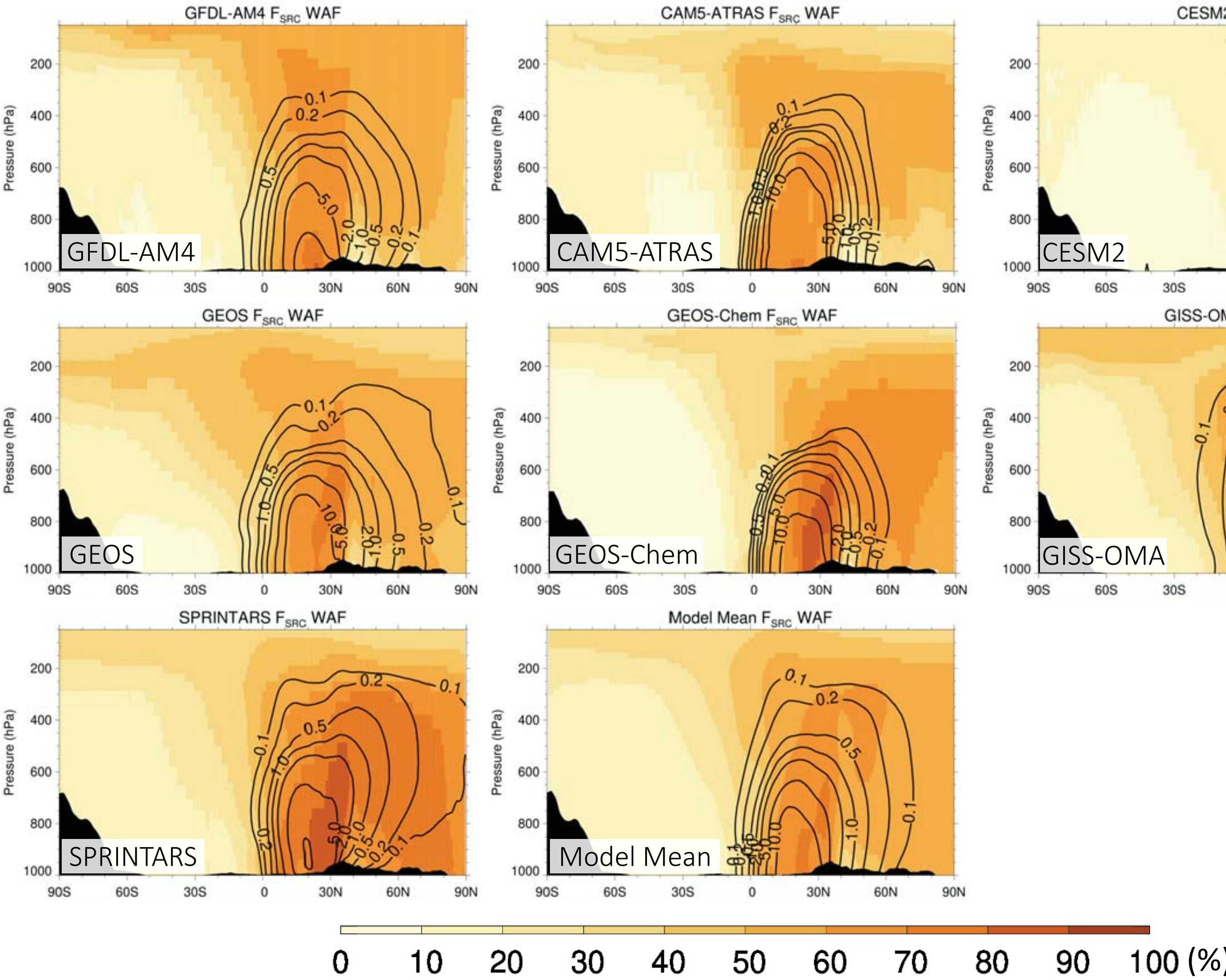

GFDL-AM4 F$_{SRC}$ WAF
CAM5-ATRAS F$_{SRC}$ WAF
CESM2 F$_{SRC}$ WAF
GEOS F$_{SRC}$ WAF
GEOS-Chem F$_{SRC}$ WAF
GISS-OMA F$_{SRC}$ WAF
SPRINTARS F$_{SRC}$ WAF
Model Mean F$_{SRC}$ WAF
GFDL-AM4
CAM5-ATRAS
CESM2
GEOS
GEOS-Chem
GISS-OMA
SPRINTARS
Model Mean
Pressure (hPa)
200
400
600
800
1000
90S
60S
30S
0
30N
60N
90N
0
10
20
30
40
50
60
70
80
90
100 (%)

Figure 7.

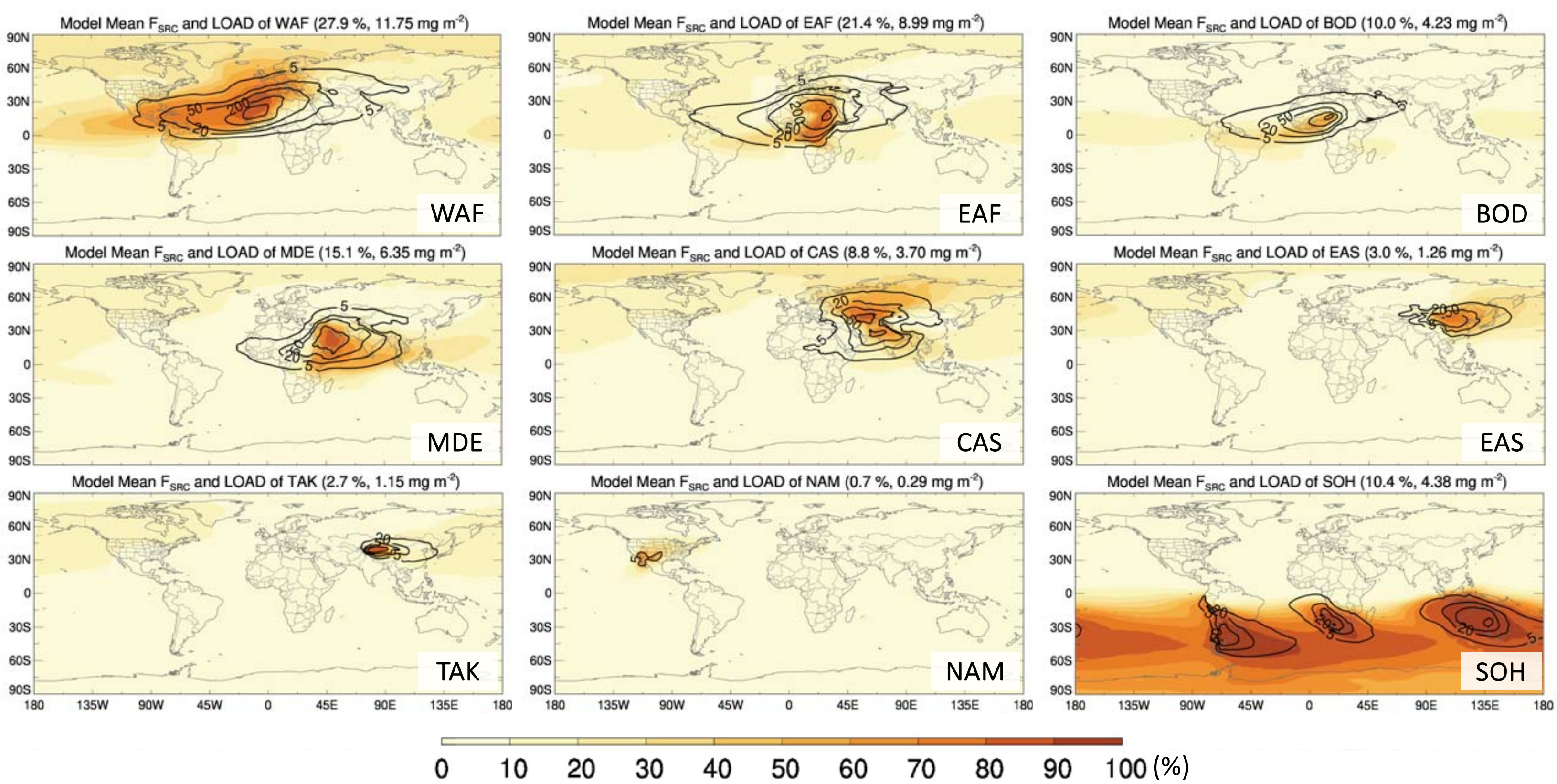
Model Mean F_{SRC} and LOAD of WAF (27.9 %, 11.75 mg m^{-2})
WAF
Model Mean F_{SRC} and LOAD of EAF (21.4 %, 8.99 mg m^{-2})
EAF
Model Mean F_{SRC} and LOAD of BOD (10.0 %, 4.23 mg m^{-2})
BOD
Model Mean F_{SRC} and LOAD of MDE (15.1 %, 6.35 mg m^{-2})
MDE
Model Mean F_{SRC} and LOAD of CAS (8.8 %, 3.70 mg m^{-2})
CAS
Model Mean F_{SRC} and LOAD of EAS (3.0 %, 1.26 mg m^{-2})
EAS
Model Mean F_{SRC} and LOAD of TAK (2.7 %, 1.15 mg m^{-2})
TAK
Model Mean F_{SRC} and LOAD of NAM (0.7 %, 0.29 mg m^{-2})
NAM
Model Mean F_{SRC} and LOAD of SOH (10.4 %, 4.38 mg m^{-2})
SOH
90N 60N 30N 0 30S 60S 90S
180 135W 90W 45W 0 45E 90E 135E 180
0 10 20 30 40 50 60 70 80 90 100 (%)

Figure 8.

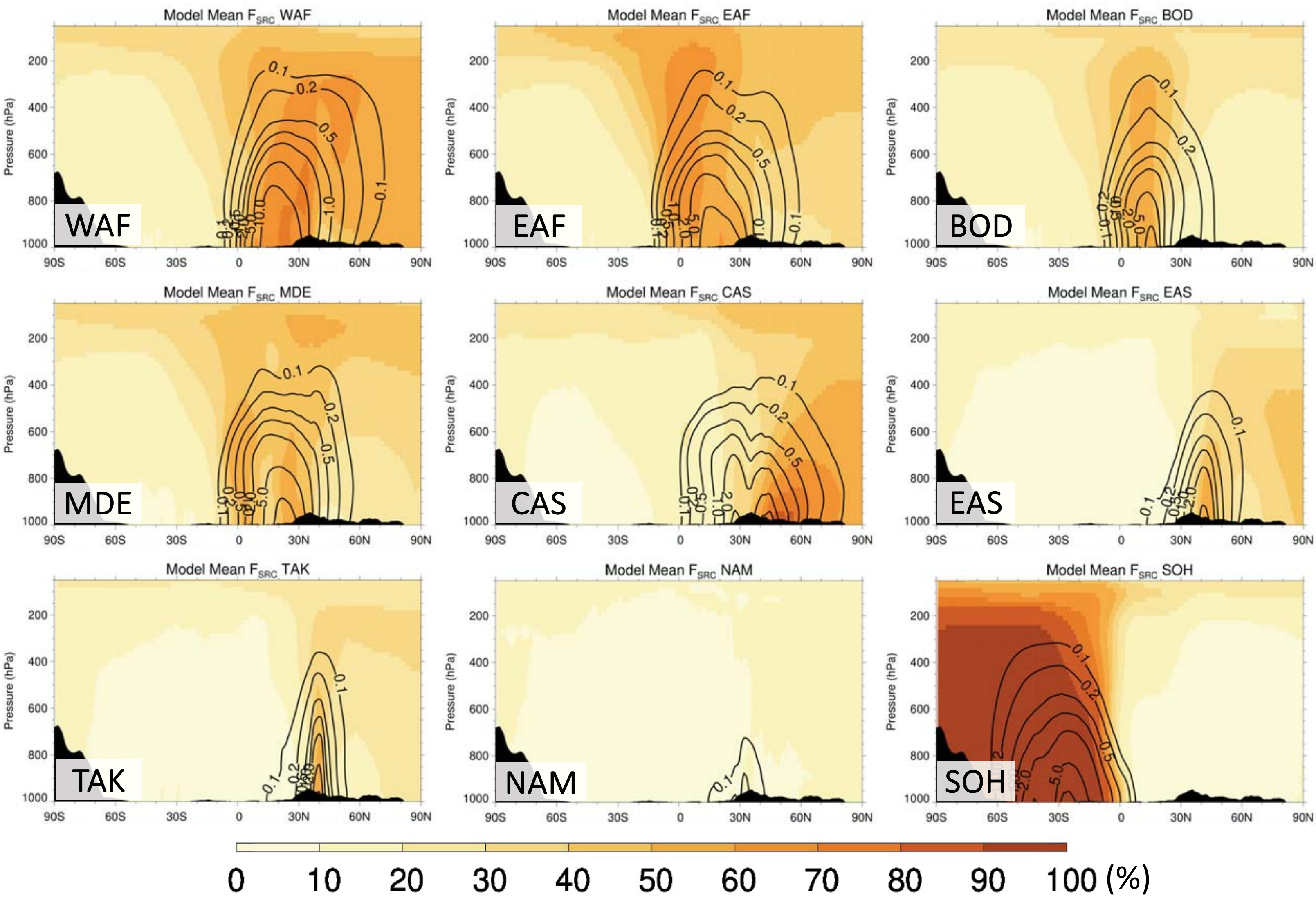

Model Mean F_{SRC} WAF
Model Mean F_{SRC} EAF
Model Mean F_{SRC} BOD
Model Mean F_{SRC} MDE
Model Mean F_{SRC} CAS
Model Mean F_{SRC} EAS
Model Mean F_{SRC} TAK
Model Mean F_{SRC} NAM
Model Mean F_{SRC} SOH
WAF
EAF
BOD
MDE
CAS
EAS
TAK
NAM
SOH
Pressure (hPa)
90S 60S 30S 0 30N 60N 90N
0 10 20 30 40 50 60 70 80 90 100 (%)

Figure 9.

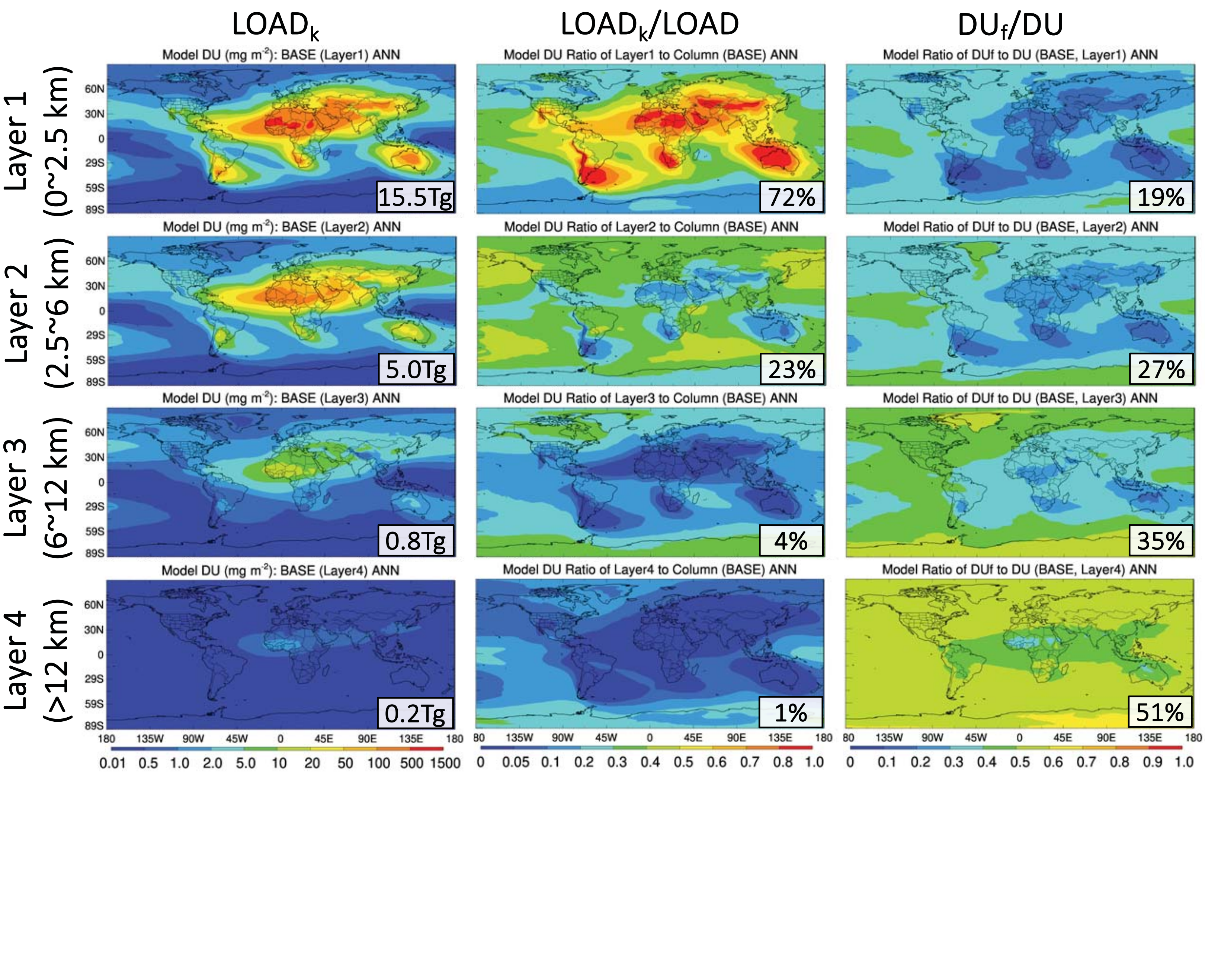

LOADk
LOADk/LOAD
DUf/DU
Layer 1 (0~2.5 km)
Layer 2 (2.5~6 km)
Layer 3 (6~12 km)
Layer 4 (>12 km)
Model DU (mg m-2): BASE (Layer1) ANN
Model DU Ratio of Layer1 to Column (BASE) ANN
Model Ratio of DUf to DU (BASE, Layer1) ANN
15.5Tg
72%
19%
Model DU (mg m-2): BASE (Layer2) ANN
Model DU Ratio of Layer2 to Column (BASE) ANN
Model Ratio of DUf to DU (BASE, Layer2) ANN
5.0Tg
23%
27%
Model DU (mg m-2): BASE (Layer3) ANN
Model DU Ratio of Layer3 to Column (BASE) ANN
Model Ratio of DUf to DU (BASE, Layer3) ANN
0.8Tg
4%
35%
Model DU (mg m-2): BASE (Layer4) ANN
Model DU Ratio of Layer4 to Column (BASE) ANN
Model Ratio of DUf to DU (BASE, Layer4) ANN
0.2Tg
1%
51%
60N 30N 0 29S 59S 89S
180 135W 90W 45W 0 45E 90E 135E 180
0.01 0.5 1.0 2.0 5.0 10 20 50 100 500 1500
0 0.05 0.1 0.2 0.3 0.4 0.5 0.6 0.7 0.8 1.0
0 0.1 0.2 0.3 0.4 0.5 0.6 0.7 0.8 0.9 1.0

Figure 10.

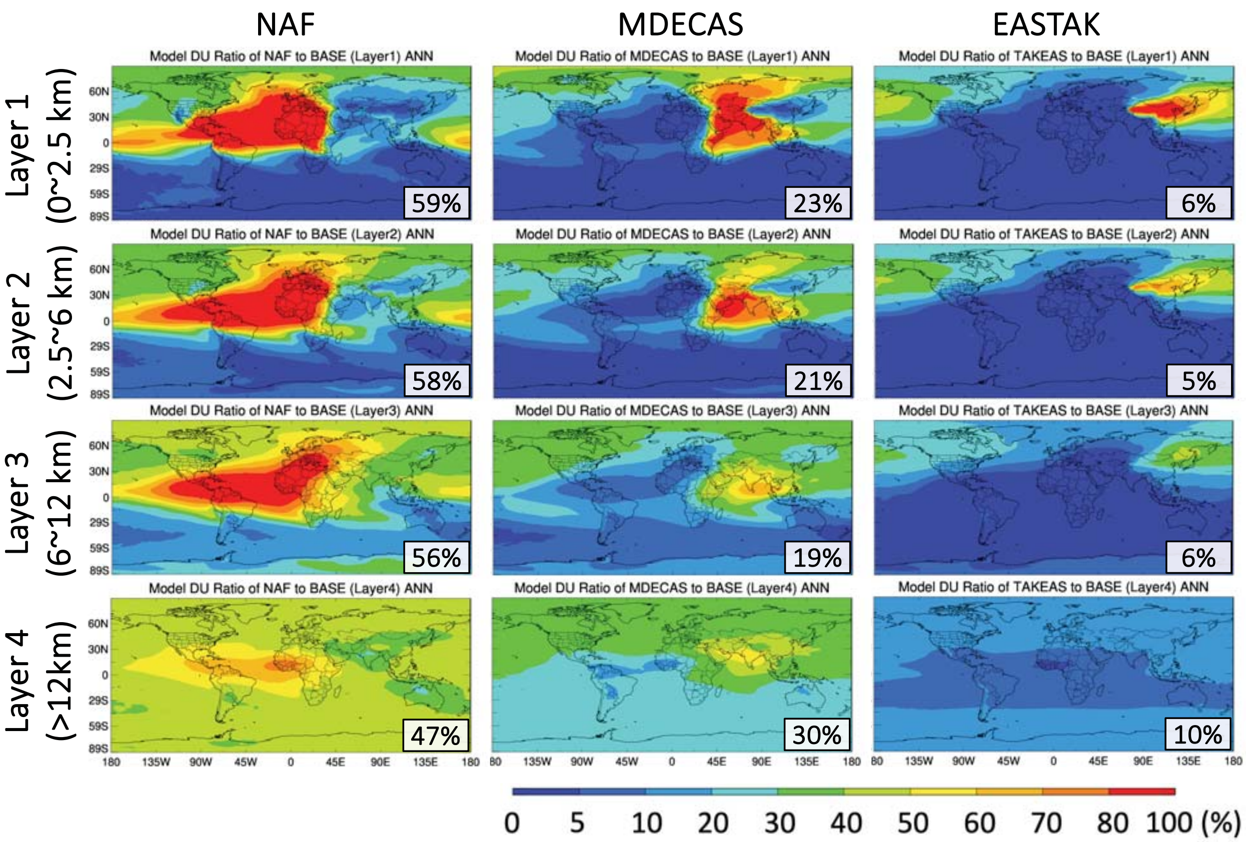
NAF
MDECAS
EASTAK
SOH
Layer 1 (0~2.5 km)
Layer 2 (2.5~6 km)
Layer 3 (6~12 km)
Layer 4 (>12km)
Model DU Ratio of NAF to BASE (Layer1) ANN
Model DU Ratio of MDECAS to BASE (Layer1) ANN
Model DU Ratio of TAKEAS to BASE (Layer1) ANN
Model DU Ratio of SOH to BASE (Layer1) ANN
59%
23%
6%
12%
Model DU Ratio of NAF to BASE (Layer2) ANN
Model DU Ratio of MDECAS to BASE (Layer2) ANN
Model DU Ratio of TAKEAS to BASE (Layer2) ANN
Model DU Ratio of SOH to BASE (Layer2) ANN
58%
21%
5%
15%
Model DU Ratio of NAF to BASE (Layer3) ANN
Model DU Ratio of MDECAS to BASE (Layer3) ANN
Model DU Ratio of TAKEAS to BASE (Layer3) ANN
Model DU Ratio of SOH to BASE (Layer3) ANN
56%
19%
6%
17%
Model DU Ratio of NAF to BASE (Layer4) ANN
Model DU Ratio of MDECAS to BASE (Layer4) ANN
Model DU Ratio of TAKEAS to BASE (Layer4) ANN
Model DU Ratio of SOH to BASE (Layer4) ANN
47%
30%
10%
11%
60N 30N 0 29S 59S 89S
180 135W 90W 45W 0 45E 90E 135E 180
0 5 10 20 30 40 50 60 70 80 100 (%)

Figure 11.

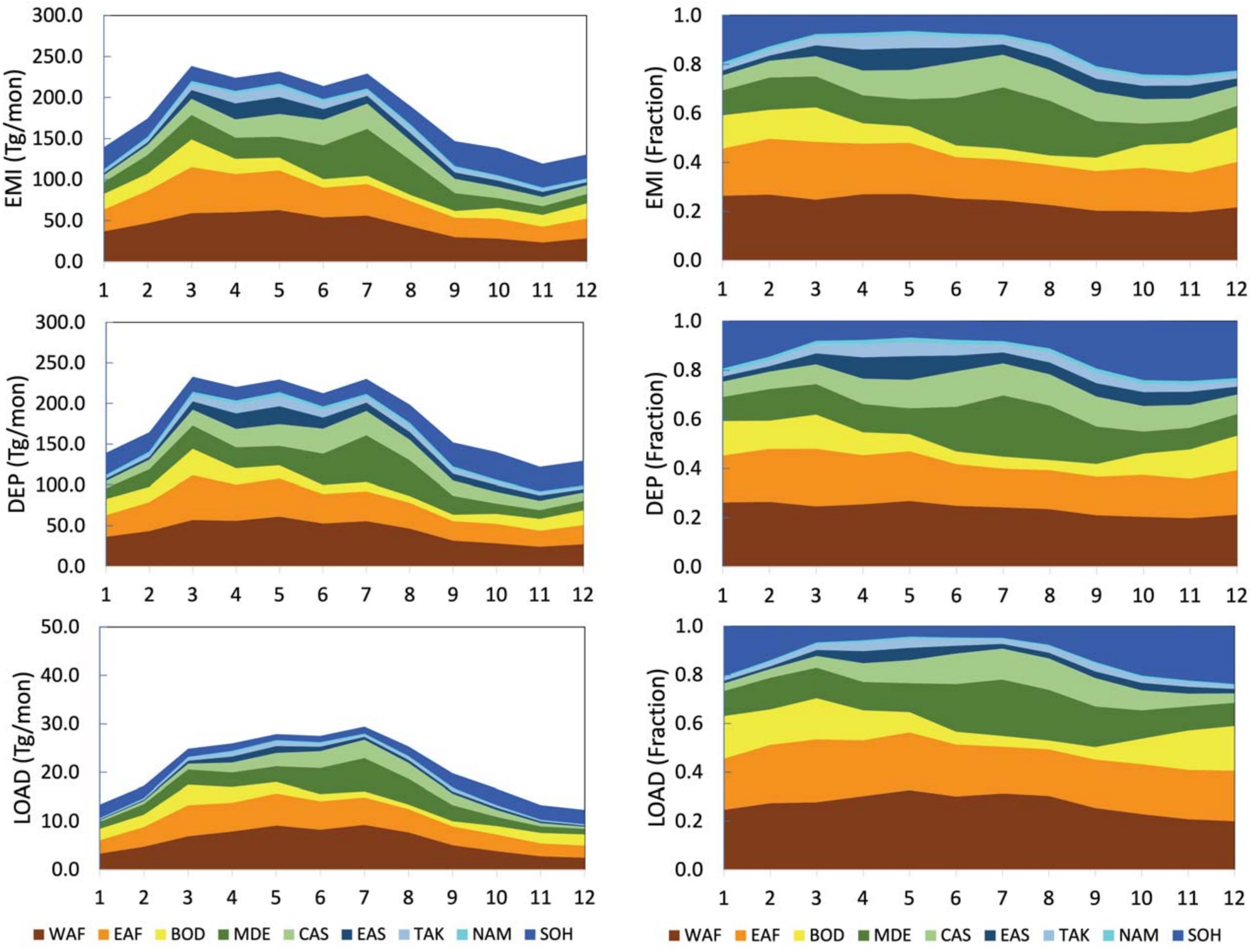

EMI (Tg/mon)
EMI (Fraction)
DEP (Tg/mon)
DEP (Fraction)
LOAD (Tg/mon)
LOAD (Fraction)
WAF EAF BOD MDE CAS EAS TAK NAM SOH
WAF EAF BOD MDE CAS EAS TAK NAM SOH

Figure 12.

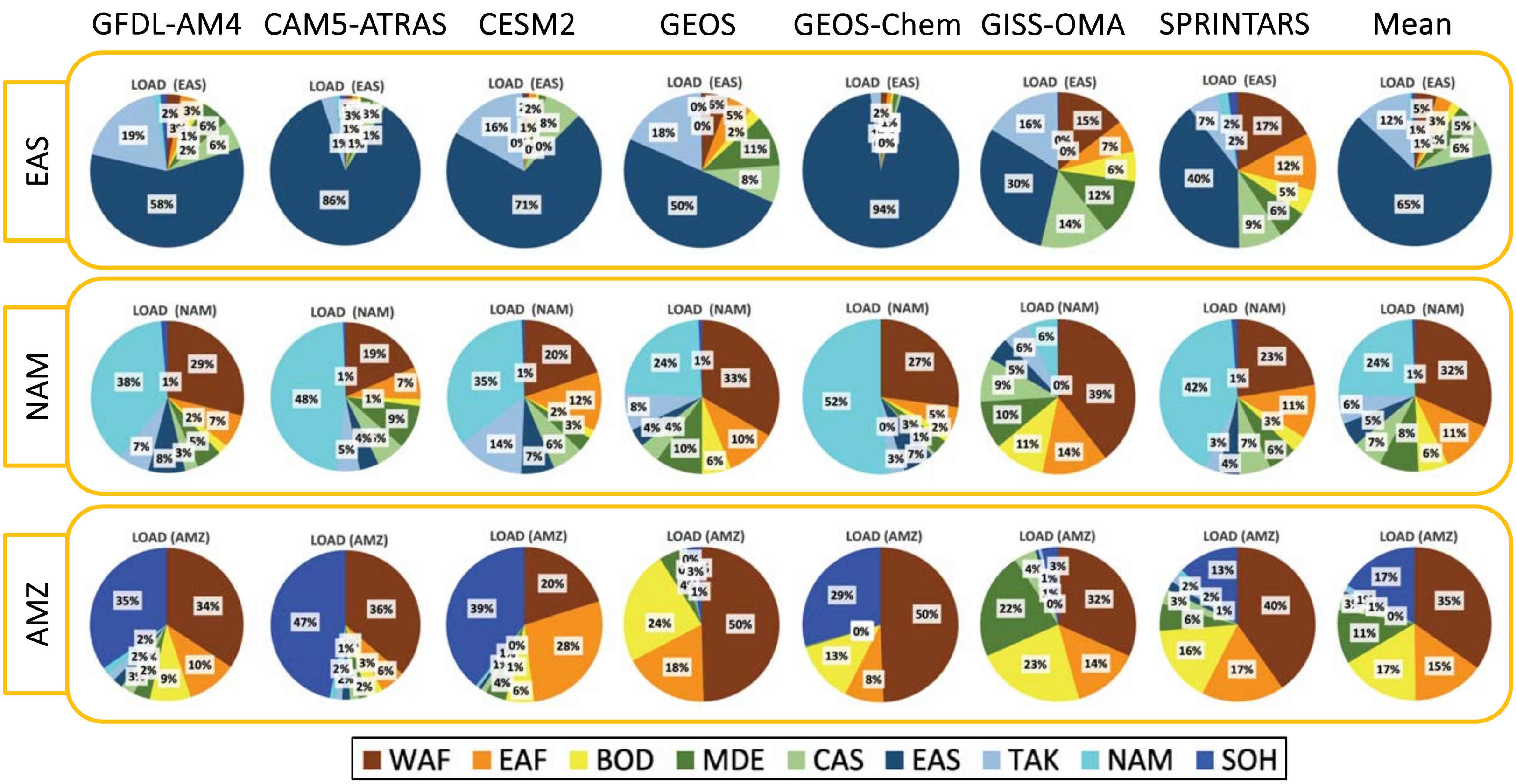
GFDL-AM4
CAM5-ATRAS
CESM2
GEOS
GEOS-Chem
GISS-OMA
SPRINTARS
Mean
EAS
NAM
AMZ
LOAD (EAS)
LOAD (NAM)
LOAD (AMZ)
WAF
EAF
BOD
MDE
CAS
EAS
TAK
NAM
SOH

Figure 13.

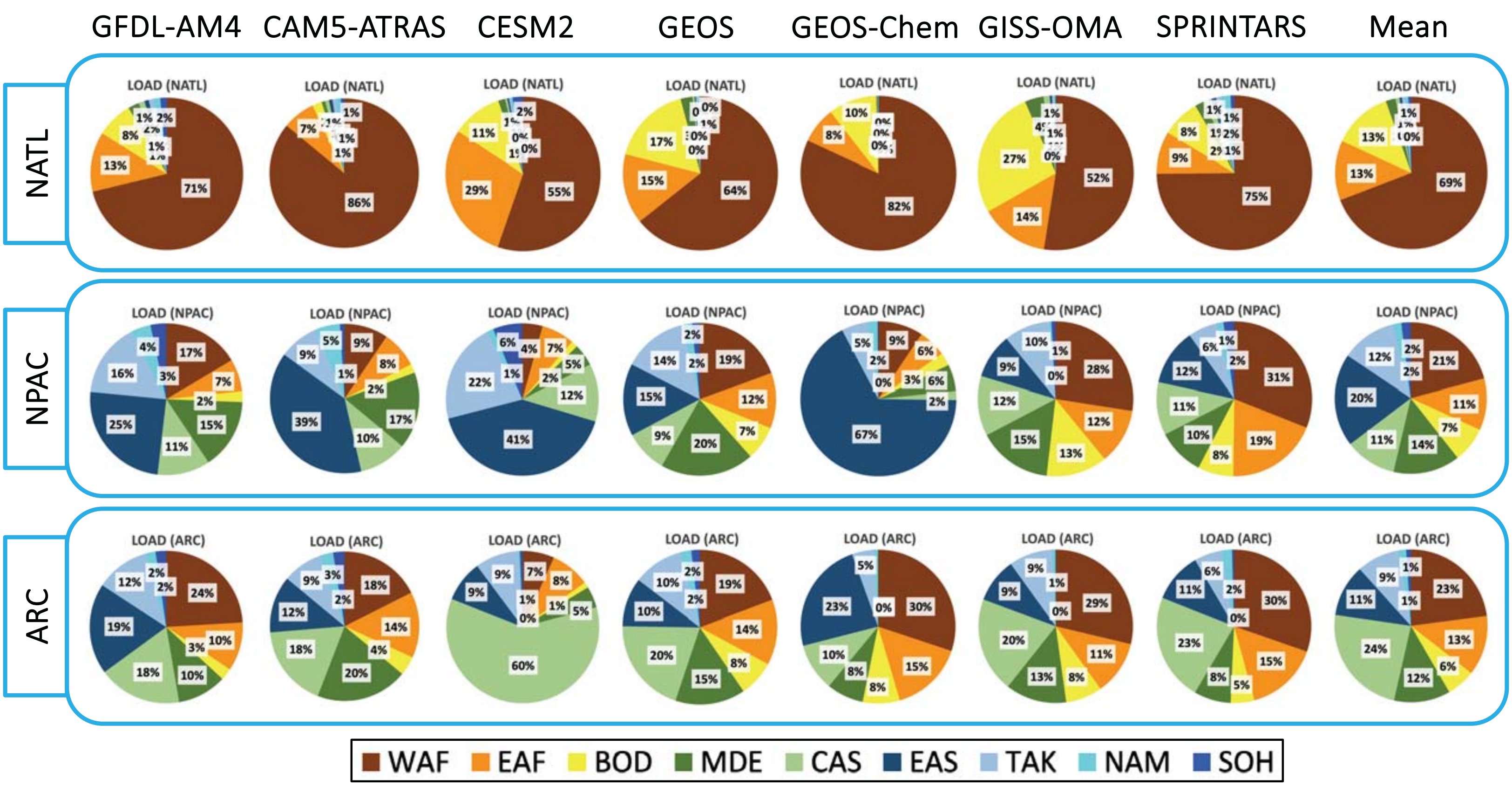
GFDL-AM4
CAM5-ATRAS
CESM2
GEOS
GEOS-Chem
GISS-OMA
SPRINTARS
Mean
NATL
NPAC
ARC
LOAD (NATL)
LOAD (NPAC)
LOAD (ARC)
WAF
EAF
BOD
MDE
CAS
EAS
TAK
NAM
SOH

Figure 14.

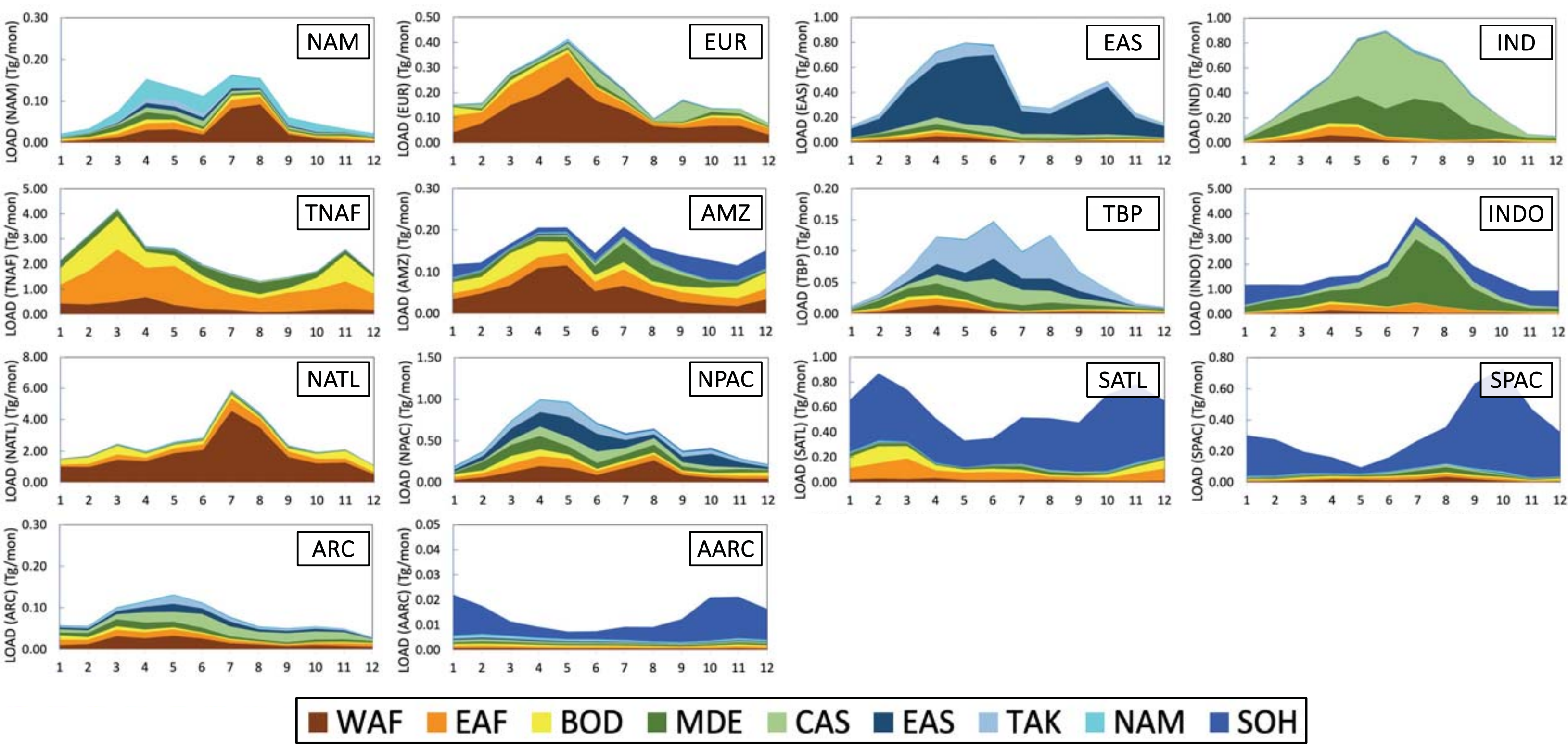
NAM
EUR
EAS
IND
TNAF
AMZ
TBP
INDO
NATL
NPAC
SATL
SPAC
ARC
AARC
LOAD (NAM) (Tg/mon)
LOAD (EUR) (Tg/mon)
LOAD (EAS) (Tg/mon)
LOAD (IND) (Tg/mon)
LOAD (TNAF) (Tg/mon)
LOAD (AMZ) (Tg/mon)
LOAD (TBP) (Tg/mon)
LOAD (INDO) (Tg/mon)
LOAD (NATL) (Tg/mon)
LOAD (NPAC) (Tg/mon)
LOAD (SATL) (Tg/mon)
LOAD (SPAC) (Tg/mon)
LOAD (ARC) (Tg/mon)
LOAD (AARC) (Tg/mon)
WAF EAF BOD MDE CAS EAS TAK NAM SOH

Figure 15.

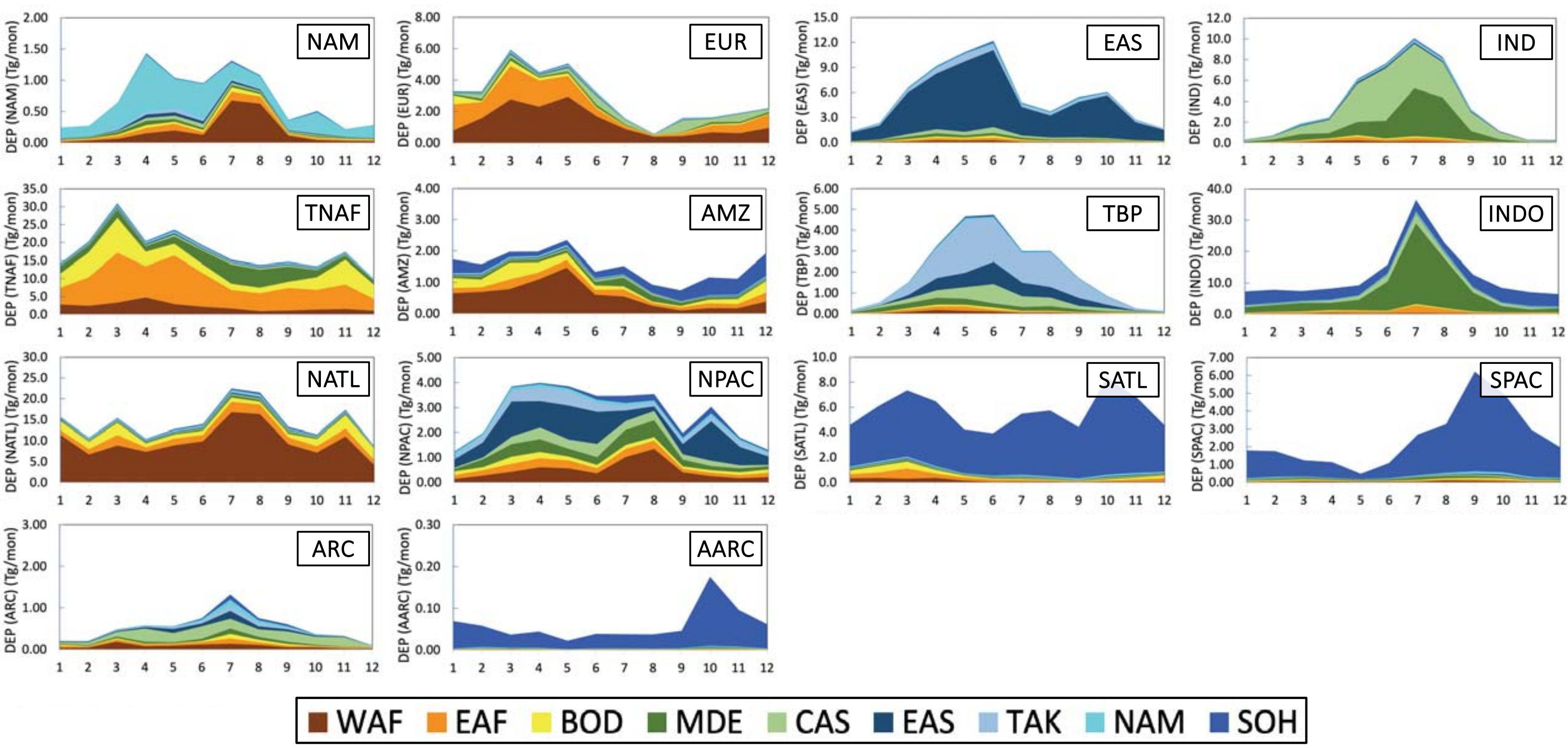

NAM
DEP (NAM) (Tg/mon)
EUR
DEP (EUR) (Tg/mon)
EAS
DEP (EAS) (Tg/mon)
IND
DEP (IND) (Tg/mon)
TNAF
DEP (TNAF) (Tg/mon)
AMZ
DEP (AMZ) (Tg/mon)
TBP
DEP (TBP) (Tg/mon)
INDO
DEP (INDO) (Tg/mon)
NATL
DEP (NATL) (Tg/mon)
NPAC
DEP (NPAC) (Tg/mon)
SATL
DEP (SATL) (Tg/mon)
SPAC
DEP (SPAC) (Tg/mon)
ARC
DEP (ARC) (Tg/mon)
AARC
DEP (AARC) (Tg/mon)
WAF
EAF
BOD
MDE
CAS
EAS
TAK
NAM
SOH

Figure 16.

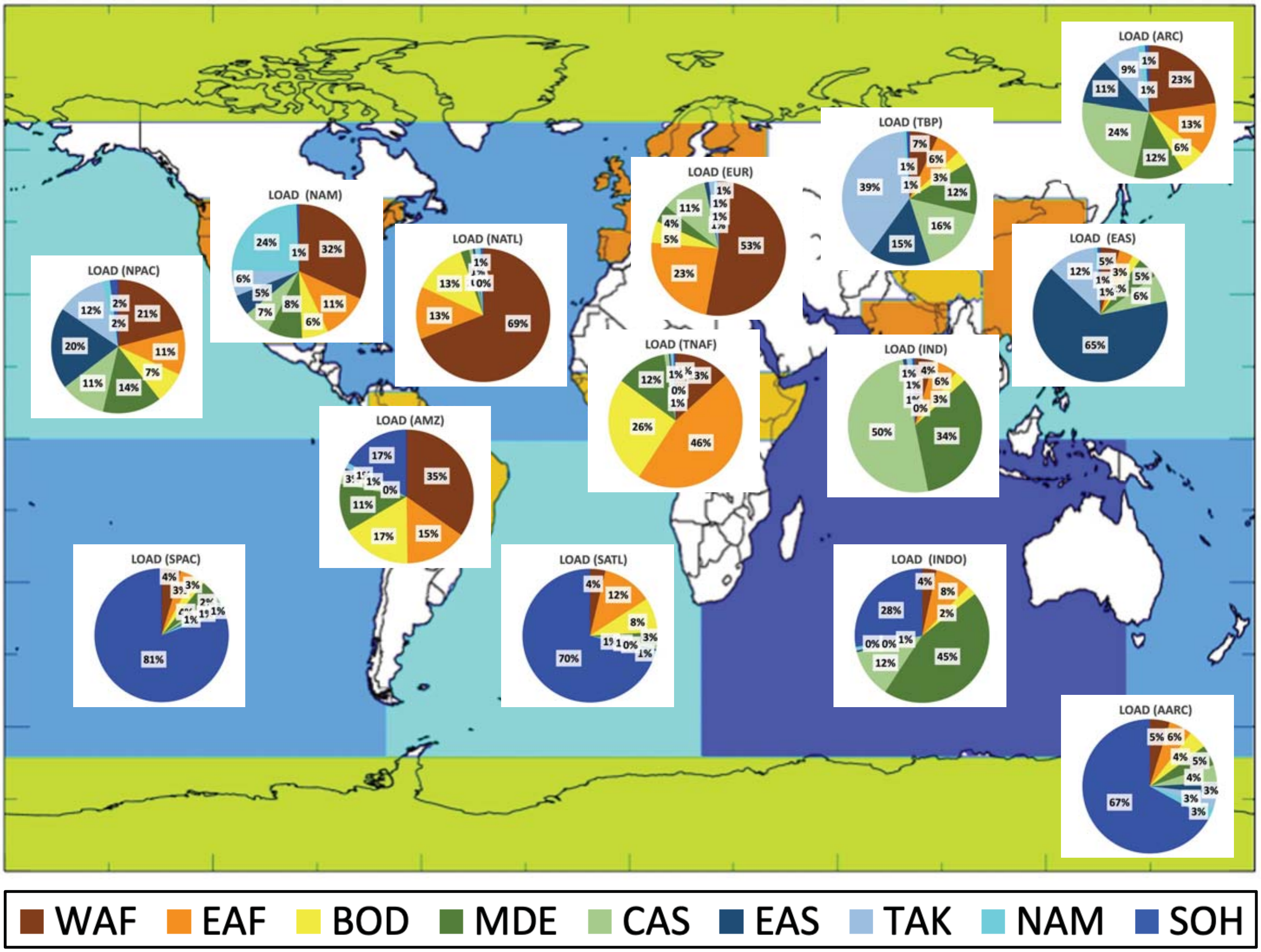
LOAD (ARC)
LOAD (TBP)
LOAD (EUR)
LOAD (NAM)
LOAD (NATL)
LOAD (NPAC)
LOAD (EAS)
LOAD (TNAF)
LOAD (IND)
LOAD (AMZ)
LOAD (SPAC)
LOAD (SATL)
LOAD (INDO)
LOAD (AARC)
WAF
EAF
BOD
MDE
CAS
EAS
TAK
NAM
SOH

Figure 17.

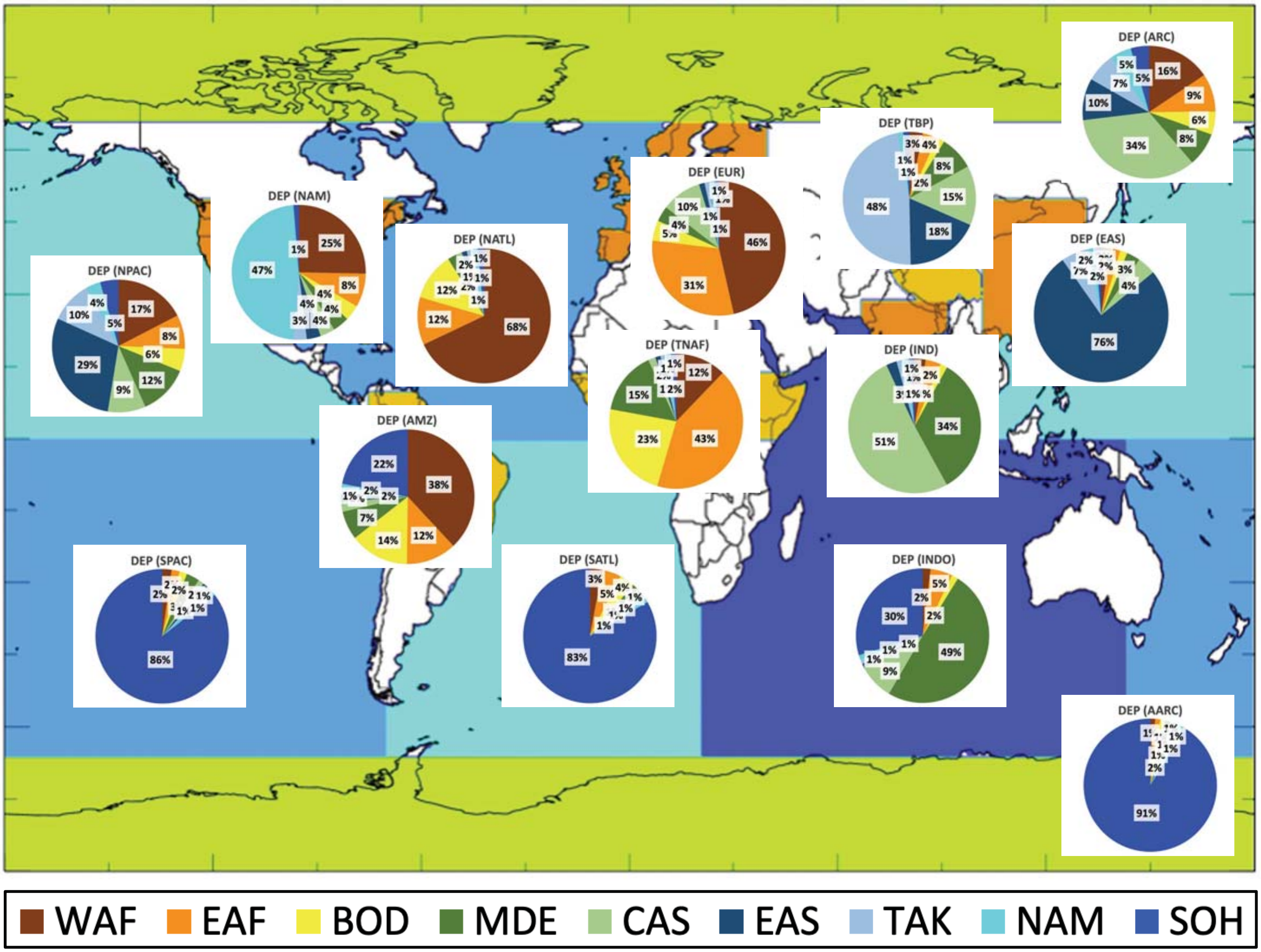
DEP (ARC)
16%
9%
6%
8%
34%
10%
7%
5%
5%
DEP (TBP)
3%
4%
8%
15%
18%
48%
DEP (EUR)
46%
31%
10%
4%
1%
DEP (NAM)
47%
25%
8%
4%
3%
1%
DEP (NATL)
68%
12%
12%
DEP (EAS)
76%
3%
4%
2%
DEP (NPAC)
17%
8%
6%
12%
9%
29%
10%
4%
5%
DEP (TNAF)
12%
43%
23%
15%
DEP (IND)
51%
34%
2%
DEP (AMZ)
38%
12%
14%
7%
22%
2%
DEP (SPAC)
86%
DEP (SATL)
83%
3%
5%
DEP (INDO)
49%
30%
9%
5%
2%
DEP (AARC)
91%
2%
WAF
EAF
BOD
MDE
CAS
EAS
TAK
NAM
SOH

Figure 18.

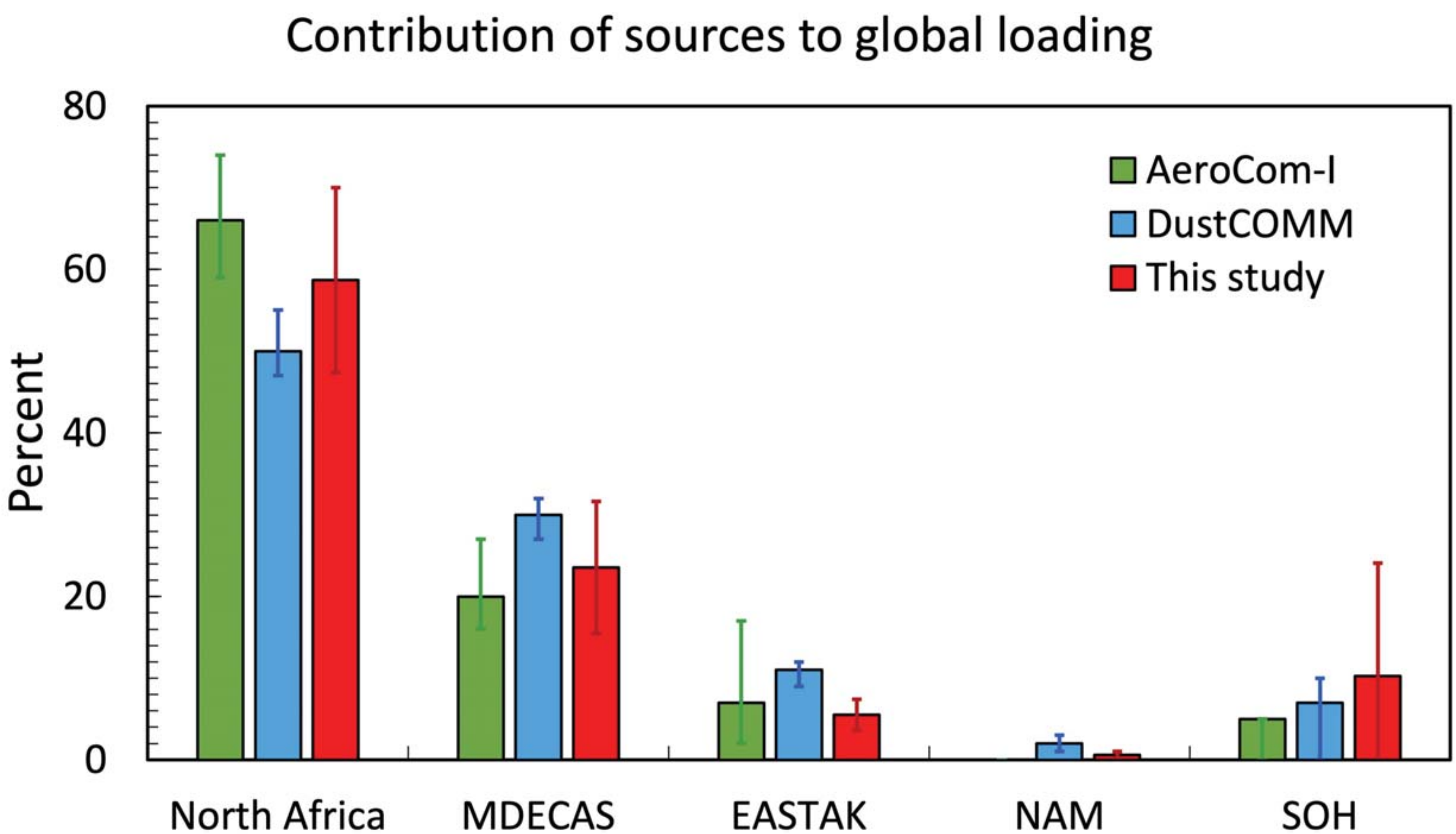

Contribution of sources to global loading
80
60
40
20
0
Percent
AeroCom-I
DustCOMM
This study
North Africa
MDECAS
EASTAK
NAM
SOH